

# **Incorporating Tl-based Materials into High Efficiency Multijunction Photovoltaics**

A thesis

submitted by

Chandler Downs

In partial fulfillment of the requirements  
for the degree of

Master of Science

in

Electrical Engineering

TUFTS UNIVERSITY

Date

May, 2011

ADVISOR: Thomas Vandervelde

**Abstract:**

The optimum band structure for both multijunction photovoltaics, where layers of semiconductor materials are connected in series, and split junction photovoltaic systems, consisting of a number of physically separated solar cells, are investigated. Possible implementations of these designs are suggested, based on design constraints such as lattice matching, use of possible substrates, and ease of material growth, and then simulated. In order to realize these implementations, it was required to include TI-bearing semiconductor materials in the simulations; this is a class of materials that has not been extensively studied, particularly for use in photovoltaics. Incorporation of this class of materials in photovoltaics is shown to both improve the effectiveness of some high performance cells already studied by other groups as well as allow for new high conversion efficiency band structures.

## Table of Contents

Abstract.....	i
Table of Contents.....	ii
List of Figures.....	vii
Chapter 1: Introduction.....	1
1.1 A Brief History of Photovoltaics.....	3
1.2 The Physics of Solar Cells.....	6
1.2.1 The Solar Spectrum.....	6
1.2.2 Relevant Physics of Light.....	8
1.2.3 The Photovoltaic and Photoelectric Effects.....	8
1.3 Semiconductor Physics and Band Theory.....	10
1.3.1 Lattice Constants.....	10
1.3.2 Valence and Conduction Bands.....	11
1.3.3 Band Interactions.....	13
1.3.4 The Kronig-Penny Model.....	14
1.3.5 Indirect Gap vs. Direct Gap.....	18
1.3.6 Effective Mass of Carriers.....	20
1.3.7 Diffusion and Drift Current Densities.....	21
1.3.7.1 Diffusion Current Density.....	21
1.3.7.2 Drift Current Density.....	22
1.3.8 The Fermi Level and the Fermi-Dirac Probability Function.....	23
1.3.9 Other Intrinsic Characteristics.....	25
1.3.10 Doping.....	25
1.3.11 p-n Heterojunctions.....	27

1.3.12	Carrier Lifetime and Diffusion Length.....	31
1.3.13	III-V and II-VI Materials.....	32
1.3.14	Ternary and Quaternary Materials.....	34
1.3.15	Lattice Matching and Mismatch Strain.....	37
1.3.16	Lattice Defects.....	39
1.4	The Current State of Photovoltaic Technologies.....	40
1.4.1	Single Crystal Silicon.....	40
1.4.2	Amorphous Silicon.....	43
1.4.3	Dye-Sensitized Solar Cells.....	45
1.4.4	Organic Solar Cells.....	48
1.4.5	Up-Conversion.....	51
1.4.6	Down-Conversion.....	54
1.4.7	Nanoparticles and Quantum Structures.....	58
1.4.8	Multijunction Photovoltaics and Concentrating Arrays.....	67
1.4.9	Split Junction Photovoltaics.....	74
1.4.10	Tunnel Diodes.....	76
1.4.11	Antireflective Coatings.....	80
1.5	Performance Parameters and Rubrics.....	82
1.5.1	Built-in Voltage, Open Circuit Voltage, and Bias Voltage.....	82
1.5.2	Dark Current, Photocurrent, Short Circuit Current, and Load Current.....	84
1.5.3	Performance Rubrics.....	86
1.6	Basic Economics of Solar Cells.....	87
1.7	Motivation for Research.....	89
Chapter 2: Materials and Methods.....		91

2.1 Synopsys Sentaurus TCAD.....	91
2.1.1 Sentaurus Workbench.....	91
2.1.2 Sentaurus Structure Editor.....	92
2.1.3 Sentaurus Device.....	93
2.1.3.1 Transfer Matrix Method.....	94
2.1.4 Inspect.....	97
2.1.5 Tecplot.....	98
2.2 Fabrication Equipment and Deposition Methods.....	99
2.2.1 Molecular Beam Epitaxy.....	99
2.2.2 Photolithography.....	100
2.2.3 Rapid Thermal Annealing.....	103
2.2.4 Ion Beam Deposition.....	103
2.3 IV-Station.....	105
2.3.1 Solar Simulator.....	106
2.3.2 Test Area and Probing Stations.....	106
2.3.3 Reference Cell.....	108
2.3.4 Thermoelectric Chiller.....	109
2.3.5 Sourcemeeter.....	110
2.4 Other Testing Apparatus.....	111
2.4.1 Spectroscopic Ellipsometer.....	111
<b>Chapter 3: Band Gap Optimization of Split Junction Solar Cells_____</b>	<b>113</b>
3.1 Full Spectrum Solar Cells.....	114
3.1.1 A Single Junction Full Spectrum Cell.....	114
3.1.2 Multijunction Full Spectrum.....	117
3.2 Multijunction Split Junction Solar Cells.....	118

3.2.1	867 nm Cutoff Split Junction Cell.....	120
3.2.2	925 nm Cutoff Split Junction Cell.....	121
3.2.3	1100 nm Cutoff Split Junction Cell.....	124
3.2.3.1	1100 nm Cutoff Split Junction Cell – Silicon Based...124	
3.2.3.2	1100 nm Cutoff Split Junction Cell – GaAs Based....125	
3.2.4	1698 nm Cutoff Split Junction Cell.....	126
3.3	Conclusions.....	128
Chapter 4: Simulation of Thallium-Based Multijunction Cells_____		130
4.1	Simulation of Single Junction Photovoltaic Cells.....	131
4.1.1	Simulation of a Single Junction GaInP Cell.....	131
4.1.2	Simulation of a Single Junction InGaAs Cell.....	133
4.1.3	Simulation of a Single Junction Ge cell.....	135
4.2	Simulation of a Tunnel Diode.....	136
4.3	Simulation of Dual Junction Cells.....	137
4.3.1	Simulation of a GaInP/InGaAs Cell.....	138
4.3.2	Simulation of a InGaAs/Ge Cell.....	140
4.4	Simulation of Triple Junction Cells.....	142
4.4.1	Simulation of a GaInP/InGaAs/Ge Cell.....	142
4.4.2	Simulation of a GaInP/InGaAs/GaTIP Cell.....	144
4.4.3	Simulation of a GaInP/AlGaAs/GaTIP Top Cell.....	147
4.4.4	Simulation of a GaSb TPV Cell.....	148
4.4.5	Simulations of Triple Junction Cells Utilizing Antireflective Coatings.....	151
4.5	Conclusions and Future Work.....	153
Chapter 5: Conclusions and Future Work_____		156

Appendix: Figure Credits	161
Bibliography	164

## List of Figures

<b>Figure 1.1:</b> Conversion efficiency of photovoltaic cell type by year. As time has advanced, the efficiency of each technology has gradually improved [1]. Each improvement in efficiency brings the technology another step closer to economic viability.....	5
<b>Figure 1.2:</b> Spectral intensity vs. wavelength of light present under different atmospheric conditions. AM0 corresponds to outside of Earth’s atmosphere and AM1.5 corresponds to typical atmospheric conditions at Earth’s surface [2].....	6
<b>Figure 1.3:</b> An illustration of the dependence of the AM spectra on angle of incidence of light and the distance the light travels through the atmosphere. AM0 and AM1 are included as a reference [3].....	7
<b>Figure 1.4:</b> A comparison of wavelength/frequency of light and the energy of the photons that compose that light (in both J and eV). The wavelengths of the visible light spectrum are denoted by the small spectra in the upper left of the diagram [4].....	8
<b>Figure 1.5:</b> Sample models of a) simple cubic, b) body centered cubic, and c) face centered cubic lattice structures [3].....	9
<b>Figure 1.6:</b> Electrons filling the available states in a semiconductor at an arbitrary temperature $T > 0^{\circ}$ K. Each circle represents an available energy state and each filled circle represents an electron [4].....	11
<b>Figure 1.7:</b> A model of the periodic potential well utilized in the Kronig-Penney model [5].....	14

**Figure 1.8:** An example plot of a simplification of the left hand side of the solution to the Kronig-Penney model. Only the values for this equation valued between +1 and -1 are valid as per the right hand side of the solution. P is an aggregation of the variables listed above.....16

**Figure 1.9:** Cross section of the E-k band structure for Si (an indirect gap material) and GaAs (a direct gap material) in the [111] direction (left side of each plot) and the [100] direction (right side of each plot) [4].....17

**Figure 1.10:** The Fermi-Dirac probability function evaluated for a number of different temperatures for a particular semiconductor device [5].....23

**Figure 1.11:** Silicon lattices doped with a) an acceptor material (Boron) and b) a donor material (Phosphorus).....25

**Figure 1.12:** Energy states in the forbidden band of a semiconductor created by doping with a) n-type (donor) material and b) p-type (acceptor) material.[6]....26

**Figure 1.13:** a) a physical diagram of a p-n junction, b) the distribution of charge, c) the electric field across the junction, d) the voltage across the junction, and e) the final band structure of the entire junction [7].....28

**Figure 1.14:** A diagram of a p-n junction [7].....29

**Figure 1.15:** The Periodic Table of Elements with groups III and V (yellow) and II-VI (blue) materials highlighted.....31

**Figure 1.16:** A plot of the band gap of  $\text{In}_{1-x}\text{Ga}_x\text{As}_y\text{P}_{1-y}$  over changing values for x and y [8].....34

**Figure 1.17:** When lattice mismatching is small, the only effect is strain on the materials, instead of defects. Both a) biaxial compressive strain (when the lattice constant of the epitaxial layer is greater than that of the substrate layer) and b) biaxial tensile strain (when the lattice constant is less than that of the substrate layer) are possible.....37

**Figure 1.18:** A sample diagram of a dislocation between two lattice mismatched materials.....38

**Figure 1.19:** An electron carrier in the conduction band undergoing Shockley-Read-Hall (SRH) recombination due to the existence of a trap state of energy level,  $E_T$ , existing in the material.....39

**Figure 1.20:** A comparison of theoretical maximum efficiency (or Shockley-Queisser limit) given a single material of a given band gap. Several well known semiconductor materials are specifically marked on the graph, including both crystalline and amorphous (a-) materials [9].....41

**Figure 1.21:** A comparison of photoconductive at varying intensities of light before (A) and after (B) exposure to approximately four hours of  $200 \text{ mW/cm}^2$  of light [10].....43

**Figure 1.22:** A diagram of the general layout of a dye-sensitized solar cell (DSC) [11].....45

**Figure 1.23:** A band structure for a bilayer heterojunction organic solar cell. It is separated into donor (D) and acceptor (A) regions[12].....48

**Figure 1.24:** A comparison of efficiency ( $\eta$ ) for a) energy transfer up-conversion (ETU) b) 2-step ground state absorption (GSE) and excited state absorption

(ESA) c) cooperative sensitisation d) cooperative luminescence e) second harmonic generation (SHG) and f) multi-photon excitation [13].....52

**Figure 1.25:** A band diagram of an ideal down-converter system. The down-converter has a bandgap twice that of the solar cell with an impurity layer (IL) of available states in the middle [14].....55

**Figure 1.26:** A comparison of the efficiencies of a photovoltaic system for the Shockley-Queisser limit of a single junction cell (solid line), with a down-converter on the front surface (open squares), and with a down-converter on the rear surface using a reflective coating (solid circles) [14].....56

**Figure 1.27:** Transmission electron microscopy (TEM) images of a ‘tetrapod’ three dimensional nanostructure [15].....59

**Figure 1.28:** A SEM image of a superlattice of GaAs and AlGaAs [16].....60

**Figure 1.29:** A sample band structure for a photovoltaic device utilizing quantum wells [17].....60

**Figure 1.30:** A sample band diagram illustrating the formation of minibands in a superlattice of quantum wells [4].....62

**Figure 1.31:** A TEM image of nanorods [15].....63

**Figure 1.32:** A TEM image of an InAs/GaAs quantum dot [18].....65

**Figure 1.33:** A  $1\mu\text{m} \times 1\mu\text{m}$  atomic force microscope (AFM) image of InAs quantum dots on a GaAs substrate [19].....66

**Figure 1.34:** Example a solar cell under nonuniform concentration ( $\sim 1000$  suns). A voltage difference of upwards of .15 V has arisen parallel to the plane of the solar cell [20].....69

**Figure 1.35:** The optimum band gap under conditions of high irradiance-high temperature (HIHT), medium irradiance-high temperature (MIHT), high irradiance-low temperature (HILT), low irradiance-low temperature (LILT), and medium irradiance-medium temperature (MIMT) for each layer of a a) 1-junction cell b) 2-junction cell c) 3-junction cell d) 4-junction cell and e) 5-junction cell [21].....70

**Figure 1.36:** Plots of PV system cost per kWh electricity generated in a 5-year period, as a function of cell cost per unit area, for both flat-plate (non-concentrated) and concentrator PV systems. Current multijunction photovoltaics have achieved conversion efficiencies of over 40% under concentration [22]....72

**Figure 1.37:** Sample reflectivity (red) and transmission (black) spectra for a dichroic filter [23].....73

**Figure 1.38:** Band structures like the one in a) would be ideal for multijunction cells. Moving from left-to-right, both the conduction and valence band edges are always lowering in energy. Much more common are band structures as seen in b), where moving from the n-doped region of the left junction and the p-doped region of the right junction introduces a potential barrier in both bands.....75

**Figure 1.39:** An example of an I-V curve for a tunnel diode.....76

**Figure 1.40:** Band structure of energy states in a tunnel diode where tunnel can occur. Grey areas are filled with electrons, white areas with holes [24].....77

**Figure 1.41:** The band structure of a tunnel diode (center) between GaInP (left) and GaInAs p-n junctions.....78

**Figure 1.42:** A close-up of the band structure of the tunnel diode in Figure 1.41. The n-side (left) follows the proper design criteria, leading to a continuous band edge. The p-side does not, and thus has a band discontinuity.....79

**Figure 1.43:** A comparison of a light current I-V curve and a dark current I-V curve. On the light I-V curve the maximum power point is identified. The power rectangle associated with that point is also illustrated in gray [25].....84

**Figure 2.1:** A sample output from Sentaurus Structure Editor, showing the physical structure of a single junction photovoltaic cell.....91

**Figure 2.2:** In each image, a region (box outline) is defined near the interface of two different homogeneous materials (yellow and green boxes). The region in a) is allowed, as the region is composed of a single, homogeneous material. The region in b) is prohibited, as the region contains the interface of two materials...93

**Figure 2.3:** A sample of the plots produced by Inspect, utilizing data imported from a Sentaurus Device simulation of a solar cell.....96

**Figure 2.4:** A sample of plots generated by Tecplot. On the left is a spatial plot of a single junction solar cell. On the right is the band structure of the cell, taken along a 1-D strip on the far left of the cell.....97

**Figure 2.5:** An image of the OAI 204IR Mask Aligner.....100

**Figure 2.6:** An image of the solar simulator.....105

**Figure 2.7:** An image of the test area and probe stations.....106

**Figure 2.8:** An image of the reference cell.....108

**Figure 2.9:** An image of the thermoelectric chiller.....109

**Figure 2.10:** An image of the sourcemeter.....110

**Figure 2.11:** A diagram of a spectroscopic ellipsometer. In this case, the light source is a white light source and a monochromator, the input stage is a polarizer for producing linearly polarized light and quarter wave plate, the sample stage is just the sample, and the output stage is the analyzer and the photodetector [26].....111

**Figure 3.1:** Ideal band gap placement for a full spectrum single junction solar cell as calculated by the band gap optimization program (left) and Zdanowicz et al. (center) [21].....115

**Figure 3.2:** Ideal band gap placement for a full spectrum dual junction solar cell as calculated by the band gap optimization program (left) and Zdanowicz et al.(right) [21].....117

**Figure 3.3:** Ideal band gap placement for a full spectrum triple junction solar cell as calculated by the band gap optimization program (left) and Zdanowicz et al.(right)[21].....117

**Figure 3.4:** Ideal band gap placement for single, dual, and triple junction PV cells in a split junction system. Material suggestions for each junction are provided if applicable.....119

**Figure 3.5:** Ideal band gap placement for single and dual junction TPV cells in a split junction system. Material suggestions for each junction are provided if applicable.....119

**Figure 3.6:** Ideal band gap placement for single, dual, and triple junction PV cells in a split junction system. Material suggestions for each junction are provided if applicable.....121

**Figure 3.7:** Ideal band gap placement for single and dual junction TPV cells in a split junction system. Material suggestions for each junction are provided if applicable.....121

**Figure 3.8:** Lattice constant vs. band gap plot for common group IV, III-V, and II-VI semiconductors. Certain regions of this plot have very few well characterized materials and are denoted as gaps. Gap 1 is germane to the 925 nm cutoff system, while Gap 2 is relevant to the 1100 nm cutoff system. Adapted from [27].....122

**Figure 3.9:** Ideal band gap placement for single, dual, and triple junction PV cells in a split junction system. Material suggestions for each junction are provided if applicable.....123

**Figure 3.10:** Ideal band gap placement for single and dual junction TPV cells in a split junction system. Material suggestions for each junction are provided if applicable.....123

**Figure 3.11:** Ideal band gap placement for single, dual, and triple junction PV cells in a split junction system. Material suggestions for each junction are provided if applicable.....125

**Figure 3.12:** Ideal band gap placement for single, dual, and triple junction PV cells in a split junction system.....126

**Figure 3.13:** Ideal band gap placement for single and dual junction TPV cells in a split junction system.....126

**Figure 4.1:** Physical structure and equilibrium band diagram of a GaInP (red) single junction cell.....131

**Figure 4.2:** Structural parameters of GaInP cell.....131

**Figure 4.3:** J-V and P-V curves for the GaInP cell.....132

**Figure 4.4:** Performance metrics for GaInP cell. Short circuit current density ( $J_{SC}$ ), open circuit voltage ( $V_{OC}$ ), maximum power ( $P_m$ ), fill factor (FF), and conversion efficiency (Efficiency) are listed.....132

**Figure 4.5:** Physical structure and equilibrium band diagram of an InGaAs (red) single junction cell.....133

**Figure 4.6:** Structural parameters of InGaAs cell.....133

**Figure 4.7:** J-V and P-V curves for the InGaAs cell with truncated (left) and full (right) incident spectrum.....133

**Figure 4.8:** Performance metrics for the InGaAs cell. Short circuit current density ( $J_{SC}$ ), open circuit voltage ( $V_{OC}$ ), maximum power ( $P_m$ ), fill factor (FF), and conversion efficiency (Efficiency) are listed.....134

**Figure 4.9:** Physical structure and equilibrium band diagram of a Ge (red) single junction cell.....134

**Figure 4.10:** Structural parameters of Ge cell.....135

**Figure 4.11:** J-V and P-V curves for the Ge cell with a truncated (left) and full (right) incident spectrum.....135

**Figure 4.12:** Performance metrics for the Ge cell. Short circuit current density ( $J_{SC}$ ), open circuit voltage ( $V_{OC}$ ), maximum power ( $P_m$ ), fill factor (FF), and conversion efficiency (Efficiency) are listed.....135

**Figure 4.13:** J-V curve for an  $Al_7Ga_3As/GaAs$  tunnel diode.....136

<b>Figure 4.14:</b> Physical structure and band diagram of a GaInP(red)/InGaAs(blue) dual junction cell.....	137
<b>Figure 4.15:</b> Structural parameters of GaInP/InGaAs cell.....	138
<b>Figure 4.16:</b> J-V and P-V curves for the GaInP/InGaAs cell.....	138
<b>Figure 4.17:</b> Performance metrics for the GaInP/InGaAs cell. Short circuit current density ( $J_{SC}$ ), open circuit voltage ( $V_{OC}$ ), maximum power ( $P_m$ ), fill factor (FF), and conversion efficiency (Efficiency) are listed.....	138
<b>Figure 4.18:</b> Physical structure and band diagram of an InGaAs(cyan)/Ge(blue) dual junction cell.....	139
<b>Figure 4.19:</b> Structural parameters of InGaAs/Ge cell.....	140
<b>Figure 4.20:</b> J-V and P-V curves for the InGaAs/Ge cell with a truncated (left) and full (right) incident spectrum.....	140
<b>Figure 4.21:</b> Performance metrics for the InGaAs/Ge cell. Short circuit current density ( $J_{SC}$ ), open circuit voltage ( $V_{OC}$ ), maximum power ( $P_m$ ), fill factor (FF), and conversion efficiency (Efficiency) are listed.....	140
<b>Figure 4.22:</b> Physical structure and equilibrium band diagram of a GaInP/InGaAs/Ge triple junction cell.....	142
<b>Figure 4.23:</b> Structural parameters of GaInP/InGaAs/Ge cell.....	142
<b>Figure 4.24:</b> J-V and P-V curves for the GaInP/InGaAs/Ge cell.....	143
<b>Figure 4.25:</b> Performance metrics for the GaInP/InGaAs/Ge cell. Short circuit current density ( $J_{SC}$ ), open circuit voltage ( $V_{OC}$ ), maximum power ( $P_m$ ), fill factor (FF), and conversion efficiency (Efficiency) are listed.....	143

**Figure 4.26:** Physical structure and equilibrium band diagram of a GaInP(red)/InGaAs(green)/GaTIP(blue) triple junction cell.....144

**Figure 4.27:** Structural parameters of GaInP/InGaAs/GaTIP cell.....145

**Figure 4.28:** J-V and P-V curves for the GaInP/InGaAs/GaTIP cell.....145

**Figure 4.29:** Performance metrics for the GaInP/InGaAs/GaTIP cell. Short circuit current density ( $J_{SC}$ ), open circuit voltage ( $V_{OC}$ ), maximum power ( $P_m$ ), fill factor (FF), and conversion efficiency (Efficiency) are listed.....145

**Figure 4.30:** Physical structure and band diagram of a GaInP(red)/AlGaAs(green)/GaTIP(blue) triple junction cell.....146

**Figure 4.31:** Structural parameters of GaInP/AlGaAs/GaTIP cell.....147

**Figure 4.32:** J-V and P-V curves for the GaInP/AlGaAs/GaTIP cell.....147

**Figure 4.33:** Performance metrics for the GaInP/AlGaAs/GaTIP cell. Short circuit current density ( $J_{SC}$ ), open circuit voltage ( $V_{OC}$ ), maximum power ( $P_m$ ), fill factor (FF), and conversion efficiency (Efficiency) are listed.....148

**Figure 4.34:** Physical structure and equilibrium band diagram of a GaSb single junction cell.....148

**Figure 4.35:** Structural parameters of GaSb cell.....149

**Figure 4.36:** J-V and P-V curves for the GaSb cell with truncated (left) and full (right) spectrum illumination.....149

**Figure 4.37:** Performance metrics for the GaSb cell. Short circuit current density ( $J_{SC}$ ), open circuit voltage ( $V_{OC}$ ), maximum power ( $P_m$ ), current at maximum

power ( $I_m$ ), voltage at maximum power ( $V_m$ ), fill factor (FF), and conversion efficiency (Efficiency) are listed.....149

**Figure 4.38:** Performance metrics for the GaInP/InGaAs/Ge cell with a  $Si_3N_4$  ARC. Short circuit current density ( $J_{SC}$ ), open circuit voltage ( $V_{OC}$ ), maximum power ( $P_m$ ), fill factor (FF), and conversion efficiency (Efficiency) are listed...151

**Figure 4.39:** EQE of GaInP/InGaAs/Ge cell without (left) and with (right) a  $Si_3N_4$  ARC.....151

**Figure 4.40:** Performance metrics for the GaInP/InGaAs/GaTIP cell with a  $Si_3N_4$  ARC. Short circuit current density ( $J_{SC}$ ), open circuit voltage ( $V_{OC}$ ), maximum power ( $P_m$ ) fill factor (FF), and conversion efficiency (Efficiency) are listed....151

**Figure 4.41:** EQE of GaInP/InGaAs/GaTIP cell without (left) and with (right) a  $Si_3N_4$  ARC.....152

**Figure 4.42:** Performance metrics for the GaInP/AlGaAs/GaTIP cell with a  $Si_3N_4$  ARC. Short circuit current density ( $J_{SC}$ ), open circuit voltage ( $V_{OC}$ ), maximum power ( $P_m$ ), fill factor (FF), and conversion efficiency (Efficiency) are listed...152



## Chapter 1 Introduction

One of the great problems that the modern world faces today is that of energy consumption and production. Electrical devices have become an integral part of our society, ranging from massive server farms located all over the world to humble light bulbs ubiquitous in our everyday lives. To power all of these devices requires a tremendous amount of energy. The vast majority of energy production comes from non-renewable sources. In 2006 in the United States, renewable energy production (including biomass, geothermal, hydroelectric, solar, wind, etc.) was only 6.9% of total energy production[28]. Naturally, as fossil fuel reserves are finite, there will come a point when alternative energy sources must be our primary source of energy. If, due to economic viability of these sources, that time comes before fossil fuels are depleted, then so much the better.

Solar cells, also called photovoltaic cells, show great promise in meeting the demands of world energy consumption by drawing on a virtually limitless resource. In 2006, worldwide consumption of electrical energy was  $4.98 \times 10^{20}$  J for the year, or  $1.58 \times 10^{13}$  W [29]. As a comparison, total solar radiation incident on the earth is 173,000 TW ( $1.73 \times 10^{17}$  W) [30]. This means that every 48 minutes, enough solar energy strikes Earth to power all of the electrical devices on the planet for an entire year. While a large percentage of the incident radiation is near impossible to collect, as it strikes deep ocean, intractable mountain ranges, or other inhospitable locations, even a small fraction, converted to electricity, would be sufficient to meet worldwide energy needs.

At this time solar cells have yet to achieve grid parity, where the cost per unit of energy produced by photovoltaics is equal to that of more traditional power supplies like coal, oil, and natural gas. This is due in large part to factors such as the high cost of materials and cell manufacturing, costs which many believe will decrease as the technology matures and becomes more prevalent. Adaptation of solar cells may turn out to be a highly regional process, as the amount of sunlight incident on different regions over the course of a year can vary greatly. Optimistically, up to ten different regions of the world could achieve grid parity by 2020, including the southwestern United States and large portions of Spain and Italy [31].

One of the most promising types of photovoltaic cell for achieving grid parity is the multijunction photovoltaic cell. In this cell, a number of different layers of material are grown sequentially, creating something akin to a ‘sandwich’ of a cell. Each layer of the cell absorbs a different range of frequencies of light, improving the overall efficiency of the cell. To offset the higher material and manufacturing costs multijunction photovoltaics have, these devices are typically used in conjunction with concentrating arrays, which shine light from a large area onto a much smaller. This keeps the materials and manufacturing costs for the cell lower.

In order for photovoltaic cells to reach their highest efficiencies, the materials in cell must absorb ranges of wavelengths of light that are ideally tailored to each other while still maintaining structural integrity. For the ideal three-junction case, there are two well-known and well-characterized materials

that can occupy two of the junctions. A complementary material for the final junction remains unfound, and it is the intention that this thesis may help fill that gap.

### **1.1 A Brief History of Photovoltaics**

The physical phenomenon central to solar cells is the photovoltaic effect, first identified by Antoine-César Becquerel in 1839. In his experiment, a solid electrode was placed in an electrolyte solution. When light shined on the electrode, an electrical voltage developed. For a while, this was regarded merely as an intellectual curiosity. It wasn't until 1883 that this phenomenon was applied with the intent of collecting solar energy, when Charles Fritts developed the first photovoltaic cell. Fritts' cell was composed by taking a sample of selenium and coating it with a thin layer of gold. This very basic cell was capable of converting 1% of incident light energy into electrical energy [32].

The first published photovoltaic cell was developed in 1954 by Chapin, Fuller, and Pearson at Bell Laboratories [33]. This cell, a simple p-n junction, only managed to convert 6% of incident solar energy into electrical energy, a meager sum by modern standards. This cell demonstrated that it was indeed possible to convert solar energy into electrical energy. A number of practical applications were quickly identified for this technology. One of the most notable of these applications was use in satellites. As a power source for these devices, solar cells have a number of distinct advantages, one of the largest being that a chemical or material fuel was not required, drastically decreasing the weight of

the satellites (due to a lack of fuel) while increasing their lifetime (since there is no periodic need to refuel). These benefits led to solar cells being incorporated into satellites as early as in the Vanguard I in 1958 [34]. Additionally, and perhaps more importantly, it was posited that the design of this cell could be significantly improved upon to increase its efficiency, such that more energy could be converted from solar radiation into electricity.

From that point, photovoltaics have been the focus of intense research. This research has produced constant advances in the field, both in terms of improved efficiency of the cells as well as exciting and innovative new designs. Figure 1.1 shows some of the progress that photovoltaics have made in the last 30 years. Whereas the first photocell had an efficiency of only 6%, today labs have produced individual cells with efficiencies over 40%, a dramatic improvement from where the technology started [35]. Despite this marked improvement, there are still prospects for improving photovoltaic efficiency even further in each existing technology.

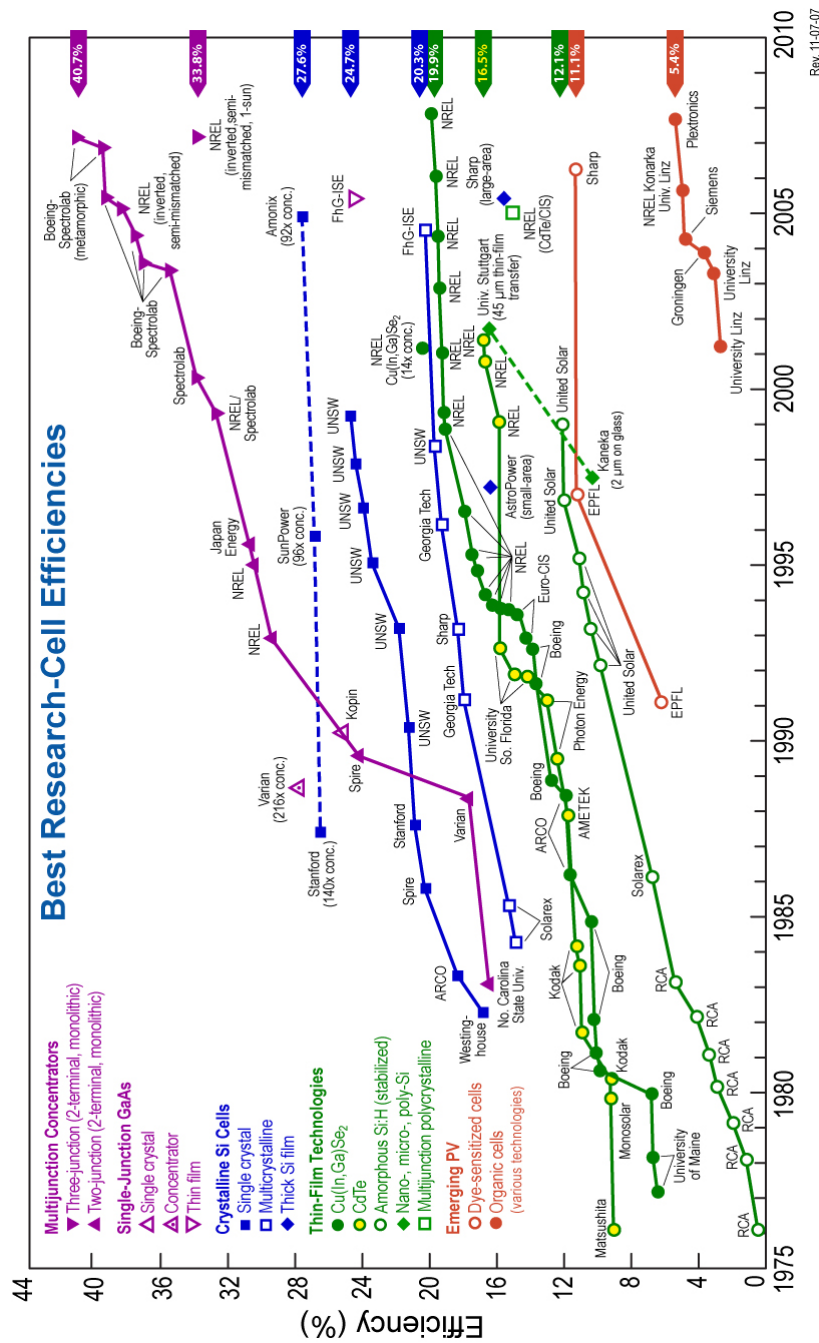


**Figure 1.1:** Conversion efficiency of photovoltaic cell type by year. As time has advanced, the efficiency of each technology has gradually improved [1]. Each improvement in efficiency brings the technology another step closer to economic viability.

## 1.2 The Physics of Solar Cells

### 1.2.1 The Solar Spectrum

Light radiated by the Sun into space is composed of a range of different wavelengths of light of various intensities. Travelling through space, light experiences almost no loss. Thus, the spectrum at the edge of Earth's atmosphere is virtually the same as that emitted by the Sun and is designated AM0, for air mass 0. This spectrum can be seen in Figure 1.2. As the light passes through the atmosphere, the spectrum is attenuated proportionally to the distance the light travels through the atmosphere. Additionally, while all wavelengths are attenuated to some extent, some wavelengths are significantly more attenuated than others. This inequity is due to absorption of light by the various components of the atmosphere, such as oxygen, water vapor, ozone, et al [3].

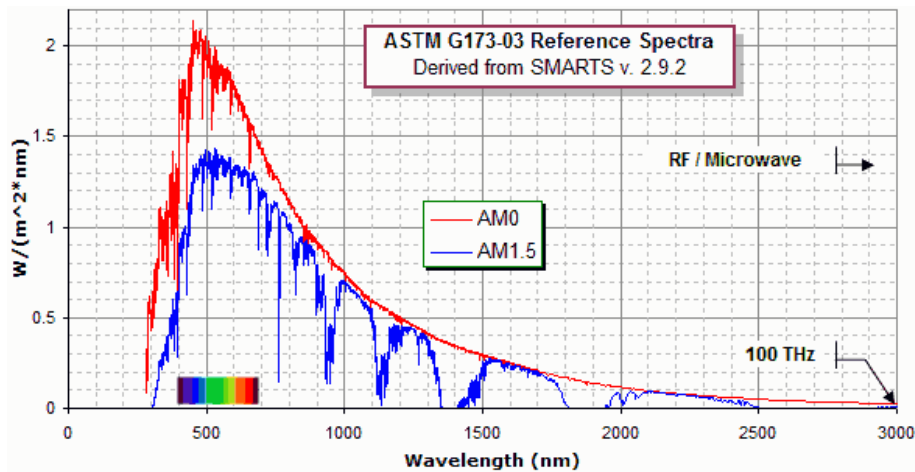


**Figure 1.2:** Spectral intensity vs. wavelength of light present under different atmospheric conditions. AM0 corresponds to outside of Earth's atmosphere and AM1.5 corresponds to typical atmospheric conditions at Earth's surface [2].

The total degree of attenuation of the AM0 spectrum is determined by the total distance the light must travel through the atmosphere. This distance can change

depending on the angle of incidence of the Sun's rays on the testing apparatus, which is dependent on factors such as the location's latitude, altitude, season, etc. This is done with the use of known air mass referencing spectra. In this system, the air mass spectrum,  $AM(m)$ , is determined by Equation 1.1:

$$m = \frac{h}{h_0} \quad 1.1$$

where  $h$  is the distance the light actually travels through the atmosphere. If the light travelled to sea level directly perpendicular to the Earth's surface, this would correspond to AM1. Additionally, when  $h$  comes in at an angle of incidence of  $\theta$ , it can be rewritten as Equation 1.2:

$$h = h_0 \sec \theta \quad 1.2$$

which leaves Equation 1.3:

$$m = \sec \theta \quad 1.3$$

A visual representation of this can be seen in Figure 1.3. As a standard, most photovoltaics are tested using the AM1.5 spectrum, shown in Figure 1.2.

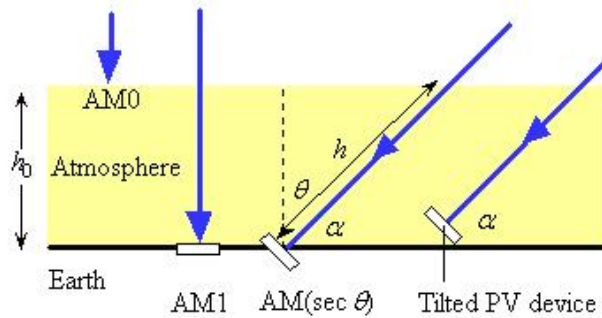


**Figure 1.3:** An illustration of the dependence of the AM spectra on angle of incidence of light and the distance the light travels through the atmosphere. AM0 and AM1 are included as a reference [3].

### 1.2.2 Relevant Physics of Light

In the course of this thesis, it is often more convenient to consider light in the sense of a particle as opposed to a wave. This is done so that the interaction of light with the individual of atoms of a semiconductor lattice is more readily understandable. Additionally, it is more convenient to consider the energy of a photon in terms electron-volts as opposed to Joules. With some rearranging of the photon energy equation and combining various constants and conversion factors, Equation 1.4 is produced:

$$E(eV) \approx \frac{1.24}{\lambda_o} \quad 1.4$$

where  $\lambda_o$  in measured in  $\mu\text{m}$  [4]. In general, light in the course of this paper will be referenced by its energy in electron-volts, as opposed to the more familiar wavelength or frequency, for later simplicity. For reference, a comparison of light wavelength/frequency and light energy is provided in **Error! Reference source not found.**

### 1.2.3 The Photovoltaic and Photoelectric Effects

Both the photovoltaic and photoelectric effects are central to the operation of a solar cell. The photovoltaic effect, first explained by Albert Einstein in 1905, is most well-known for introducing the concept of the photon to science. For photovoltaic cells, it has a much more direct application. In this phenomenon, monochromatic light is shined on a sample of metal. When the frequency of light is below a certain value intrinsic to the material, known as the work function, incident light does not produce a current. Above the work function, incident light

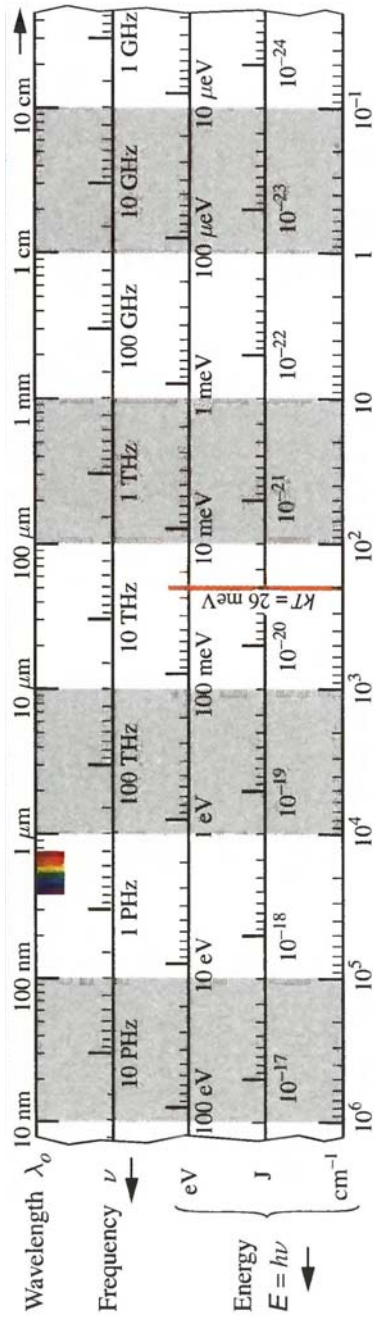


**Figure 1.4:** A comparison of wavelength/frequency of light and the energy of the photons that compose that light (in both J and eV). The wavelengths of the

visible light spectrum are denoted by the small spectra in the upper left of the diagram [4].

produces an electric current in the material, and this is the aspect of the photoelectric effect photovoltaic cells make use of [6].

The photovoltaic effect is based on a slightly different, but closely related, principle. When two materials with different electrical properties meet at an interface, there is a distinct possibility that the electric charge will flow more easily through one of the materials than the other. In this case, there can be a buildup of charge near that interface, resulting in an electric potential across the interface [36].

### **1.3 Semiconductor Physics and Band Theory**

The interaction of light and semiconductor materials forms the basis of the majority of this paper. In the case of many semiconductors, it is simpler to consider the physical interactions of light with the semiconductor crystal as a whole, as opposed to with the individual atoms of the semiconductor. From this viewpoint, a system under consideration is generally viewed as being composed of the lattice as a whole, carriers (electrons and holes), and any input energy (solar, thermal, etc.). A brief overview of semiconductor physics and band theory, which are relied on heavily to describe the results produced in this paper, follows.

#### **1.3.1 Lattice Constants**

Most semiconductor materials used for photovoltaic devices have a crystalline structure. In a crystalline structure, a three-dimensional structure of atoms, called a unit cell, is repeated in each direction. The length of the unit cell in each Cartesian direction is the lattice constant for that direction, with those values not necessarily being equal. In the case of many semiconductor materials, their lattice structure is either cubic or a cubic derivative (face-centered cubic, body-centered cubic, hexagonal close-packed structure, diamond, etc.). In this case, the lattice constants in each direction are approximately equal, and so are characterized by a single lattice constant. This lattice constant describes the average distance between two atoms in a semiconductor lattice[3].

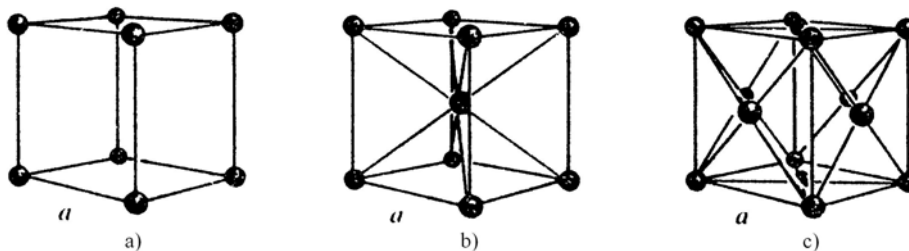


**Figure 1.5:** Sample models of a) simple cubic, b) body centered cubic, and c) face centered cubic lattice structures [3].

### 1.3.2 Valence and Conduction Bands

In any atom, there are a number of different, discrete energy states that any given electron can fill. Due to the Pauli Exclusion Principle, electrons under no external stimulation will fill the lowest available energy state not occupied by another electron. To fill that state, the electron must have the same energy as that state, with the outer-most group of states that contains at least one electron is referred to as the valence states. If a material has an incomplete valence shell, in

general the outermost filled  $s$ - and  $p$ -orbital, it will form chemical bonds with another material, sharing electrons to fill its valence shell [37].

In semiconductors, when a large amount of atoms bond to form a lattice, all of the valence energy states are at approximately the same level. If the lattice is large enough, it can be assumed that all electrons between some minimum and maximum energy will be accepted into the valence shell of some atom in the lattice. This region is referred to as the valence band. A similar phenomenon occurs with the set of completely unfilled energy states with the next highest energy, forming the conduction band. Generally, there will be some separation between the highest energy state in the valence band and the lowest energy state in the conduction band. This separation is called the band gap and its size varies between materials, a crucial fact utilized in this research. Electrons which have energies in this region cannot be captured by an atom in the lattice and so are not allowed. Electrons with energies in this disallowed region must either gain some energy to reach a state in the conduction band or lose some energy to reach a state in the valence band [4]. A diagram of this is provided in Figure 1.6.

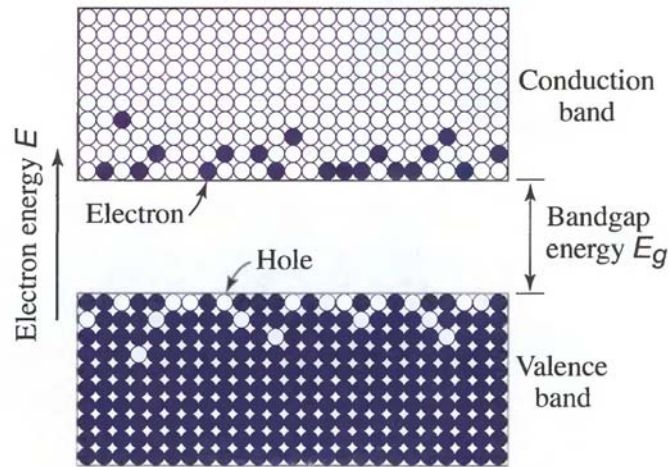


**Figure 1.6:** Electrons filling the available states in a semiconductor at an arbitrary temperature  $T > 0^\circ \text{K}$ . Each circle represents an available energy state and each filled circle represents an electron [4].

### 1.3.3 Band Interactions

When there is no input energy to the system (i.e. at  $T = 0^\circ \text{K}$ ), all electrons in a perfect semiconductor are contained in states in the valence band, implying that they are shared between atoms of the semiconductor in a chemical bond. Additionally, due to the bonds between the atoms of the semiconductor, all of the valence states in the material are filled and all states in the conduction band are empty. However, suppose a single electron in a semiconductor lattice absorbs a large enough packet of energy, whether from heat, light, etc., that the chemical bond holding it is broken and it can cross the band gap to fill a state in the conduction band. In this case, the electron is referred to as a carrier, the energy state the electron vacates is referred to as a hole, and the process as a whole is referred to as carrier generation. Additionally, it is simple to see that the carrier electron acts electrically as though it has the charge of an electron. The hole, as it

is considered the absence of an electron, acts in the opposite manner, as though it has an electrical charge opposite to that of an electron [7].

This reaction has a number of important consequences. First, the energy state the excited electron previously occupied is left empty. There is a possibility that the excited electron, after absorbing enough energy to rise into the conduction band, will relax back into the state it just vacated, reemitting the energy it just absorbed. The electron itself, no longer held in a chemical bond between two adjacent atoms, is able to drift freely through the lattice. As it drifts away from its original location, it is unable to relax to a lower energy state as there are no unoccupied states in the valence band. There is the possibility the carrier may collide with another electron in a state in the valence band, dislodge from its energy state, and relax into that lower energy state, but the result of this process is that dislodged electron replaces the carrier in the conduction band and becomes a carrier itself in a process known as photon recycling [38].

Simultaneously, the hole also ‘moves’ through lattice, though in a different way than the excited electron. When the electron was excited from the valence band, it left an atom in the semiconductor lattice with an unfilled valence shell. There is the possibility that a nearby electron in a valence energy state between two separate atoms in the lattice will move into this vacated energy state, in doing so leaving an empty energy state behind. In doing so, the hole is said to ‘move’ through the lattice as the process is repeated.

The only way a carrier electron in the conduction band or a hole in the valence can be removed is if, in moving through the lattice, they come across their

counterpart. If this occurs, the electron can relax to the lower energy state of the hole, releasing energy in the form of light, heat, etc., in a process called recombination. After this occurs, another burst of incident energy is required to create another electron-hole pair [7].

### 1.3.4 The Kronig-Penney Model

A more in-depth examination of how electrons act in a semiconductor lattice is necessary to explain some of the phenomenon that occur. In order to do so, the electron cannot simply be viewed as a particle, but also as a wave, i.e. quantum mechanics are required. In quantum mechanics, a particle is represented by a wave function  $\psi(\mathbf{r},t)$ , where  $\mathbf{r}$  is a location in three dimensions and the magnitude of the wave function at a given time and location is considered the probability the particle will be at location, or probability amplitude. The wave function is governed by the Schrödinger Equation, which it must satisfy at all times and locations, reproduced in Equation 1.5.

$$i\hbar\psi(\mathbf{r},t) = -\frac{\hbar^2}{2m}\nabla^2\psi(\mathbf{r},t) + V(\mathbf{r},t)\psi(\mathbf{r},t) \quad 1.5$$

Here,  $m$  is the mass of the particle,  $\hbar$  is Planck's constant multiplied by  $2\pi$ , and  $V(\mathbf{r},t)$  is the external potential acting on the particle.

The Kronig-Penney model is used to solve the Schrödinger equation for an electron in a semiconductor lattice. In this case, the external potential felt by an electron is due to a periodic potential from the nuclei of the atoms in the semiconductors. In the Kronig-Penney model, the actual potential experienced by the electron is approximated by an idealized potential. To further simplify the

problem, only one dimension is considered at first, and the solution is then extended to three dimensions. In this approximation,  $V(\mathbf{r},t)$  is approximated by a periodic potential that could best be described as a square wave. One portion of the wave has a potential of zero and length  $a$ , representing when the electron is far from any atomic nucleus, and the other a magnitude of  $V_0$  for a length  $b$ , representing when the electron is close to an atomic nucleus. Additionally, the sum of  $a$  and  $b$  should be equal to the lattice constant. A diagram of this potential in the one-dimensional case can be found in Figure 1.7.

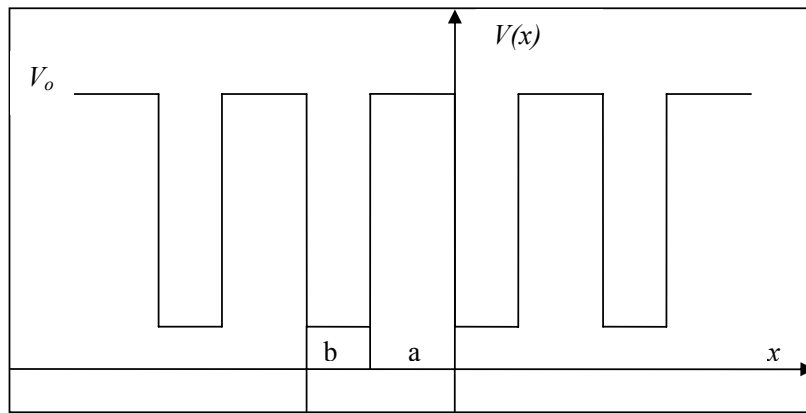


**Figure 1.7:** A model of the periodic potential well utilized in the Kronig-Penney model [5].

The solution for  $\psi(x)$  in this one dimensional case is supplied by the Bloch Theorem, and has the form of Equation 1.6:

$$\psi_k(x) = e^{ikx} \varphi_k(x) \quad 1.6$$

where  $k$  is the propagation vector of the wavefunction on the axis considered and  $\varphi(x)$  is a periodic function associated with the periodic potential described above. When this wavefunction is inserted into the Schrödinger equation, the following result can be produced as in Equations 1.7-1.9:

$$-\frac{(\alpha^2 + \beta^2)}{2\alpha\beta} \sin(a\alpha) \sin(b\beta) + \cos(a\alpha) \cos(b\beta) = \cos(ka + kb) = \cos(Lk) \quad 1.7$$

$$\alpha^2 = \frac{2mE_n}{\hbar^2} \quad 1.8$$

$$\beta^2 = \frac{2m(E_n - V_o)}{\hbar^2} \quad 1.9$$

where  $E_n$  is the energy of the electron. A plot of this equation, under the simplification where the periodic potential wells are modeled as  $\delta$ -functions, is supplied in Figure 1.8 [5].

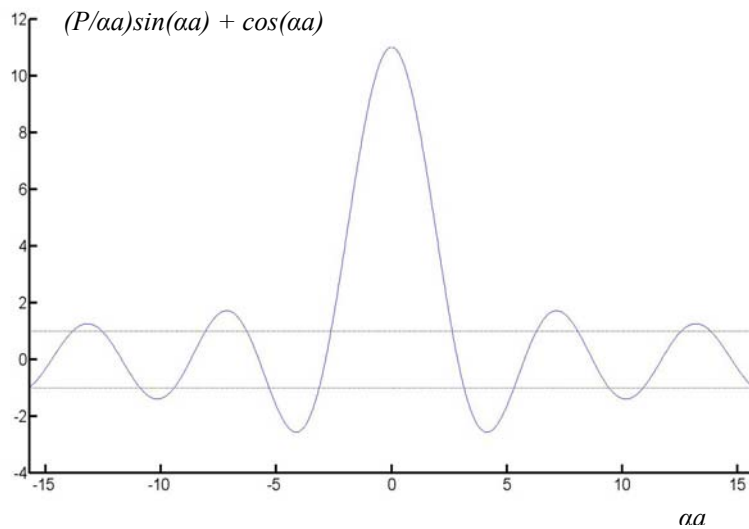


**Figure 1.8:** An example plot of a simplification of the left hand side of the solution to the Kronig-Penney model. Only the values for this equation valued between +1 and -1 are valid as per the right hand side of the solution. P is an aggregation of the variables listed above.

There are two important realizations that can be made from this equation. The first is that  $\cos(Lk)$  can only take values between -1 and 1, where has the left-hand side of the equation can take values outside this range. When the left-hand side of the equation takes a value outside of this accepted range, it is said to represent a

disallowed state. These states represent the bandgaps present in the allowed energy levels of an atom, one of which, the gap between the valence band and the conduction band, has been mentioned before. The other is that the allowed energy state of an electron is partially dependent on the propagation vector of that electron. While this example is confined to one direction, and so one propagation constant, when it is extended to three dimensions, there are also three associated propagation constants which also must be satisfied. That is, each energy state not only has a fixed energy level that is allowed, but also a fixed set of propagation constants that also must be satisfied [5].

### **1.3.5 Indirect Gap vs. Direct Gap**

The realization that the allowed energy states in a semiconductor only allow certain propagation constants allow us to separate semiconductors into two groups in terms of this research: direct bandgap and indirect bandgap materials. For direct gap materials, the transition between the highest energy valence energy state and the lowest energy conduction state requires no change in the propagation vector associated with an electron. In an indirect gap material, the minimum energy transition between the bands does require a change in the propagation vector of the electron. The plot of the band structure of both an indirect bandgap and a direct bandgap material can be found in Figure 1.9.

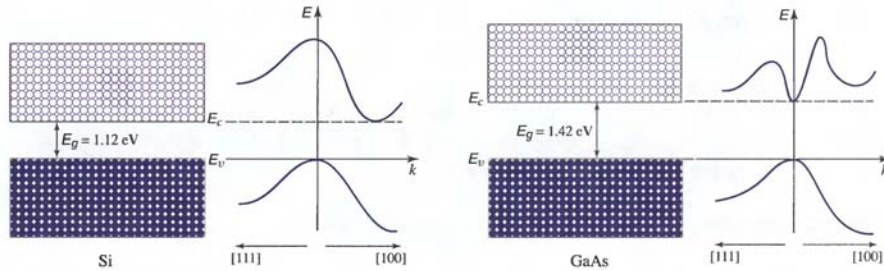


**Figure 1.9:** Cross section of the E-k band structure for Si (an indirect gap material) and GaAs (a direct gap material) in the [111] direction (left side of each plot) and the [100] direction (right side of each plot) [4].

In direct gap materials, the interaction of electrons and photons is fairly simple. Should the photon be of sufficient energy, the electron can absorb it and rise into the conduction band. Since this transition requires no change in wave vector to occur, this transition is likely to occur. In indirect materials, the process is more complicated. There are two main methods that an electron in an indirect gap material can reach the conduction band. In the first, an electron absorbs both a photon and a phonon simultaneously, a particle that exists in a lattice due to lattice vibrations which has high momentum (and so is able to alter another particle's wave vector) but low energy. A three-body reaction is highly unlikely to occur, making this sort of reaction fairly rare. The other possibility is that the electron absorbs a photon of high enough energy to raise it to the conduction band without needing to change its wave vector. Since the conduction band is composed more of empty energy states than filled ones (e.g. in intrinsic crystalline silicon, there are on the order of  $1.08 \times 10^{10}$  electrons/cm<sup>3</sup> in  $2.86 \times 10^{19}$  states/cm<sup>3</sup> [7]) it's all but certain that the electron will relax to a lower energy level in the conduction band. In doing so, it releases energy in the form of a lower energy photon and a phonon to reach the lowest available energy state in

the conduction band. The release of photons represents a significant loss of energy that was initially absorbed, and in the case of photovoltaics would represent a significant loss in conversion efficiency. Additionally, the release of phonons can cause increase lattice vibrations in the structure, which leads to an increased temperature in the photovoltaic cell. Should this occur to a large extent, it is possible to overheat the cell. Regardless of type of material, excited electrons will relax to the lowest unoccupied energy level in the conduction band. Should it be excited from this state in either of the processes described above, it would revert back to the lower energy state [7].

### 1.3.6 Effective Mass of Carriers

The value for the mass of an electron most commonly used, approximately  $9.11 \times 10^{-31}$  kg, is more precisely the mass of a free electron. When an electron is unconfined, Equation 1.10 is used to relate the particle's energy, momentum, and mass.

$$E = \frac{p^2}{2m} = \frac{k^2 \hbar^2}{2m} \quad 1.10$$

In the case of a free electron, its mass is constant. This implies a very specific relationship between the electron's energy and wave number, i.e. that the energy of the electron is a quadratic function with respect to the electron's wave number.

When carrier electrons, which are confined in the lattice of a semiconductor, are considered, the allowed energy states available are different than when unconfined. Instead, the mass of a carrier electron in the material is governed by Equation 1.11:

$$\frac{1}{\hbar^2} \frac{d^2 E}{dk^2} = \frac{1}{m^*} \quad 1.11$$

where  $m^*$  is the effective mass of an electron. Being mindful that, as per the Kronig-Penney model, the energy of an electron is a rather complicated function with respect to its wave number, it is clear to see that the mass of an electron in a semiconductor not only is different than when unconfined, but is also no longer constant. When the electron is in a region of the band structure that is relatively steep, the mass of the electron will be smaller and lighter, and vice versa.

The above relationship also holds when considering the effective mass of a hole in the semiconductor as well. As the hole is really the absence of an electron, it is little surprise that the particle acts in a similar manner. One important distinction to make between the two is arises from the band that each particle is in. The carrier electrons reside in the conduction band, and due to that band's curvature have positive mass. Meanwhile, the holes reside in the valence band, and due to that band's curvature have negative mass [6].

### **1.3.7 Diffusion and Drift Current Densities**

There are two mechanisms through which carriers (both holes and carrier electrons) move through a semiconductor lattice: diffusion and drift. The motion of carriers due to each of these mechanisms gives rise to an associated current density, i.e. a diffusion current density and a drift diffusion density, with the sum of the two totaling the full current density through the semiconductor. The properties of these current densities are examined in this section.

### 1.3.7.1 Diffusion Current Density

Diffusion current, as its name implies, is dependent upon the process of diffusion that all particles experience. In diffusion, any particle, regardless of charge, mass, or any other characteristic, has equal likelihood of moving in any direction from where it is located. If we consider two adjacent regions of equal size, but different densities of a given particle an important result becomes clear. The probability that any given particle in the high density region will move to the low density is the same as for a particle moving from the low density region to the high density region. Since there are a larger number of particles present in the high density region, there will, on average, be a net movement of particles from the high density region to the low density region. Should this particle be a charged particle, then this net movement of particles will result in a diffusion current density. In the case of a semiconductor, both types of carrier present have a respective diffusion current. The value of the electron diffusion current through a given volume of material is given by Equation 1.12:

$$J_{n(diff)} = qD_n \nabla n(x, y, z) \quad 1.12$$

while the hole diffusion current is given by Equation 1.13:

$$J_{p(diff)} = -qD_p \nabla p(x, y, z) \quad 1.13$$

where  $q$  is the charge of an electron,  $D_n$  and  $D_p$  are the associated diffusion coefficients for electrons and holes, respectively, and  $n$  and  $p$  are the 3-dimensional density distributions of the electrons and holes, respectively.

### 1.3.7.2 Drift Current Density

The other portion of current density that is present in a semiconductor arises from external applied forces. As both types of carriers in a semiconductor behave as though they have charge, negative for electrons and positive for holes, should an electric field be applied across the semiconductor, the carriers will move in response to it. This current, called the drift current, is defined for carrier electrons as Equation 1.14:

$$J_{n(drift)} = q\mu_n nE \quad 1.14$$

and for holes as Equation 1.15:

$$J_{p(drift)} = q\mu_p pE \quad 1.15$$

where  $\mu_n$  and  $\mu_p$  are the electron and hole mobilities, respectively,  $n$  is the concentration of electrons,  $p$  is the concentration of holes, and  $E$  is the magnitude of the applied electric field. The electron and hole mobilities are simply a measurement of how quickly the carrier can move through a given material and is usually determined experimentally for a material over a range of temperatures. Additionally, electron and hole mobilities are not necessarily equal in magnitude, and in fact are so only rarely[7].

### **1.3.8 The Fermi Level and the Fermi-Dirac Probability Function**

The Fermi level is a powerful conceptual tool in understanding complicated multijunction semiconductor devices. It is utilized the Fermi-Dirac probability function to help determine the probability of a given energy state being filled in a semiconductor material, provided that a state exists at that energy level. The Fermi-Dirac probability function is defined in Equation 1.16:

$$f(E) = \frac{1}{1 + e^{(E-E_f)/kT}} \quad 1.16$$

where  $E$  is the energy level of an allowed state,  $E_f$  is the Fermi level,  $k$  is the Boltzmann constant, and  $T$  is the temperature. A plot of a Fermi-Dirac distribution is shown in Figure 1.10. The Fermi level is chosen for a material such that at the Fermi level the probability an electron would fill a state at that energy level in an intrinsic semiconductor would be  $\frac{1}{2}$ . The rest of the probability function is centered on this reference point. It should be noted, though, that nearly always there is not an available energy state at the Fermi level, it is used more as a reference level for comparison between materials.

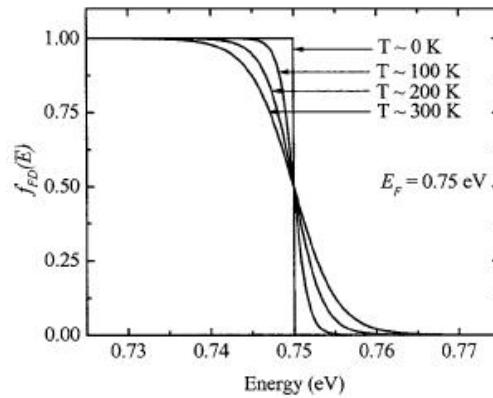


**Figure 1.10:** The Fermi-Dirac probability function evaluated for a number of different temperatures for a particular semiconductor device [5].

In a homogeneous, intrinsic material, the Fermi level will be at the midpoint of the bandgap of the material. In a doped material, the addition of carriers by dopant atoms changes the probability that an electron will fill a state at a given energy level. In a n-type material, there are excess carrier electrons added to the material, resulting in a much higher probability of higher energy states,

such as those in the conduction band, being filled. In a p-type material, the opposite is true, where added holes make it less likely a conduction band energy state will be filled. In these materials, the shape of the distribution will still follow the Fermi-Dirac probability function centered on the Fermi level, which is constant, so to take into account the change of probability of which states are filled the conduction and valence bands shift around the Fermi level [7], as seen in Figure 1.12.

### **1.3.9 Other Intrinsic Characteristics**

There are a handful of other useful characteristics of semiconductors that are innate to each material. The vacuum energy level,  $E_{vac}$ , is the energy level at which an electron no longer held by an atom in the lattice, that it is a free electron. The ionization energy,  $\gamma$ , of a material is the energy it takes to move an electron from the uppermost edge of the valence band to  $E_{vac}$ . The work function,  $\Phi$ , is the energy required to move from the Fermi level to  $E_{vac}$ . Finally, the electron affinity,  $\chi$ , is the energy needed to move from the lower edge of the conduction band to  $E_{vac}$ . These characteristics are innate to a given material and will not change based on doping or external electric field [7]. A chart illustrating these values is shown in Figure 1.14.

### **1.3.10 Doping**

The semiconductors that have been discussed to this point have all been intrinsic materials, where the lattice is composed entirely of a given material. Besides intrinsic materials there are also doped materials, wherein specific impurities are introduced to a semiconductor lattice. While these impurities comprise only a small percentage of the total lattice, they can significantly alter the characteristics of the material.

There are two types of doping, which are typically in complementing each other. In n-type doping, atoms of a material with an additional electron than the substrate material are introduced to the semiconductor lattice. The dopant atom will then form enough bonds with surrounding substrate atoms to fill its valence shell, usually in a geometry consistent with that dictated by the substrate material. In doing so, the dopant is generally left with an extra electron, which remains unbonded. As all the valence shell states in the dopant material are filled by electrons in bonds with other atoms in the lattice, this extra electron is held in an energy state in the conduction shell of the dopant material. This electron is held loosely enough that it can almost immediately act as a carrier electron without requiring significant external excitation to the conduction band.

In p-type doping, the opposite is done. Atoms of a material with one fewer electron than the substrate material are introduced to the substrate lattice. The dopant atom will attempt to form enough bonds to fill its valence shell in a manner consistent with the geometry of the lattice. Since the dopant atom does not have enough electrons to form sufficient bonds to have a full valence shell in the geometry of the lattice, the material will have an empty energy state present in

its valence shell. This empty energy state acts as a hole would. A diagram of a lattice of a n-type and a p-type doped material can be seen in Figure 1.11.

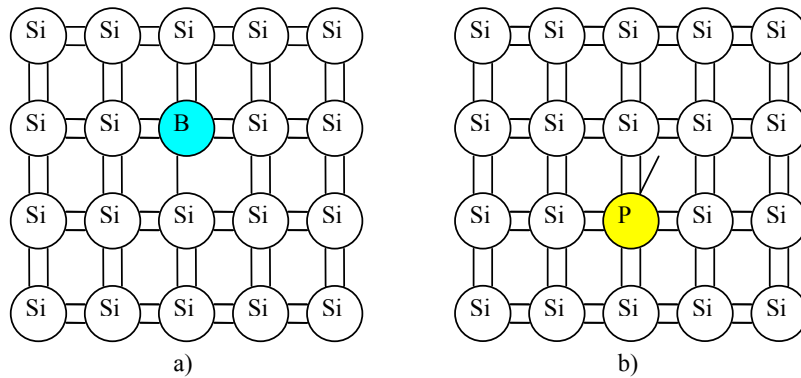


**Figure 1.11:** Silicon lattices doped with a) an acceptor material (Boron) and b) a donor material (Phosphorus).

Since the dopant materials will have a different band gap than the substrate material, though usually only by a small margin, they will create an allowed states in the forbidden region of the band structure of the lattice, as seen in Figure 1.12. An n-type material will create an available state just below the conduction band, whereas a p-type material will create an available state just above the valence band. As a result of these dopant states, the minimum energy required to move from the valence band to the conduction band would be slightly reduced, as the carriers could move between the dopant states and then into the valence or conduction band, as opposed to only moving between states in either valence or conduction band [7].

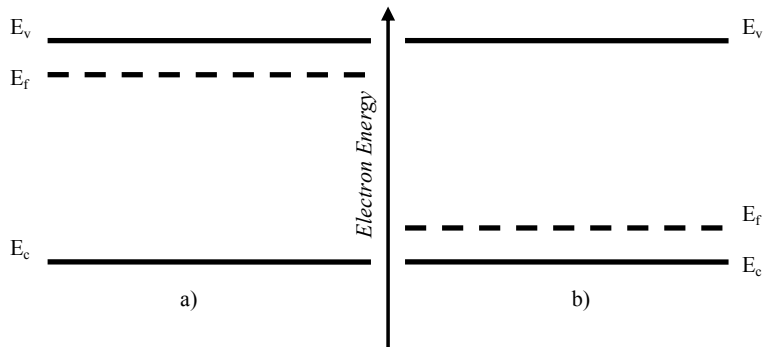


**Figure 1.12:** Energy states in the forbidden band of a semiconductor created by doping with a a) n-type (donor) material and b) p-type (acceptor) material.[6]

### 1.3.11 p-n Heterojunctions

When a region of p-type, uniformly doped material and a region of n-type, uniformly doped material of the same substrate come into contact, a p-n heterojunction is formed. This structure illustrates a number of important features of semiconductors. Each region has excess carriers of one type, electrons in n-type and holes in p-type. These carriers, due to the concentration difference between each region, will then begin to diffuse into the opposite region, electrons into the p-type region and holes into the n-type region. As this occurs, the carriers will combine with the dopants in the opposite region. In doing so, the carrier will be annihilated, but in doing so will leave a net charge on the dopant atom, positive in an n-type material and negative in a p-type. After annihilating the opposing carrier, the dopant atom will have a complete valence shell and because of that no longer contributes a carrier to the semiconductor as a whole, merely acting as a fixed charge at the interface of the two materials. The combined regions of fixed charge are known as the space charge region.

As the process of annihilation continues, the regions of fixed positive and negative charges grow larger, creating an increasingly strong electric field and, due to that field, a potential voltage. By Poisson's equation and the functional form of the electric field, provided in Equations 1.17 and 1.18:

$$\frac{dE}{dx} = \frac{Q(x)}{\epsilon} \quad 1.17$$

$$E = -\frac{dV}{dx} \quad 1.18$$

This electric field opposes the diffusion of the carriers across the space charge region and, once the space charge region is large enough, prevents carriers from crossing it completely. When this occurs, the space charge region stops growing and carriers are unable to cross into the opposite material anymore. At this point, the region is referred to as the depletion region, as it is very unlikely to find carriers in this region of the semiconductor, and the potential due to the electric field across the depletion region is known as the built-in voltage,  $V_{bi}$ . A qualitative sample comparing the fields in a p-n junction is supplied in Figure 1.13.

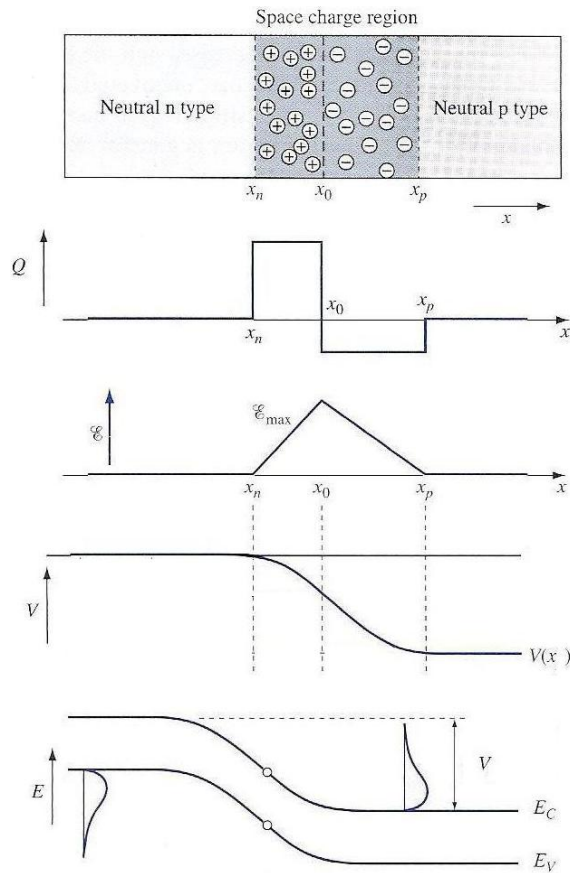


**Figure 1.13:** a) a physical diagram of a p-n junction, b) the distribution of charge, c) the electric field across the junction, d) the voltage across the junction, and e) the final band structure of the entire junction [7].

It should also be noted that the total positive fixed charge in the depletion region will equal the total negative fixed charge in the depletion region once equilibrium is reached. Should the doping concentrations on either side of the interface be equal, then the length of positive and negative portions of the depletion regions will be equal as well. Should this not be the case, then it follows that, since the charges in the depletion region are fixed, the region more lightly doped would



The carrier lifetime,  $\tau$ , and diffusion length,  $L$ , for carriers in a semiconductor are useful in understanding how well a semiconductor conducts current. The carrier lifetime is the average time that a carrier exists in a semiconductor, for electrons it applies to time spent in the conduction band and for holes time spent in the valence band. In a doped material, due to the excess of carriers of a particular type injected to the semiconductor by doping, typically only the minority carrier lifetime, the carrier not doped into the material, is considered. This can vary greatly depending on the type of material used, the purity of the material, and the doping concentration present and is typically found experimentally for a given material, as opposed to by calculation. Values for carrier lifetime can range from the order of milliseconds for a pure, undoped semiconductor to the order of nanoseconds for a heavily doped material. Additionally, direct gap materials tend to have much shorter carrier lifetimes than indirect gap materials, as the process of relaxation of carriers in those materials is much simpler.

Diffusion length refers to the average distance that a carrier will travel via diffusion while it exists. This is dependent on two properties of the semiconductor, the carrier lifetime, described above and the diffusion coefficient, heavily reliant on the mobility of the material. It is defined for electrons and holes respectively as in Equation 1.19:

$$\begin{aligned} L_n &= \sqrt{D_n \tau_n} \\ L_p &= \sqrt{D_p \tau_p} \end{aligned} \tag{1.19}$$

It should be noted that the diffusion lengths for electrons and holes are not necessarily equal [7].

### 1.3.13 III-V and II-VI Materials

While silicon is the most commonly used material in semiconductors, due to its availability and durability, there are a number of factors (indirect bandgap, band gap of non-optimal size, etc.) that make it a non-ideal material. This led to the development of alternative semiconductor materials as both replacements and supplements. The most well-known of these alternatives generally fall into either the III-V or II-VI categories, highlighted in Figure 1.15.

Periodic Table of the Elements

1 H 1.008																	2 He 4.00																												
3 Li 6.94	4 Be 9.01											5 B 10.81	6 C 12.01	7 N 14.01	8 O 16.00	9 F 19.00	10 Ne 20.18																												
11 Na 22.99	12 Mg 24.31											13 Al 26.98	14 Si 28.09	15 P 30.97	16 S 32.07	17 Cl 35.45	18 Ar 39.95																												
19 K 39.20	20 Ca 40.08	21 Sc 44.96	22 Ti 47.88	23 V 50.94	24 Cr 52.00	25 Mn 54.94	26 Fe 55.85	27 Co 58.93	28 Ni 58.69	29 Cu 63.55	30 Zn 65.39	31 Ga 69.72	32 Ge 72.61	33 As 74.92	34 Se 78.96	35 Br 79.90	36 Kr 83.80																												
37 Rb 85.47	38 Sr 87.62	39 Y 88.91	40 Zr 91.22	41 Nb 92.91	42 Mo 95.94	43 Tc (98)	44 Ru 101.0	45 Rh 102.9	46 Pd 106.4	47 Ag 107.8	48 Cd 112.4	49 In 114.8	50 Sn 118.7	51 Sb 121.7	52 Te 127.6	53 I 126.9	54 Xe 131.2																												
55 Cs 132.9	56 Ba 137.3	57 La 138.9	72 Hf 178.5	73 Ta 180.1	74 W 183.9	75 Re 186.2	76 Os 190.2	77 Ir 192.2	78 Pt 195.1	79 Au 197.0	80 Hg 200.6	81 Tl 204.4	82 Pb 207.2	83 Bi 209.0	84 Po (209)	85 At (210)	86 Rn (222)																												
87 Fr 223.0	88 Ra 226.0	89 Ac 227.0	104 Rf (261)	105 Db (262)	106 Sg (263)	107 Bh (262)	108 Hs (265)	109 Mt (266)	110 Ds (281)	111 Rg (272)	112 Uub (285)	113 Uut (284)	114 Uuq (289)	115 Uup (288)	116 Uuh (292)																														
<table border="1"> <tbody> <tr> <td>58 Ce 140.1</td> <td>59 Pr 141.0</td> <td>60 Nd 144.2</td> <td>61 Pm (145)</td> <td>62 Sm 150.4</td> <td>63 Eu 153.0</td> <td>64 Gd 157.3</td> <td>65 Tb 158.9</td> <td>66 Dy 162.5</td> <td>67 Ho 164.9</td> <td>68 Er 167.3</td> <td>69 Tm 168.9</td> <td>70 Yb 173.0</td> <td>71 Lu 175.0</td> </tr> <tr> <td>90 Th 232.4</td> <td>91 Pa 231.4</td> <td>92 U 238.0</td> <td>93 Np (237)</td> <td>94 Pu (240)</td> <td>95 Am (243)</td> <td>96 Cm (247)</td> <td>97 Bk (248)</td> <td>98 Cf (251)</td> <td>99 Es (252)</td> <td>100 Fm (257)</td> <td>101 Md (257)</td> <td>102 No (259)</td> <td>103 Lr (262)</td> </tr> </tbody> </table>																		58 Ce 140.1	59 Pr 141.0	60 Nd 144.2	61 Pm (145)	62 Sm 150.4	63 Eu 153.0	64 Gd 157.3	65 Tb 158.9	66 Dy 162.5	67 Ho 164.9	68 Er 167.3	69 Tm 168.9	70 Yb 173.0	71 Lu 175.0	90 Th 232.4	91 Pa 231.4	92 U 238.0	93 Np (237)	94 Pu (240)	95 Am (243)	96 Cm (247)	97 Bk (248)	98 Cf (251)	99 Es (252)	100 Fm (257)	101 Md (257)	102 No (259)	103 Lr (262)
58 Ce 140.1	59 Pr 141.0	60 Nd 144.2	61 Pm (145)	62 Sm 150.4	63 Eu 153.0	64 Gd 157.3	65 Tb 158.9	66 Dy 162.5	67 Ho 164.9	68 Er 167.3	69 Tm 168.9	70 Yb 173.0	71 Lu 175.0																																
90 Th 232.4	91 Pa 231.4	92 U 238.0	93 Np (237)	94 Pu (240)	95 Am (243)	96 Cm (247)	97 Bk (248)	98 Cf (251)	99 Es (252)	100 Fm (257)	101 Md (257)	102 No (259)	103 Lr (262)																																

Figure 1.15: The Periodic Table of Elements with groups III and V (yellow) and II-VI (blue) materials highlighted.

III-V materials are composed of elements from groups III and V from the periodic table. Most common among these are the binary materials, those made from two elements, one each from group III and group V, e.g. GaAs or InP. The two elements share their valence electrons, three from each group III element and five from each group V element, to form a lattice much in the same way silicon does.

In a general sense, these materials behave as silicon does for photovoltaics: the elements form a lattice, incident light excites electrons from the semiconductor's valence band to its conduction band, etc. Naturally, the specifics of how the material behaves (indirect vs. direct band gap, size of band gap, etc.) all depend on the materials used, but the basic premise remains the same. The strength of III-V materials is that there are numerous possible combinations of materials that all produce viable cells with different characteristics. This gives the technology great flexibility in single material photovoltaics as well as, as will be explained in detail below, multiple material photovoltaics. The materials used in III-V materials do tend to be significantly more expensive than silicon, one detriment to their use. Additionally, while III-V materials tend to be highly resistant to degradation from radiation, they also tend to be more fragile in terms of physical contact [39].

II-VI materials, composed of elements from groups II and VI (e.g. CdTe) of the periodic table are much like III-V materials, only to more of an extreme. As with III-V materials, there a number of different valid semiconductor materials that can be constructed using II-VI materials, each with varying characteristics.

Some combinations of II-VI materials, such as  $\text{Hg}_x\text{Cd}_{1-x}\text{Te}$  or  $\text{Cd}_x\text{Zn}_{1-x}\text{S}$  maintain very similar lattice constants while spanning a wide range of bandgaps, one of the strengths of this kind of material [40]. Also, the high optical absorption coefficients for these materials in general means only thin films are required to make effective photovoltaics [41]. That said, these cells face many of the same limitations as III-V cells. Cost to make the cells can be high, as the raw materials can be expensive and fine processing is required. Additionally, II-VI materials are incredibly fragile to physical contact, to the point where it can be difficult to manufacture a cell and place it in its desired location without damaging it [39]. There is also an issue concerning electrical contacts with many II-VI compounds, as there are surprisingly few low-cost materials capable of creating an ohmic contact with II-VI devices [40, 42].

#### **1.3.14 Ternary and Quaternary Materials**

Ternary and quaternary materials are an extension of III-V and II-VI materials. Whereas previously only binary materials were considered (e.g. GaAs or InP), in ternary materials semiconductors are composed of three materials. In these materials, typically two elements from the same group are paired with another element to form an alloy. The ratio of the materials from the same group can vary greatly with respect to each other, however the sum of the two must be equal to that of the remaining element in order to form a proper lattice, e.g.  $\text{Ga}_x\text{In}_{1-x}\text{As}$ .

Defining the characteristics of these materials can have interesting quirks. It is clear that, in the above example,  $x$  equals zero, the material would be characterized as simply InAs, and similarly as GaAs when  $x$  equals one. In between these known points, the band gap of the alloys generally fit a quadratic curve of the form of Equation 1.20:

$$G'_{ABC}(x) = (1-x)G_{AC} + xG_{BC} - x(1-x)D_{ABC} \quad 1.20$$

Where A, B, and C represent the alloy elements, G references the band parameter under consideration, and D is bowing parameter determined experimentally. The bowing parameter is usually positive, which implies that the actual band gap is lower than the projected linear interpolation of the two known points. A similar effect happens with the lattice constants of the alloy materials as well [43].

Quaternary materials act much as an extension of ternary materials. For III-V materials, they can have two kinds of compositions, one where there are two components each from group III and group V (e.g.  $\text{Ga}_x\text{In}_{1-x}\text{As}_y\text{P}_{1-y}$ ) and the other where one group has one component and the other has three components (e.g.  $\text{Al}_x\text{Ga}_y\text{In}_{1-x-y}\text{P}$ ). Regardless of which type a particular quaternary material falls into, the ratio of materials within each group can vary while the ratio of the sum of materials in each group should be nearly 1:1.

The expressions from material characteristics of quaternary materials understandably become increasingly complicated from ternary materials with the addition of another component. Additionally, each kind of quaternary material follows a different characterization. Using the notation for ternary materials

supplied above, the band parameters for a quaternary materials composed of two group III and two group V materials is defined as in Equation 1.21:

$$G_{ABCD}''(x, y) = \frac{x(1-x)[(1-y)G_{ABD}'(x) + yG_{ABC}'(x)] + y(1-y)[xG_{ACD}'(y) + (1-x)G_{BCD}'(y)]}{x(1-x) + y(1-y)} \quad 1.21$$

A sample plot of one of these materials is supplied in Figure 1.16.

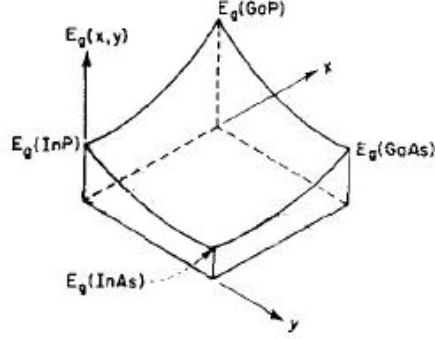


**Figure 1.16:** A plot of the band gap of  $\text{In}_{1-x}\text{Ga}_x\text{As}_y\text{P}_{1-y}$  over changing values for  $x$  and  $y$  [8].

For quaternary materials composed of three materials from one group (B, C, and D) and a fourth from the other (A) the band parameters are defined as in Equation 1.22 [43]:

$$G_{ABCD}''(x, y) = \frac{xyG_{ABD}'((1-x-y)/2) + y(1-x-y)G_{BCD}'((2-x-2y)/2) + (1-x-y)xG_{ACD}'((2-2x-y)/2)}{xy + y(1-x-y) + (1-x-y)x} \quad 1.22$$

One issue that can arise in some cases for some of these materials is that of miscibility. In the case of some alloys, the constituent parts may not fully intermix under typical growth conditions, leading to a final material which may behave unexpectedly. These materials come in two degrees, slightly immiscible and quite immiscible. In a slightly immiscible material, the constituents of the alloy will mix at a sufficiently high temperature, occurring while the alloy is still

solid. In quite immiscible alloys, this temperature does not occur until the alloy is on the verge of melting, if not already melted [44].

### 1.3.15 Lattice Matching and Mismatch Strain

At an interface between two different materials, there are a number of considerations that must be taken into account in order to assure the photovoltaic cell's effectiveness. One of the most important considerations for multijunction photovoltaics is lattice matching. If there is any mismatch at all between the lattice constants of the two layers, there will be strain. Should the lattice constants be very nearly the same, then the strain will not be sufficient to alter the either lattice structure of the cell, which could then perform as intended. Should there be a significant difference between the two, then the strain would be sufficiently large to cause dislocations, defects, and other efficiency damaging structures in the lattice of the photovoltaic cell.

At the lattice interface, the lattice mismatch, or lattice misfit, is defined as in Equation 1.23:

$$\frac{\Delta a}{a} = \frac{a - a_o}{a} = -f \quad 1.23$$

Where  $a_o$  is the lattice constant of the substrate material and  $a$  is the lattice constant of the epitaxial layer. This misfit can be used to estimate the maximum layer thickness an epitaxial layer can have without developing defects. This thickness, known as the critical thickness, is defined as in Equation 1.24:

$$h_c \cong \frac{a}{2f} \quad 1.24$$

If the deposited layer of material is less than this thickness, then there will be no defects in the material. The mismatch will only be exhibited in strain in the crystal, as can be seen in Figure 1.17. Should an epitaxial layer be thicker than this critical width, then the strain on the lattice will be sufficient to cause at dislocations or worse, as can be seen in Figure 1.18. A cursory examination of this equation shows that there isn't a great deal of leeway in terms of difference between lattice constants if layers of appreciable thickness must be grown. A lattice mismatch of only 1% can limit the critical thickness of an epitaxial layer to only a few hundred angstroms, depending on the material. A layer this thin, regardless of material, is unusable for a photovoltaic device [45].

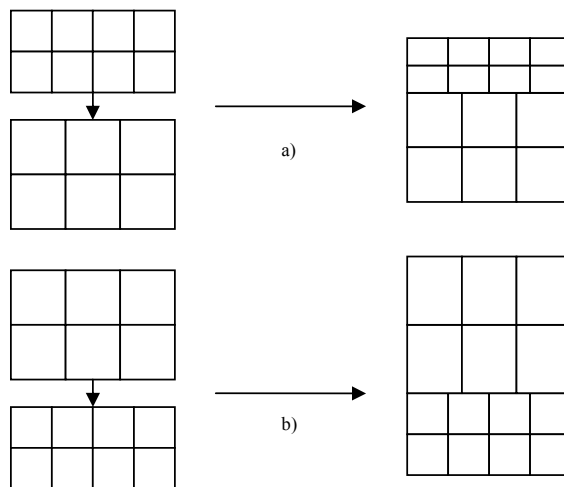


**Figure 1.17:** When lattice mismatching is small, the only effect is strain on the materials, instead of defects. Both a) biaxial compressive strain (when the lattice constant of the epitaxial layer is greater than that of the substrate layer) and b) biaxial tensile strain (when the lattice constant is less than that of the substrate layer) are possible.

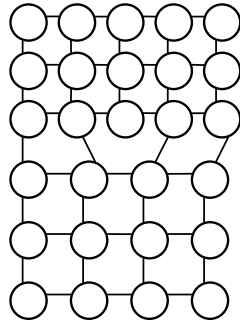


**Figure 1.18:** A sample diagram of a dislocation between two lattice mismatched materials.

### 1.3.16 Lattice Defects

Dislocations, resulting from the lattice mismatch at the semiconductor heterojunction, grain boundaries, resulting from inadequate crystal growth conditions, and impurities, resulting from the introduction of contaminants during the growth process, can cause significant reductions in cell conversion efficiency in photovoltaic cells. Dislocations and grain boundaries both affect the physical properties of a material. There have been numerous studies that have indicated that once dislocation density in a region increases to the order of  $10^5$  per  $\text{cm}^2$ , which can correspond to a lattice mismatch of as little as .5%, cell performance characteristics like minority carrier diffusion length can drastically decrease. The shorter the diffusion length is, the longer it takes an individual carrier to reach the contacts of the cell. The longer a carrier takes to reach the contact of a cell, the higher the chance of recombination becomes. This can lead to decreases in short circuit current, open circuit voltage, fill factor, conversion efficiency, et al.[46-49].

Impurities can negatively affect solar cell performance by adding trap states to the cell's band structure. Depending on the impurity, this trap state can exist in the band gap of the material as a whole, as seen in Figure 1.19. This trap state will facilitate what is known as Shockley-Read-Hall (SRH) recombination, where an electron carrier in the conduction band will relax into the trap state in the band gap, then relax into the valence band. The probability of this entire reaction occurring is greater the probability of recombination for an electron in the conduction band and hole in the valence band. Thus, each trap state in the cell leads to a decrease in the total amount of carriers that are collected at the contacts of the cell. This leads to an overall decrease in the performance of the cell in many of the same metrics as dislocations and grain boundaries [50].

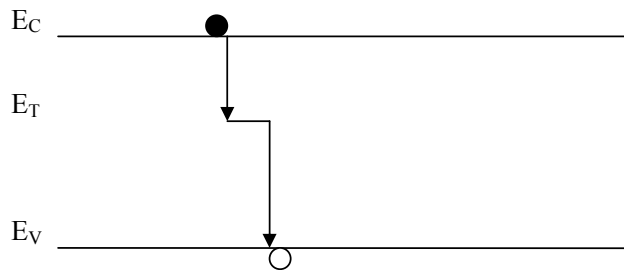


**Figure 1.19:** An electron carrier in the conduction band undergoing Shockley-Read-Hall (SRH) recombination due to the existence of a trap state of energy level,  $E_T$ , existing in the material.

## **1.4 Current State of Photovoltaic Technologies**

### **1.4.1 Single Crystal Silicon**

The first modern semiconductor solar cell was, as mentioned previously, first published in 1954 by Chapin, Fuller, and Pearson of Bell Laboratories. This solar cell was nothing more elaborate than a p-n junction, specifically a thin layer

of p-type material on a n-type substrate, exposed to a stream of photons of a certain energy. These photons were of sufficient energy to generate electron-hole pairs, which led to current in the cell, and from that power. These photocells only were able to produce a conversion efficiency of a scant 6%, a figure that would only group them with today's cheapest and least efficient cells, but at the time was drastic improvement in conversion efficiency for a photovoltaic cell [33].

This cell was the forefather of the entire semiconductor photovoltaic device field, but more specifically was the forefather of the single crystal photovoltaic field. This subset of semiconductor photovoltaics is characterized by having a single kind of substrate through the entire material and utilizing simple doping materials, like simple boron or phosphorus. In general, silicon is the chosen substrate for solar cells, due to its abundance and low cost, but this material choice comes with a number of issues. Firstly, crystalline silicon is an indirect bandgap material, which implies that there is a significant portion of the energy absorbed by the cell that is lost via phonon interactions. This leads to an absorption for crystalline silicon that is not particularly strong, necessitating significant thicker substrates (at least 100  $\mu\text{m}$  for 90% absorption) to ensure all incident sunlight is captured, increasing the costs of a cell [51-53]. Secondly, the large amounts of pure crystal silicon needed for these cells are very difficult to grow. Initially, only Czochralski grown single crystals were of sufficient quality and size for this application and while more methods for crystal growth have since been developed, this problem remains a hindrance to the technology as a whole [9]. Additionally, the band gap of silicon is not of the ideal size for a

single photovoltaic cell exposed to the AM1.5 solar spectrum. As can be seen in Figure 1.20, the Shockley-Queisser limit for silicon, while near the peak of the efficiency curve for photovoltaics using a single material, is not at the highest point of the peak.

Since the introduction of this technology, there have been consistent and gradual improvements in the conversion efficiency of single crystal silicon cells. These cells, while not able to compete in terms of pure conversion efficiency or cost with the best technologies in each of those areas, strike a good balance between cost and efficiency while having great simplicity of design. This simplicity will become apparent as later technologies are examined. To this point, the highest conversion efficiency achieved by a single crystal silicon cell is well over 24%, though in the recent few years progress in pushing this value higher has slowed [35].

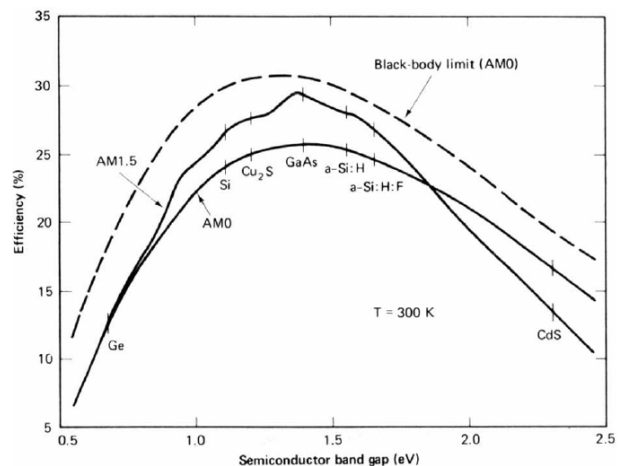


**Figure 1.20:** A comparison of theoretical maximum efficiency (or Shockley-Queisser limit) given a single material of a given band gap. Several well known semiconductor materials are specifically marked on the graph, including both crystalline and amorphous (a-) materials [9].

### 1.4.2 Amorphous Silicon

Amorphous silicon lacks the lattice structure present in crystalline silicon, much like glass lacks the crystalline structure of quartz despite the materials' similar chemical composition. This gives the material certain advantages and disadvantages. Amorphous silicon does not require as costly a manufacturing process to produce, which in turn reduces the total cost of the cell. Process temperatures tend to be significantly lower than in production of crystalline materials, allowing the use of much less expensive substrates, including float-glass or foils made of metal or plastic [54]. Since a lattice structure need not be maintained, films of this material are fairly flexible and have sound mechanical integrity [55]. Additionally, the absorption coefficient of amorphous silicon is significantly higher (upwards of 20x) than that of crystalline silicon, with layers on the order of  $\mu\text{m}$  able to absorb nearly all incident light on its surface [56]. These factors make amorphous silicon a cheap and versatile photovoltaic device.

Carrier generation occurs much like in crystalline silicon, with one noteworthy exception. Despite still being composed mainly of silicon (hydrogen is often present in the material as well, deposited during the production process), the effective band gap of amorphous silicon can range between  $\sim 1.55\text{-}1.8$  eV, compared to 1.1 eV for crystalline silicon. Not only is the band gap significantly higher than crystalline silicon, there is a certain amount of flexibility that can be used to tailor the material to the needed application [56].

These advantages do come at a price to the cells' efficiency and durability. The production process for amorphous silicon generally involves an RF. glow

discharge plasma, utilizing silane ( $\text{SiH}_4$ ) to introduce silicon to the system. Dopants are also typically introduced using highly hydrogenated compounds, including diborane ( $\text{B}_2\text{H}_6$ ) and phosphene ( $\text{PH}_3$ ). The end result is that most amorphous silicon samples include a significant amount of hydrogen from the production process. The hydrogen does nothing to aid the efficiency of solar cells made from amorphous silicon, making its incorporation problematic [56]. Since amorphous silicon lacks the structure of a crystalline lattice, structural irregularities and stray bonds are significantly more frequent in amorphous silicon. This in turn decreases carrier mobility through the material [6]. Also due to the lack of a crystalline structure, stray band tails and defects in the material lead to difficulty when trying to dope the material, making it nearly impossible to dope the material to the point where the Fermi level is within 0.2-0.3 eV of either band edge [54]. The net result of these issues is that amorphous silicon is only capable of lower conversion efficiencies than crystalline silicon, having a record conversion efficiency of 9.47% [57].

Degradation is also a significant issue in amorphous silicon cells. When exposed to sunlight, a phenomenon known as the *Staebler-Wronski* effect occurs in amorphous photovoltaics. Upon exposure to sunlight, even as briefly as a few hours, photoconductivity of the material decreases noticeably, as seen in Figure 1.21. While this effect can be reversed by heating the silicon to around  $150^\circ\text{C}$ , the maintenance required to avoid losses from the *Staebler-Wronski* effect is noteworthy [10].

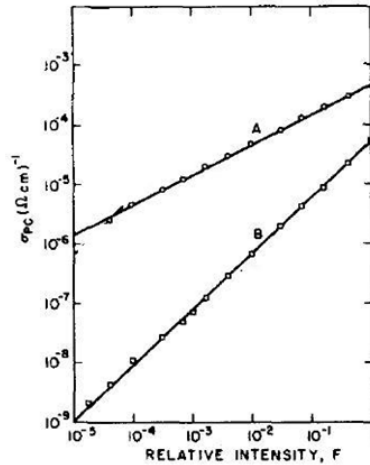


**Figure 1.21:** A comparison of photoconductive at varying intensities of light before (A) and after (B) exposure to approximately four hours of 200 mW/cm<sup>2</sup> of light [10].

### 1.4.3 Dye-Sensitized Solar Cells

Dye-sensitized solar cells (DSCs) work on a slightly different principle than conventional photovoltaics. DSCs are composed of three distinct regions, each serving a different purpose. The central layer to the cell is the dye layer, which is a thin layer that absorbs photons and produces carriers. Whereas conventional photovoltaics rely on the band structure of a crystalline or semi-crystalline element or compound to produce carriers, the dye layer of DSCs utilize complex molecules sensitive to certain regions of the solar spectrum. When these molecules absorb photons, they generate carrier electrons which then diffuse out of the layer. The aim is to have the carriers diffuse into the conduction band of a semiconductor material attached to the dye, commonly TiO<sub>2</sub> or a similar transparent conducting oxide. This layer, as it is the topmost layer of the cell, must also be as optically transparent as possible, implying a large band gap. Once

the carriers diffuse into the semiconductor, they act similarly as in a traditional photovoltaic, moving in a diffusion current until they are collected at the contact of the cell. It should be noted that since the only carriers injected into the semiconductor are electrons, the total current generated compared to a conventional photovoltaic for the same number electrons collected is significantly lower.

The third, bottommost layer of the cell is an electrolyte layer; a liquid, not solid-state, layer whose composition can change from cell to cell. This layer returns electrons to the dye layer, which had diffused into the semiconductor layer, by utilizing a redox (oxidation-reduction) reaction. Electrons which have left the electrolyte layer are then replenished from the rear contact of the cell. A diagram of a typical DSC can be seen in Figure 1.22 [11].

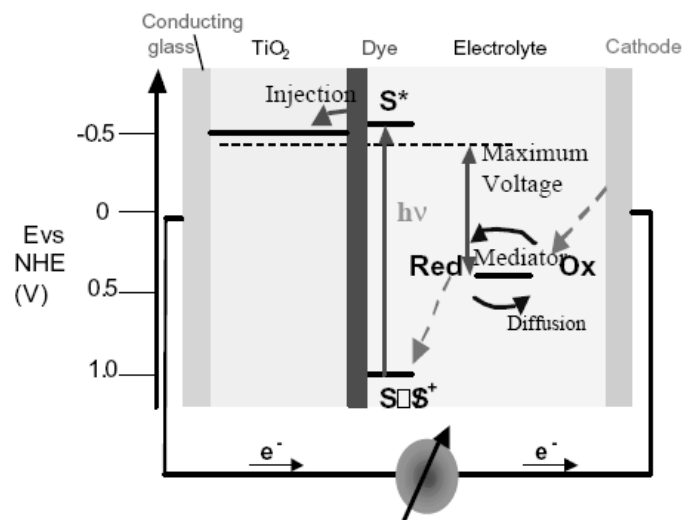


**Figure 1.22:** A diagram of the general layout of a dye-sensitized solar cell (DSC) [11].

One of the earliest effective examples of this type of photovoltaic device was first published in 1991 by Brian O'Regan and Michael Grätzel of the Swiss Federal Institute of Technology. Utilizing a TiO<sub>2</sub> semiconductor layer and iodide/tri-iodide electrolyte, this first cell was able to achieve a conversion efficiency of 7.12% [58]. Since that cell was introduced, steady improvements have been made. Recently, cells with conversion efficiencies over 10% have been recorded, including a cell achieving a 10.8% conversion efficiency designed by Chiba, et al., the highest efficiency at this time. This design, while still utilizing a TiO<sub>2</sub> semiconductor layer, improves upon the amount of light transmitted through the cell compared to earlier designs [59].

Due to their structure and composition, DSCs have a unique set of advantages and disadvantages compared to other solar cells. The main advantage of this cell is its production cost. Since two of the active layers need not be perfectly crystalline, production of those layers tends to be more straightforward and cheaper than higher efficiency photovoltaics. Additionally, new dyes and electrolytes are developed regularly, which may lead to further improvements in conversion efficiency [11], many of which are more environmentally friendly than the materials used in many other photovoltaic cells [60, 61]. Due to the variety of dyes available, DSCs offer an extra design consideration based on the incident spectrum for a given region instead of the traditional AM1.5 spectrum. That spectrum is good average value across all regions, but it may be possible to achieve higher efficiencies for an individual cell by tailoring it to its environment [62]. These advantages come at a cost though, as even the most efficient DSCs

have conversion efficiencies significantly lower than most other solid-state photovoltaics. Since the only carriers utilized in this technology are electrons, it is unlikely that DSCs will ever approach the effectiveness of higher efficiency photovoltaics, with the current maximum recorded conversion efficiency at 10.4% [63]. There are also significant durability issues in regard to DSCs. If the durability of DSCs is significantly less than conventional photovoltaics, then it may cancel out any benefits from it may get from its low manufacturing costs. There are many places where this cell can degrade, the electrolyte and the dye being prime examples. Only recently have DSCs passed the more commonplace of the stability tests applied to solar cells and are still aiming to produce a cell that can meet lifetime benchmark of 20 years of serviceability that is generally accepted as the minimum lifetime acceptable for a solar cell [11]. DSCs also have a higher sensitivity to changes in temperature than most other photovoltaic devices, due to the incorporation of the liquid electrolytes. When exposed to temperatures that are non-ideal, the liquid can lose a significant portion of its efficiency, leading to a decrease in conversion efficiency [64].

#### **1.4.4 Organic Solar Cells**

Organic solar cells differ greatly in composition from inorganic cells, but the physics governing the processes in each are surprisingly similar. Whereas in inorganic cells the active region of the cell is generally a lattice of semiconductor material, organic cells have active regions composed of complex organic molecules in solution. The earliest organic cells, such as that published in 1973

by Ghosh et al., consisted of a single layer of organic material sandwiched between two layers of metal with different work functions. The organic material absorbs the incident photons and generates carriers. Since the diffusion length for electrons is so short in organic films, on the order of only 20 nm [12], these cells exhibited woefully low conversion efficiencies, on the order of .01% or lower [65]. Despite this, it still proved it was possible to convert solar energy to electricity using these materials.

Later organic cells began to utilize a bilayer heterojunction structure, where there would be two distinct layers of organic material, an example of which can be seen in Figure 1.23. One layer would compose of electron accepting material and the other electron donating material, very much akin to p-type and n-type materials. There is an important distinction to make between inorganic cells and organic cells. In inorganic cells, photons stimulate electrons into the conduction band, directly creating electron hole pairs. Once excited, the carriers are able to move through the conduction band to elsewhere in the lattice. In organic cells, carrier generation requires both a donor and an acceptor material. This process starts with a donor molecule absorbing a photon, generating an excited electron. This electron is still bound to the donor material, so another step is required. If the donor material is close enough to an acceptor material, again a very small distance since the mobility of the organic materials is so low, the excited electron can move to and excited state in the acceptor molecule, generating a carrier pair. Since the generation process requires both donor and acceptor molecules, the region they are generated in is limited to the thin region

near the interface of the two layers. Carrier lifetime is significantly improved in this design compared to the single layer design as once carriers enter the donor/acceptor regions recombination is unlikely, dramatically improving efficiency [12, 63].

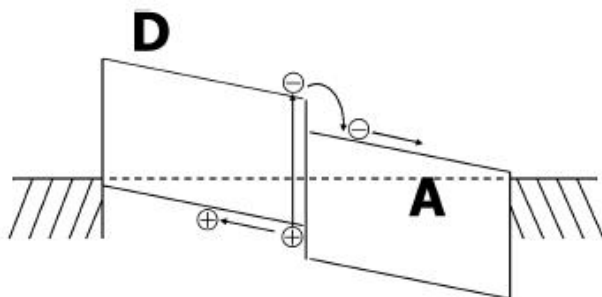


**Figure 1.23:** A band structure for a bilayer heterojunction organic solar cell. It is separated into donor (D) and acceptor (A) regions[12].

One more organic photovoltaic technology under investigation concerns bulk heterojunctions, first developed in 1986 by a group in the Eastman Kodak company [66]. This addresses the issue in bilayer heterojunction cells of the generation region being limited to the interface of the regions by creating as large of an interface between donors and acceptors as possible. This is done by intermixing donor and acceptor molecules through the entire active region. In this way, the generation region is greatly widened, intending to compensate for the increased rate of recombination of the generated carriers. Peak efficiencies for this technology sit in the range of 5.15% [12, 63].

Organic photovoltaics, being fairly similar to dye-sensitized photovoltaics, have similar advantages and disadvantages to that technology. Organic photovoltaics are intended to be cheap and simple to manufacture, flexible in use, and provide serviceable conversion efficiencies [67]. Carrier diffusion lengths for

these materials tend to be small, frequently less than 100 nm [68]. This necessitates these cells being very thin, otherwise carriers will have little chance of being extracted from the device. Like dye-sensitized cells, the conversion efficiency of these cells is significantly less than their more efficient counterparts. At present, organic photovoltaics typically have conversion efficiencies below even those of DSCs, with the highest confirmed readings of only recently rising above 5%. Additionally, organic photovoltaics face degradation issues that could be a serious detriment to the profitability of the technology. Degradation of up to 80% over 6000 hours has been recorded for some of the highest efficiency organic photovoltaics, a rate of degradation which implies a very short lifetime for any device utilizing the technology. The actual length of time 6000 hours of use will last can vary depending on the conditions for an individual region (a winter day in New England receives significantly less sun than a summer day in Arizona), but if an average value of 5 solar hours of use per day is assumed, then these cells are only operating at 20% of their peak efficiency after a little more than three years of use [69].

#### **1.4.5 Up-Conversion**

A typical solar cell can only generate electrical energy from photons with a higher energy than the band gap of the material. This leaves a large portion of incident light unusable by any given cell. Up-conversion is used in addition to a standard cell to utilize some of this unused portion of the solar spectrum. In up-conversion, the energy from multiple low energy photons, typically two both with

energy lower than the bandgap of the material, are used to create a single carrier pair. This is typically done through the use of a material that creates available intermediate states in the region of the bandgap that is normally forbidden to photons.

There are number of different technologies that work on this basic principle, taking advantage of different properties of the materials involved. A comparison of the efficiencies of some of the more prevalent technologies can be found in Figure 1.24 [13]. In energy transfer up-conversion (ETU), there exist energy levels in the forbidden region of the band gap of the material. Once electrons are excited to this intermediate level, there is the possibility that two electrons, both in the intermediate states available, will interact with each other. Should this occur, one of the electrons can absorb energy from the other, using it to rise out of the forbidden band of the semiconductor. In two-step absorption, or ground state absorption (GSA) and excited state absorption (ESA), again an electron is excited to an intermediate level in the forbidden band of the semiconductor. Instead of interacting with another excited electron, the electron instead absorbs a second photon of sufficient energy, raising it into the conduction band of the cell. Cooperative sensitization is fairly similar to ETU, again having two intermediately excited electrons interact to produce a single higher energy carrier. The difference between the two processes is that ETU occurs nearer to resonance, and as such occurs with greater frequency. Cooperative luminescence occurs when two intermediately excited electrons interact, but instead of generating a high energy carrier, they instead emit a single higher energy photon.

This photon can then generate a carrier pair in a more typical fashion. Second harmonic generation (SHG) entails a single electron absorbing two lower energy photons and then emitting a single higher energy photon into the system that then generates carriers. Finally multiple absorption excitation occurs when a single electron absorbs sufficient photons (two or more) in order to obtain sufficient energy to cross the bandgap of the material it's in [70].

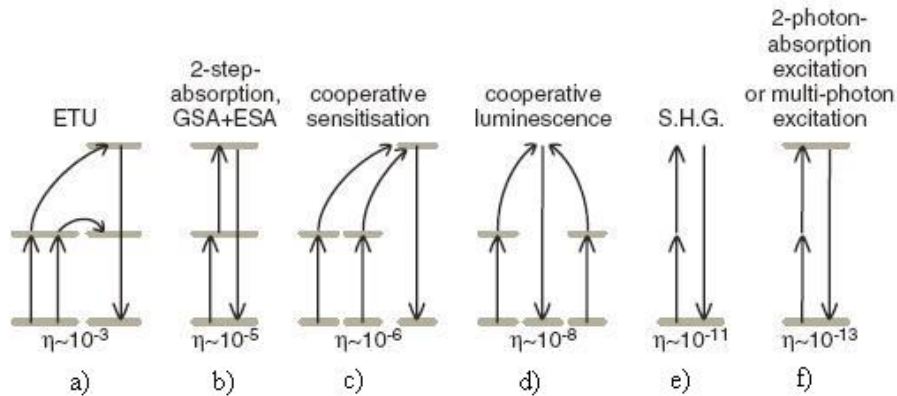


**Figure 1.24:** A comparison of efficiency ( $\eta$ ) for a) energy transfer up-conversion (ETU) b) 2-step ground state absorption (GSE) and excited state absorption (ESA) c) cooperative sensitisation d) cooperative luminescence e) second harmonic generation (SHG) and f) multi-photon excitation [13].

Since up-conversion utilizes low energy photons, which see the materials typically used in solar cells as optically transparent due to their large band gaps, up-conversion systems typically are located at the rear of solar cells as an added layer to solar cells, next to the rear contact. By doing this, the vast majority of the photons that actually reach the up-conversion portion of the device are those whose energies are so low they wouldn't normally be used by the system at all. The up-conversion system doesn't interfere with the normal operation of the cell, only supplements it [13]. The use of up-conversion in photovoltaic systems

improves the theoretical conversion efficiency limit without concentration from 30% (without up-conversion) to 37.4% (with up-conversion). As discussed below, the maximum conversion efficiency is further improved should concentration be used [13].

The main thrust of recent research in this area has been in finding materials that act as efficient up-converting materials. Of particular interest of late are compounds including rare earth ions, such as erbium, holmium, neodymium, praseodymium, and thulium due to the fact that they emit photons in the visible light spectrum when struck by low energy photons [71]. One example of this technology that has drawn recent interest is a system utilizing the up-conversion material  $\text{NaYF}_4:\text{Er}^{3+}$ , a rare earth compound, a concentration array, and silicon-based solar cell. This design is estimated to produce a conversion efficiency of upwards of 25%, most notably improving performance in the absorption of light in the near infrared range [72, 73]. It has also been posited by some research groups that quantum dots may be used as an up-conversion material, capable of creating discrete energy states in the bandgap of a material. This type of cell has shown improvement over a single junction cell, but remains at lower conversion efficiencies than multijunction cells [74].

#### **1.4.6 Down-Conversion**

In photovoltaics, when an incident photon has more energy than the band gap of the semiconductor, the semiconductor is still able to absorb the incident photon. When this occurs, the excited carrier then relaxes to the lower edge of the

conduction band. This relaxation occurs as both lattice heating or, of more interest for down-conversion, photon reemission and represents a significant source of wasted energy from incident photons.

Down-conversion is very much the counterpart to up-conversion. Where in up-conversion the energy from multiple low energy photons is used to create a single carrier pair, in down-conversion a single high energy photon is used to generate multiple, usually two, carrier pairs. The high energy photons used by the down-converter must be at least twice the energy as the band gap of the semiconductor, or the excess energy from creating a carrier pair will not be sufficient to generate another carrier pair. One method to do this is to utilize a material that has a bandgap significantly larger than that of the solar cell, at least twice as large, then introduce a small amount of impurities to the down-conversion layer, creating one or more intermediate states in the forbidden region of the down-converter's band gap. Ideally, the photons absorbed by the down-converter would have an integral multiple of the band gap energy of the semiconductor and the impurity layers would be located such that they divided the converter band gap into regions exactly the size of the solar cell band gaps, avoiding wasting any energy from the incident photon, but this is not always possible [14]. A sample diagram of a down-converter is supplied in Figure 1.25. When the incident high-energy photon has significantly more energy than the bandgap of the material ( $>3E_g$ ), then multiple exciton generation (MEG) is possible. In this case, instead of two carrier pairs being generated, many pairs are

generated, the total depending on how much energy the incident particle has. To this point, MEG remains in its conceptual stage [75].

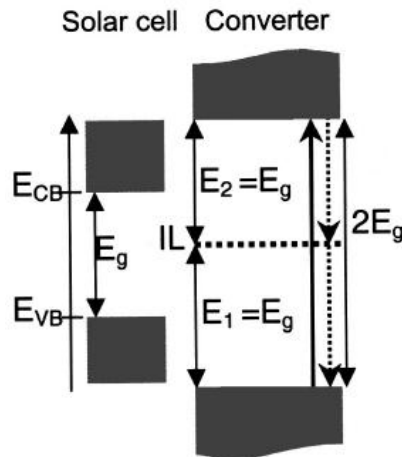


**Figure 1.25:** A band diagram of an ideal down-converter system. The down-converter has a bandgap twice that of the solar cell with an impurity layer (IL) of available states in the middle [14].

There are two main designs for utilization of down-converters. The first utilizes a front-mounted design. As the down-converter utilizes photons of higher energy than the rest of the solar cell, there is the possibility that the high energy photons may be absorbed by the solar cell, leading to wasted energy. By placing the down-converter on the front of the cell, the intention is to avoid this waste. The other option entails a rear-mounted design. This design, while having the potential to be very efficient, has a number of problems. For this design to work, the portions of the cell in front of the converter must be optically transparent to the high energy photons. This is not possible for any semiconductor photovoltaic, and in fact is possible in only some dye-sensitized cells. Additionally, this design, in order to achieve maximum efficiency, requires a bifacial design, which makes design and fabrication of the cell much more complicated [14].

When a down-converter is used properly, it can lead to a significant improvement in overall cell efficiency. For a rear-mounted down-converter system, a maximum theoretical efficiency of 39.63% without concentration has been calculated. Since this system cannot use semiconductor devices, since they are not optically transparent to high energy photons, achieving anything near this benchmark will be difficult. For a front-mounted down-converter system, a maximum theoretical efficiency of 38.6% without concentration has been calculated. Both designs offer an improvement in maximum theoretical efficiency without concentration, just over 30%, as can be seen in Figure 1.26 [14]. The reason this improvement is not more significant is due to the limited number of incident photons with more than twice the energy of a bandgap for a given semiconductor. This significantly hampers the usefulness of this technique [76].

Similarly to upconversion, one of the main difficulties with putting this concept into practice is finding materials that are practical to use in conjunction with current solar cell technology. Some groups are looking at materials including Yb<sup>3+</sup> and Tm<sup>3+</sup> ions, only instead of implanted in semiconductors like in up-conversion these ions are implanted into glass or glass-type materials [77].

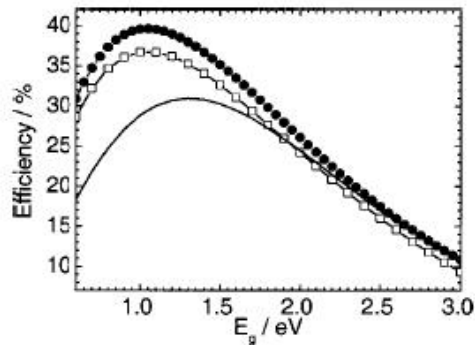


**Figure 1.26:** A comparison of the efficiencies of a photovoltaic system for the Shockley-Queisser limit of a single junction cell (solid line), with a down-converter on the front surface (open squares), and with a down-converter on the rear surface using a reflective coating (solid circles) [14].

### 1.4.7 Nanoparticles and Quantum Structures

Another method developed for improving overall conversion efficiency of a photovoltaic cell involves using structures whose size are on the scale of the wavelength of incident photons but larger than the individual atoms of a semiconductor lattice. These structures, called nanostructures, come in many different forms and work on a handful of different principles. The most prevalent methods either involve a process similar to up-conversion, enabling a cell to utilize photons it wouldn't normally be able to use, or a method of improving the mobility of carriers through the cell, reducing recombination in the cell and improving the final output. Additionally, these nanostructures can be defined not only by the methods they use, but also the dimensionality of the structure, how many dimensions the nanostructure's size approaches zero. This can range from three dimensional structures, which have no dimensions on which approach zero, to quasi-zero dimensional structures, where the structure is approaches zero size in all spatial dimensions.

Three dimensional nanostructures typically work by either improving the carrier mobility of a material or increasing the probability a photon is absorbed by the material. This is done by suspending the nanoparticles in a layer of the device. For nanoparticles that aim to improve the mobility of a material, these nanostructures don't necessarily interact direct with photons, but instead interact with carriers generated elsewhere in the cell. When a carrier is absorbed into an energy state of a nanoparticle, it is capable moving across the length of the nanoparticle with relative ease. Since the nanoparticles are generally much larger than the atoms of the substrate material, this means the carrier has to change energy states fewer times moving through the substrate. Also because of the size of the particle, it is very difficult to introduce these materials to a semiconductor lattice. Generally, these nanostructures are confined to organic and dye-sensitized photovoltaic applications. Since each change in energy state represents a possibility of recombination, reducing the number state changes improves the chances the carrier will avoid recombination. Also, since these structures are three-dimensional, orientation is not significant concern, a problem with other nanostructures. There are few nanostructures that are both three dimensional and capable of conducting carriers efficiently. This limits fabrication options and generally involves some fairly complicated compounds [15].

One such three dimensional nanostructure involves a branched CdSe/polymer molecule in the shape of a 'tetrapod', reminiscent of a child's jack. A transmission electron microscopy image of a tetrapod is supplied in Figure 1.27. These nanoparticles were then suspended in solution and exposed to solar

radiation without the benefit of a typical semiconductor device. Despite this, the solution was still able to produce a conversion efficiency of 1.8%. This number is promising, though problems still remain on how to implement these devices in crystalline cells without introducing excessive strain to the lattice [15].

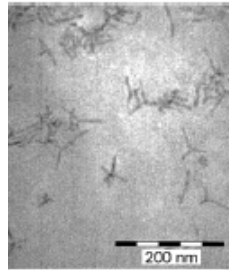


**Figure 1.27:** Transmission electron microscopy (TEM) images of a ‘tetrapod’ three dimensional nanostructure [15].

Two-dimensional nanostructures tend to work using a very different process than three dimensional nanostructures. Two-dimensional structures usually utilize layers of different materials. The number of layers used can vary between a single layer of one material sandwiched between two layers of another to a superlattice, a lattice of lattices, of two materials, as can be seen in Figure 1.28. These materials have separate band gaps and lattice parameters. These differences lead to a significantly altered band structure for the material as a whole. The varying band gaps lead to an alternating sequence of peaks and valleys in the band structure of the material, as can be seen in Figure 1.29. In the valleys, known as quantum wells, exist a number of energy states at a lower energy than that of the original conduction band. This allows for the utilization of lower energy photons in a manner very similar to up-conversion described above.

Simply, carriers can be excited by a low energy photon into the quantum well, then excited a second time into the conduction band of the material [17, 78].

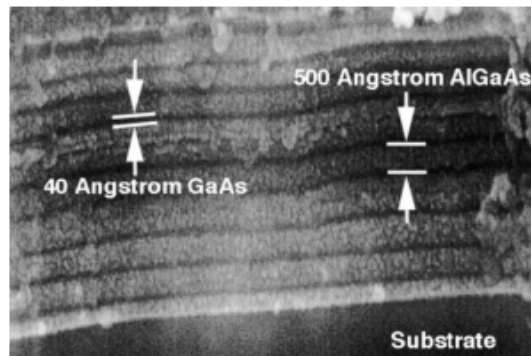


**Figure 1.28:** A SEM image of a superlattice of GaAs and AlGaAs [16].

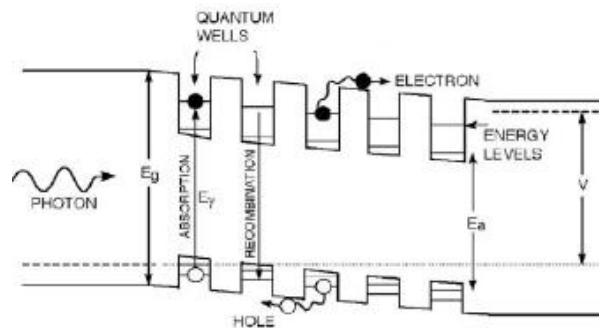


**Figure 1.29:** A sample band structure for a photovoltaic device utilizing quantum wells [17].

There are some additional effects that must be taken into account with this band structure, however. Whereas in up-conversion, there were a relatively small amount of available intermediate states available, in quantum wells there is a comparatively larger amount of available states at varying energies. This means that there are more energy states in which intraband reactions can occur. Naturally, interband recombination still occurs, only now recombination in both the well layer and the conduction band layer must be considered. One such

process, impact ionization, occurs when a single photon generates multiple carrier pairs, generally each pair at the lower edge of the conduction band of the well material. These carriers can then be excited into the conduction separately. Of more concern, however, are the relaxation processes that can occur. Auger relaxation processes can occur, where excited carriers relax partially but remain in the same band. This can occur not only between the various energy states in the well, but also between states of the conduction band and the well. These processes represent additional lost energy in the photovoltaic system. In order for a quantum well system to improve overall efficiency of the cell, the gain in energy production from impact ionization and up-conversion must outweigh the additional losses from recombination and Auger relaxation [79, 80].

Additionally, in the case of superlattices, where the separation of the well layers becomes smaller, quantum effects can be seen. Normally, when a carrier molecule is in a well energy level, it will tunnel a certain distance into the forbidden region between wells. If the distance between the wells is less than that penetration depth, then the carriers will be able to penetrate through the forbidden region between the wells into the adjacent wells. This leads to continuous minibands of available states across the superlattice as opposed to localized energy states, as can be seen in Figure 1.30. With careful spacing of the layers its possible to adjust the spacing the energy gap between the minibands of the wells [4]. The spacing of these minibands is generally too small to be of use in typical photovoltaic setups, but can be useful in thermophotovoltaic devices.



**Figure 1.30:** A sample band diagram illustrating the formation of minibands in a superlattice of quantum wells [4]

There are some additional concerns which must be addressed in this type of device. Since the device is composed of alternating layers of material, lattice strain must be considered between materials. Should the lattice constants be too far apart, the strain between the layers can lead to dislocations and defects in the cell. These can act as sites for carrier recombination, which would make the cell unusable. In fact, there are a number of criteria which should be adhered to in quantum well cells, including limiting lattice mismatch between any interface to within 2% in either direction and making the depth of the well as close to 0.9 eV as possible [81]. In cases where lattice constants significantly vary, a technique known as strain balancing is utilized. This technique involves using materials that put opposing strains on a material (i.e. places a compressive strain one side of the material and a tensile strain on the other). This can lead to combinations of materials that might otherwise be infeasible due to lattice mismatch [82]. There have been numerous theoretical investigations into the efficiency of these systems using a number of different materials. For example, one such design utilizing GaInP and GaAs has achieved a conversion efficiency of over 30%, a very promising number [83].

One-dimensional nanostructures tend to be more similar to three-dimensional nanostructures than two-dimensional nanostructures, and as such tend to be used more in organic and dye-sensitized, rather than semiconductor, solar cells. One dimensional nanostructures, also called nanotubes, nanowires, nanorods, et al., used to conduct carriers through a substrate after generation. Due to their comparative size to the rest of the atoms in the lattice they are in, the nanostructures are able to reduce the amount of energy state changes a carrier must go through in order to reach the contacts of the cell, reducing the chances of recombination. A sample TEM image of a one dimensional structure is provided in Figure 1.31. However, since these devices are only one dimensional, directionality is very important. When the nanoparticles are oriented perpendicularly to the contacts, they are an effective way to reduce the mobility of the surface. When the nanoparticles are oriented towards the sides of the cell, lying flat, they have little effect on the cell other than taking up space [15].

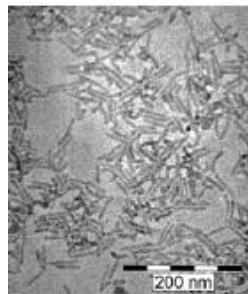


**Figure 1.31:** A TEM image of nanorods [15]

The methods and materials used in creating and orienting these structures vary significantly. For example, one popular material used is ZnO due to its high carrier mobilities and long carrier lifetimes [84]. Methods for orienting nanostructures include techniques such as vapor-solid (VS) and solution growth

(SG), but one of particular recent interest involves vapor-liquid-solid (VLS) growth. In this process, first seed molecules of the nanowire material are implanted in the substrate. A liquid solution containing a larger amount of that material is then introduced. As the nanowire material is chosen such that the sticking coefficient is much larger between itself than with the substrate, nanowires begin to assemble on the locations of the seed molecules [85]. These nanostructures tend to produce fairly low conversion efficiencies, with conversion efficiencies under 2% fairly common [86, 87].

Decreasing even further in size are quasi-zero dimensional structures, commonly referred to as quantum dots. A quantum dot is a highly localized region (smaller than the deBroglie wavelength of a charge carrier) of a given semiconductor material deposited on a semiconductor of differing material. An example is supplied in Figure 1.32. In practice, quantum dots have a number of similarities to quantum wells, but have additional considerations from quantum wells that must be addressed. As was the case with quantum wells, quantum dots create a number of energy states between the conduction and valence bands of the substrate material. These states can exhibit many of the same effects that quantum wells have in terms of intraband excitation and relaxation [79, 88] Since quantum dots are significantly smaller than the wells in size, there are significantly fewer available intermediate states available than in quantum wells and as such it is rare for a quantum dot to contain more than one carrier at any given time. This leads to number of phenomena that are not present in quantum well cells.

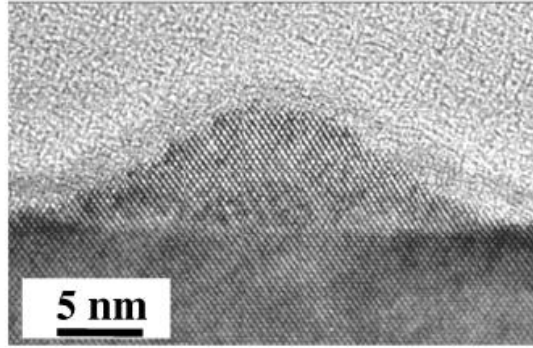


**Figure 1.32:** A TEM image of an InAs/GaAs quantum dot [18].

A large quantity of quantum dots is typically deposited on a substrate at once, usually in a fairly high number-density (e.g.  $10^{10}\text{cm}^{-2}$ ). A typical density for deposition of quantum dots can be seen in Figure 1.33. The density of the quantum dots on the substrate leads to the spacing between the individual dots being fairly small, which in turn leads to the appearance of quantum effects. For example, tunneling between quantum dots, much like tunneling between quantum wells mentioned previously, is a distinct possibility [19]. Perhaps the most interesting characteristic of quantum dots is that the effective bandgap of the dot material can change vary with the size of the dot. For example, when InAs, normal band gap of 0.38 eV, is used as a material for quantum dots, its band gap changes from 1.071 eV for dots with a diameter of 5 nm to 0.553 eV for dots with a diameter of 12 nm [89]. This allows for a material to be tuned to a desired bandgap within a given range, letting it absorb that wavelength of light most efficiently.

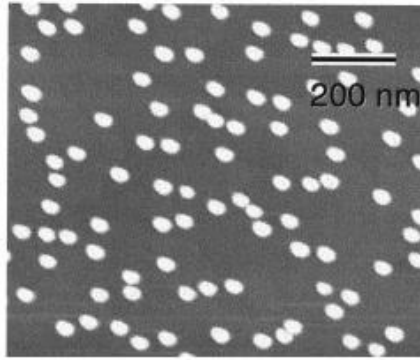


**Figure 1.33:** A  $1\ \mu\text{m} \times 1\ \mu\text{m}$  atomic force microscope (ATM) image of InAs quantum dots on a GaAs substrate [19].

There are a number of concerns which must be addressed in quantum dots. As mentioned before, the small physical size of the quantum dot greatly limits the number of available conduction states present. This can lead to an effect called the Coulomb blockade, where a carrier present in a conduction state of the dot prevents any other carriers from filling the rest of the dot's conduction states in all but the highest densities of carriers. This limiting factor can reduce the total efficiency of a cell using quantum dots [90]. There is also considerable strain present at the interface of any quantum dot and the surrounding material. This not only can give rise to various strain issues at the interface, but also can influence and alter the energy states present in the quantum dot [91].

#### **1.4.8 Multijunction Photovoltaics and Concentrating Arrays**

In the years following the invention of the earliest single crystal solar cells, discussions about how to improve overall conversion efficiency began. One method of great interest was that of multijunction photovoltaics. The concept for

the technology was fairly straightforward: if a single semiconductor crystal with a fixed band gap can convert a certain amount of solar energy into usable energy, perhaps a series of semiconductors, each with a different band gap, could convert a higher percentage of incident solar energy into usable energy. One of the earliest published theoretical investigations into the idea of multijunction photovoltaics, performed by W.P. Rahilly in 1972, suggested that this could be a highly fruitful area of research [92]. Soon after, initial designs implementing this idea were created with encouraging results. One of the earliest multijunction cells implemented was that by B.L. Sater et al., published in 1973. The cells not only demonstrated promising conversion efficiencies, but also maintained their performance when exposed to higher concentrations of light than typical at the Earth's surface [93]. From this point on, multijunction photovoltaics and solar concentration have been closely tied technologies.

From those beginnings, multijunction solar cells, typically used in conjunction with concentration arrays have become the technology capable of achieving the highest conversion efficiencies. Among the highest efficiency cells recorded to date is a triple junction cell composed of  $\text{Ga}_{0.35}\text{In}_{0.65}\text{P}/\text{Ga}_{0.83}\text{In}_{0.17}\text{As}/\text{Ge}$ . This cell achieved a conversion efficiency of 41.1% under a concentration of 454 suns. This is not only a tremendous result because of the efficiency that it achieved, but also for what it portends. This cell was not under high concentration and utilized three junctions. A design utilizing more junctions under higher concentrations could easily produce even higher efficiencies [94].

The basic design of a multijunction photovoltaic cell remains the same regardless of the materials used or the number of junction employed. In a multijunction cell, a series of semiconductor materials are stacked upon each other in order of decreasing band gap, with the largest band gap struck by incident sunlight first. The material absorbs photons above an energy larger than the band gap of the material, but remains optically transparent to photons with an energy below that level. The remaining photons then strike the next layer of the cell, with that layer absorbing remaining photons above the band gap of the material. The process is then repeated through all the subsequent layers of the cell. Since each photon is absorbed by a layer with a band gap only slightly less than the energy of the photon, there is very little wasted energy due to relaxation in the conduction band of the materials [21].

While multijunction photovoltaics hold great promise in terms of conversion efficiency, the complexity of the design comes with a number of design considerations which must be accounted for. Firstly, concentration over the cell must be as uniform as possible. Should concentration be nonuniform, a voltage difference can arise parallel to the plane of the semiconductor layers, as can be seen in Figure 1.34. This voltage is capable of reducing the efficiency of the system as a whole [20].

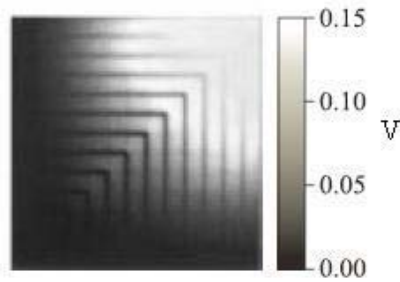


**Figure 1.34:** Example a solar cell under nonuniform concentration ( $\sim 1000$  suns). A voltage difference of upwards of .15 V has arisen parallel to the plane of the solar cell [20].

An additional consideration that must be made in the case of concentrating solar cell array is that of heat management. In cases of high concentration, the heat load on a solar cell understandably increases. Due to the material properties of the cell, this increase in heat load can result in lower operating efficiencies, long term degradation of the cell, and even outright cell failure. Cooling for cells under high concentration comes in two varieties. Passive cooling, once installed, requires no external energy source. Such cooling measures include methods like forced air convection, use of heat sinks, and numerous others. Active cooling, which does require an external energy source, includes methods including heat pumps and pumped coolant systems [95].

More problematic are the other considerations. Since there are number of different layers, each composed of a separate semiconductor material, each must be lattice matched the other layers it contacts. Without lattice matching the materials, defects in the cell can become prevalent enough the cell is unusable. This constraint would not be troublesome without the other constraint which must be considered. In order for the cell to operate most efficiently, the band gaps

must be optimally spaced apart from each other. By doing this, the least amount of incident solar energy is wasted. In Fig. BA2, the optimal band gaps for each layer of n-junction cells are shown for different conditions. In short, in order to have optimal performance, the band gaps of the materials must have particular values, depending on the number of junctions used, which all are lattice matched. As the number of junctions increases, the number combinations of materials (III-V, II-VI, ternary, and quaternary) that satisfy both of these considerations plummets [21].

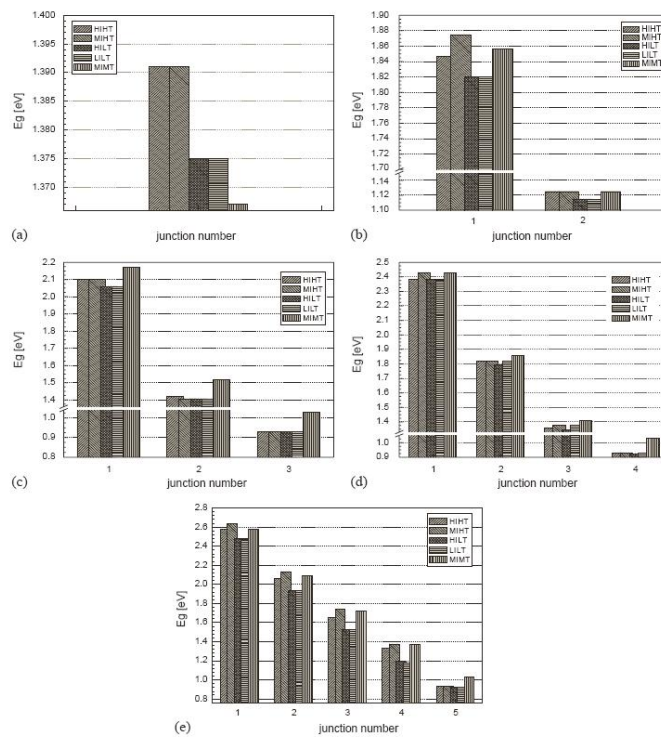


**Figure 1.35:** The optimum band gap under conditions of high irradiance-high temperature (HIHT), medium irradiance-high temperature (MIHT), high irradiance-low temperature (HILT), low irradiance-low temperature (LILT), and medium irradiance-medium temperature (MIMT) for each layer of a) 1-junction cell b) 2-junction cell c) 3-junction cell d) 4-junction cell and e) 5-junction cell [21].

Closely related to bandgap spacing is the issue current mismatch. The bandgap spacing specified in Figure 1.35 are determined such that each junction of the cell would generate the same amount of current, assuming all junctions had the same absorption efficiencies. The reason for this consideration becomes evident if the junctions of the cell are modeled as a circuit. The individual junctions of the cell can be considered as series connected current sources. As is the case with series connected current sources, the maximum current that can flow through the circuit will be limited by the junction with the smallest current, i.e. the total current through a solar cell will be equal to the smallest current produced by an individual junction in that cell. If the current matched condition is not met, it is clear a significant drop in cell conversion efficiency is possible. If optimal band gap spacing cannot be achieved, there is some recourse to minimize the effects of current mismatch. For example, by keeping each junction as thin as possible without affect its absorbance efficiency, the resistance of a constricting junction can be lowered. This helps minimize the loss in current due to electrical resistance [21, 96].

The main advantage multijunction photovoltaics have is that they are capable of the producing the highest conversion efficiencies at present, with or without concentration [35]. Thus, the technology has become of great interest in applications where conversion efficiency is prized above all else. The most noteworthy of this kind of application is for use in space applications, such as supplying energy to satellites, probes, etc., where every extra percent of conversion efficiency can allow the equipment to perform more functions and

have a longer lifetime and every ounce of weight saved makes it less expensive to get into space [97].

While multijunction photovoltaics are on the whole more efficient than other technologies, the cost of the materials used in the cell and the fabrication process used in production does make these cells more expensive to produce. It is very possible that, for cells of the same size, a low efficiency, organic cell may be more cost effective than a high efficiency, multijunction cell. Because of the technology's high conversion efficiency and its effectiveness when used in conjunction with solar concentration, a multijunction cell can have a much smaller physical size and still remain highly effective. This keeps the costs down for production of the cell to the point where they can be competitive with other photovoltaic technologies. As can be seen in Figure 1.36, the cost for producing a multijunction cell utilizing concentration is rapidly approaching the level that would be attractive for wider production [22].

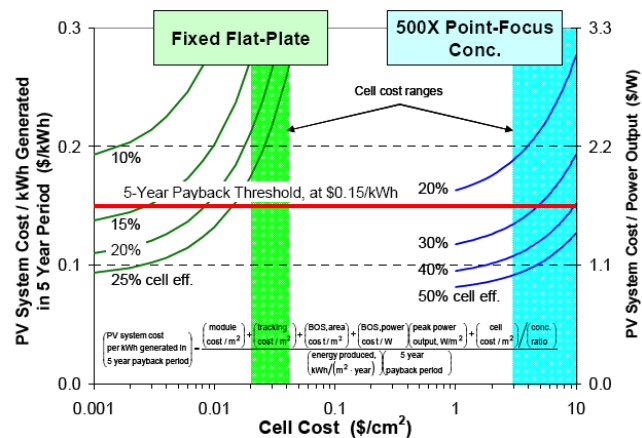


**Figure 1.36:** Plots of PV system cost per kWh electricity generated in a 5-year period, as a function of cell cost per unit area, for both flat-plate (non-concentrated) and concentrator PV systems. Current multijunction photovoltaics have achieved conversion efficiencies of over 40% under concentration [22].

### **1.4.9 Split Junction Photovoltaics**

An interesting extension of multijunction photovoltaics has received some attention recently. Split junction photovoltaics attempt to address some of the issues present in multijunction photovoltaics, namely the requirement that all junctions in the device must be lattice-matched. There are two main components to a split junction photovoltaic system. First, a group of solar cells, typically two, are used. Each cell can theoretically consist of multiple junctions, though as yet individual cells in a system rarely contain more than two. Each junction in a cell must be lattice matched to all other junctions in that cell, but each cell utilized may have a different lattice constant. This leads to a significant increase in possible material combinations for junction layers compared to multijunction systems. Second, the system requires a device to split the incident solar spectrum, with a different portion redirected to each cell. This device must split the spectrum in a particular way in order to be useful. Ideally, the device would divide the incident spectrum on the basis of wavelength. For example, if a system utilized a pair of solar cells, then the splitter would aim to direct all solar energy above a certain wavelength on one cell and all solar energy below that same energy onto the other. An example of transmission and reflection spectra of one such device, a dichroic filter, is provided in Figure 1.37.

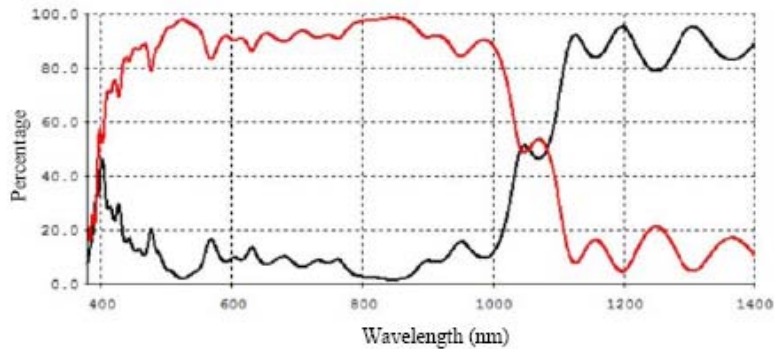


**Figure 1.37:** Sample reflectivity (red) and transmission (black) spectra for a dichroic filter [23].

Choosing the band gap placement for the individual junctions in a cell is a similar process to that of multijunction cells. The main difference between the two is that the incident spectrum is different, usually truncated, due to the splitting device. Within a single cell, lattice constants and photocurrents must match, as is true with any other multijunction device.

Choosing a method to actually split the spectrum and redirect sunlight adds an additional level of design to these devices. There are a number of methods that can achieve the desired spectral response. One method, mentioned above, utilize dichroic filters. A dichroic filter aims to transmit all light with a longer wavelength than the designated frequency and reflect all light with a shorter wavelength. Another method involves utilizing a dispersive grating. This grating disperses different frequencies of light at different angles, creating a beam of light much akin to a rainbow. Different portions of this beam can then be redirected onto individual cells [98-103].

### 1.4.10 Tunnel Diodes

Tunnel diodes, also known as Esaki diodes, while not a photovoltaic technology in themselves are absolutely crucial to the performance of multijunction cells. In an ideal multijunction cell, the band edges of the conduction and valence bands would only rise or lower moving through the cell. Due to the physical properties of materials commonly used for solar cells, such as electron affinities, band gaps, etc., this very rarely happens in practical solar cells. Generally, moving from the n-region of one junction to the p-region of the subsequent junction will result in a potential barrier for both carrier types, as seen in Figure 1.38. This potential barrier would stop current from flowing between these layers, turning the cell into nothing more than useless layers of semiconductor. In order to utilize the advantages of multijunction cells, this problem has to be overcome, and to do this tunnel diodes are used.

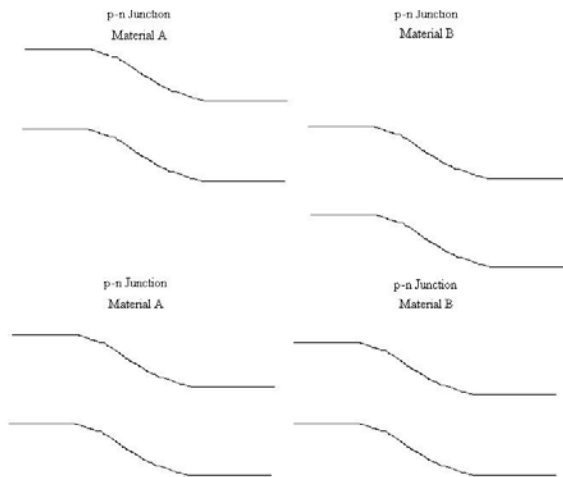


**Figure 1.38:** Band structures like the one in a) would be ideal for multijunction cells. Moving from left-to-right, both the conduction and valence band edges are always lowering in energy. Much more common are band structures as seen in b), where moving from the n-doped region of the left junction and the p-doped region of the right junction introduces a potential barrier in both bands.

First published about in 1958, a tunnel diode has a similar structure to that of typical diode. Like in a traditional diode, a p-doped region is placed in contact with an n-doped region. Unlike a traditional diode, the doping levels are significantly higher in tunnel diode, typically on order of  $10^{19} \text{ cm}^{-3}$  while simultaneously employing very thin material layers, typically on the order of tens of nanometers, both parameters required for making a successful tunnel diode. For small forward biases, in the range tenths of volts, the tunnel diode conducts better in the reverse direction rather than the forward direction, leading to the atypical voltage current curve seen in Figure 1.39 [104].

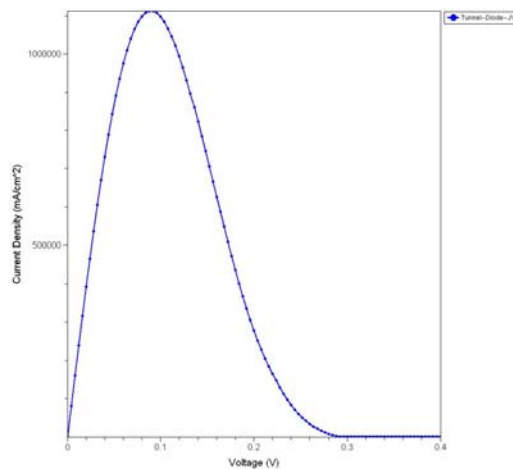


**Figure 1.39:** An example of an I-V curve for a tunnel diode.

The mechanisms at work in a tunnel diode are quantum mechanical in nature. When the proper voltage bias is applied to the tunnel diode, electrons in the valence band of the n-doped region tunnel through the forbidden region into states occupied by holes in the p-doped region. This tunneling only occurs if the energy states are at nearly the same energy level, a sample band structure for which is provided in Figure 1.40. If too little bias is applied, many of the energy

states containing electrons in conduction band of the n-doped region, due to the high doping levels, will be at the same energy level as electrons in the p-doped valence band. Should tunneling occur, electrons moving from n-doped to p-doped region will find the majority of energy states already occupied by electrons, preventing current flow. If too large a bias applied, then electrons in the n-doped region will be at the same energy level as the forbidden region in the p-doped region. Naturally, the electrons will be unable to flow into the p-doped region in this case [24, 105, 106].

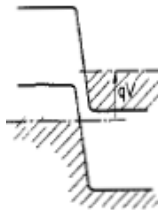


**Figure 1.40:** Band structure of energy states in a tunnel diode where tunnel can occur. Grey areas are filled with electrons, white areas with holes [24].

Additional design criteria must be considered in the case of solar cells. In order to prevent the tunnel diode from absorbing any usable sunlight, the materials used in the tunnel diode should all have at least as large a band gap as the small junction above it. Additionally, at the heterointerface between a layer of the tunnel diode and one of the active p-n junctions in the solar cell, it is imperative to have a continuous band edge. If there is a discontinuity in the band edge, carriers can encounter a potential barrier before reaching the tunnel diode, greatly decreasing current flow through the cell. In order to prevent band discontinuities, there are a pair of criteria that conservatively predict whether any discontinuities will occur. On the n-doped side, Equation 1.25 must be satisfied:

$$\chi_n < \chi_{n+} \quad 1.25$$

where  $\chi_n$  is the electron affinity of the n-doped side of the active p-n junction and  $\chi_{n+}$  is the electron affinity of the tunnel diode. On the p-doped side, Equation 1.26 must be satisfied:

$$\chi_p + E_{g,p} > \chi_{p+} + E_{g,p+} \quad 1.26$$

A band structure of a tunnel diode implemented in a solar cell is provided in Figure 1.41 and Figure 1.42.

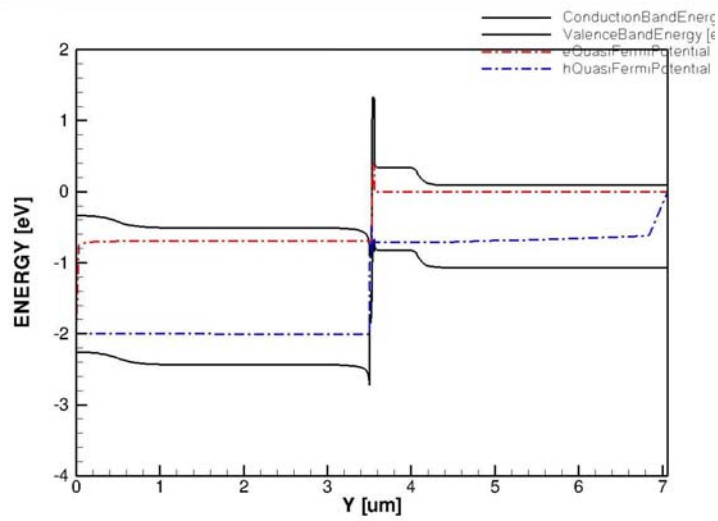


**Figure 1.41:** The band structure of a tunnel diode (center) between GaInP (left) and GaInAs p-n junctions.

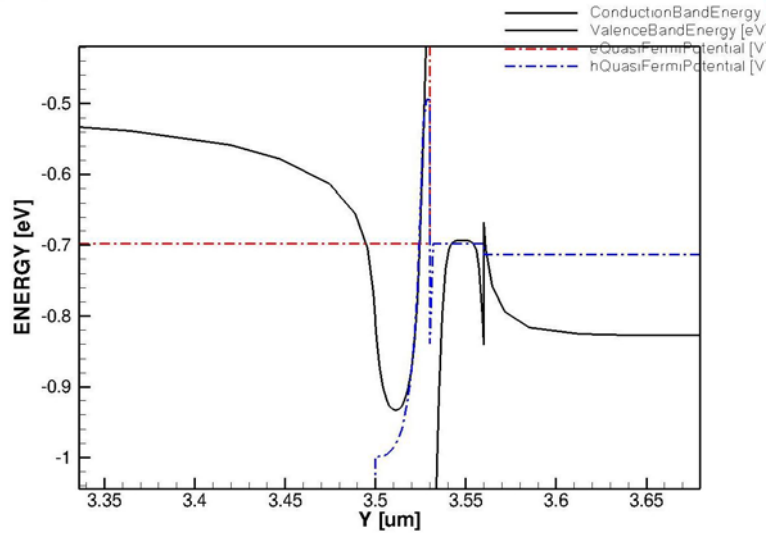


**Figure 1.42:** A close-up of the band structure of the tunnel diode in Figure 1.41. The n-side (left) follows the proper design criteria, leading to a continuous band edge. The p-side does not, and thus has a band discontinuity.

#### 1.4.11 Antireflective Coatings

An issue with all photovoltaic devices is reflection of light off the front of the cell. Some of this reflection is unavoidable, such as when light strikes the front-side contact of a cell, but ideally any light that strikes the cell material would be absorbed by the cell and converted to usable energy. The amount of reflection that does occur under normal incidence at a material interface is governed by Equation 1.27.

$$R = \left( \frac{n_1 - n_2}{n_1 + n_2} \right)^2 \quad 1.27$$

In this equation,  $R$  is the reflection coefficient, or the percentage of power of incident light which is reflected and  $n_1$  and  $n_2$  are the indices of refraction for the materials at the interface [4]. Unfortunately, for most solar cell materials ideal absorption does not occur, due to the large difference in index of refraction

between air ( $n \approx 1$ ) and the cell material (for semiconductor materials,  $n \approx 3.5-4$ ). For semiconductor cells, even when using optimistic assumptions for index of refraction for the interface material, taking  $n=3.5$ , reflection off the front of the cell can be over 30%.

In order to reduce the reflection off the front of the cell, antireflective coatings (ARCs) are utilized. This thin coating is deposited on top of the cell and consists of either a single material layer or multiple layers. There are number of different topologies of ARCs, such as index of refraction matching, single or multilayer interference, and use of nanostructures, but for the purposes of this thesis only the simplest method, index of refraction matching will be examined. Interference related ARCs, due to their nature, are used for either single wavelength or very narrow bands of wavelength applications. Since light incident on solar cells encompass a wide range of wavelengths, these topologies are not applicable. Nanostructures are generally used to improve incident light absorption as opposed to promoting transmission. Since there is no benefit to having the ARC of a solar cell absorb incident light, this topology isn't examined.

There are two main considerations for a material's use in an index-matching ARC: its index of refraction and band gap. The index of refraction should be chosen to minimize the sum total reflection from both the air/ARC interface and the ARC/semiconductor interface, which can be calculated utilizing Equation 1.27. Similarly, when an ARC is composed of multiple layers, the indices of individual layers should minimize the reflection from total of all the interfaces. The band gap for any layer in the ARC should significantly larger than

ideally band gap used in a junction of the solar cell. Ideally, the band gap would be larger than any energy photon incident on the cell, thus rendering the ARC optically transparent to all the wavelengths of light in the solar cell. When following these guidelines, the ARC can dramatically reduce the total reflection from off a solar cell. Using the previous example of cell with a top junction index of refraction of 3.5, adding a single layer ARC with an ideal index of refraction of 1.87 reduces the total reflected power from 30.9% to 18.4%. Adding a second layer to the ARC can reduce total reflected power to 12.7% [4].

## **1.5 Performance Parameters and Rubrics**

### **1.5.1 Built-in Voltage, Open Circuit Voltage, and Bias Voltage**

When discussing photovoltaics, particularly semiconductor photovoltaics, there are a number of voltages involved with similar definitions. The built-in voltage,  $V_{bi}$ , as described above, characterizes the voltage difference between the conduction and valence band levels in a p-n heterojunction. This voltage plays an important role in determining the efficiency of a semiconductor photovoltaic cell, and is characterized by Equation 1.28:

$$V_{bi} = \frac{kT}{q} \ln \left( \frac{N_A N_D}{n_i^2} \right) \quad 1.28$$

where  $k$  is Boltzmann's constant,  $T$  is the lattice temperature,  $q$  is the magnitude of electric charge,  $N_A$  and  $N_D$  are the doping densities of acceptors and donors, respectively, and  $n_i$  is the intrinsic carrier concentration. The intrinsic carrier concentration is the density of carriers present in a semiconductor that are thermally excited, and characterized by Equation 1.29:

$$n_i = \sqrt{N_C N_V} e^{-E_g/2kT} \quad 1.29$$

where  $E_g$  is the material band gap and  $N_C$  and  $N_V$  are the available density of states in the conduction and valence bands, respectively. Thus, the built-in voltage rises when the band gap increases or material doping levels increase [7].

The open circuit voltage of a photovoltaic cell is the voltage generated by a cell when there is no load attached. It corresponds to the total voltage drop across all of the junctions in the cell. This voltage depends heavily on the built-in voltages of the p-n junctions in the cell, with the maximum achievable open circuit voltage equaling the sum of the built-in voltages of the junctions in the cell, as in Equation 1.30.

$$V_{oc} = \frac{kT}{q} \ln \left( \frac{N_A N_D}{n_i^2} \right) \quad 1.30$$

As a matter of practicality, this maximum open circuit voltage is rarely realized in a physical cell. In order to realize the maximum possible open circuit voltage, unavoidable parasitic characteristics of the cell would have to be removed (e.g. nonradiative recombination would have to be zero). In these cases, the open circuit voltage is more conveniently calculated by Equation 1.31:

$$V_{oc} = \frac{kT}{q} \ln \left( 1 + \left| \frac{I_{photo}}{I_0} \right| \right) \quad 1.31$$

where  $I_{photo}$  is the photogenerated current and  $I_0$  is the saturation current for a given p-n junction [7, 105].

The bias voltage is the effective voltage produced by the photovoltaic cell when a load is attached. As a photovoltaic cell is not an ideal voltage source, it

does have some electrical impedance associated with it. As such, the load and the source impedance act as a voltage divider, resulting in Equation 1.32 for the bias voltage  $V_b$ :

$$V_b = V_{oc} \frac{Z_L}{Z_L + Z_S} \quad 1.32$$

where  $Z_L$  is the load impedance and  $Z_S$  is the source impedance. In the case where no load is attached, the bias voltage equals of the open circuit voltage of the cell.

### 1.5.2 Dark Current, Photocurrent, Short Circuit Current, and Load Current

As there are many voltages with similar definitions, so too are there many currents with similar definitions. The dark current,  $I_{dark}$ , for a solar cell is the current that is produced by a photovoltaic cell under no illumination. This is the current that arises from thermally excited carriers flowing to the contacts as a result of being propelled by the built-in voltage at the p-n interface. In the case of a typical diode, this would simply be the diode current of the structure, defined as in Equation 1.33:

$$I_{dark} = qn_i^2 A \left( \frac{D_n}{L_n N_a} + \frac{D_p}{L_p N_d} \right) e^{\left( \frac{V_b q}{kT} - 1 \right)} \quad 1.33$$

where  $n_i$  is the intrinsic carrier concentration,  $A$  is the cross-sectional area of the cell,  $D_n$ ,  $D_p$ ,  $L_n$ , and  $L_p$  are the diffusion constants and diffusion lengths of the n- and p-doped regions respectively,  $N_a$  and  $N_d$  are the acceptor and donor doping concentrations,  $T$  is the lattice temperature, and  $V_b$  is the bias voltage [7].

Photocurrent refers the amount of current generated from an incident light source. In the ideal case for a single junction cell where recombination is

neglected and the absorbance of the material is 1, photocurrent is defined as in Equations 1.34 and 1.35:

$$I_{photo} = qA\phi_g \quad 1.34$$

$$\phi_g = \frac{1}{h} \int_0^{f_g} \frac{1}{f} \frac{dP}{df} df \quad 1.35$$

where  $\phi_g$  is the flux of photons incident on the cell of an energy larger than the band gap, i.e. frequency shorter than the band gap, of the material,  $A$  is the cross-sectional area of the cell,  $h$  is Planck's constant,  $f_g$  is the frequency corresponding to the band gap of the material, and  $P$  is the incident solar power spectrum [30]. This corresponds simply to the amount of photons incident on the cell being converted into carriers and flowing through the cell. For the more general case of a multijunction cell,  $\phi_g$  changes to the form of Equation 1.36:

$$\phi_g = \text{Min}\{\phi_1, \phi_2, \dots\} \quad 1.36$$

Choosing the minimum current flux absorbed by any one of the layers in the cell.

The short circuit current,  $I_{sc}$ , of the cell refers to when the terminals of the cell are attached to a short circuit. This represents the maximum current the cell can produce. The load current,  $I_L$ , like the bias voltage, is a result of attaching a load to a photovoltaic cell. It is defined as in Equation 1.37:

$$I_L = I_{sc} \frac{Z_s}{Z_s + Z_L} \quad 1.37$$

with similar definitions as the bias voltage.

### 1.5.3 Performance Rubrics

A key aspect of the development of photovoltaic cells is how to characterize a cell's performance. The rubrics most commonly used were developed in the early stages of photovoltaic technology as a whole, based on silicon p-n junctions. The rubrics can best be explained in the context of a sample J-V curve, as shown in Figure 1.43.

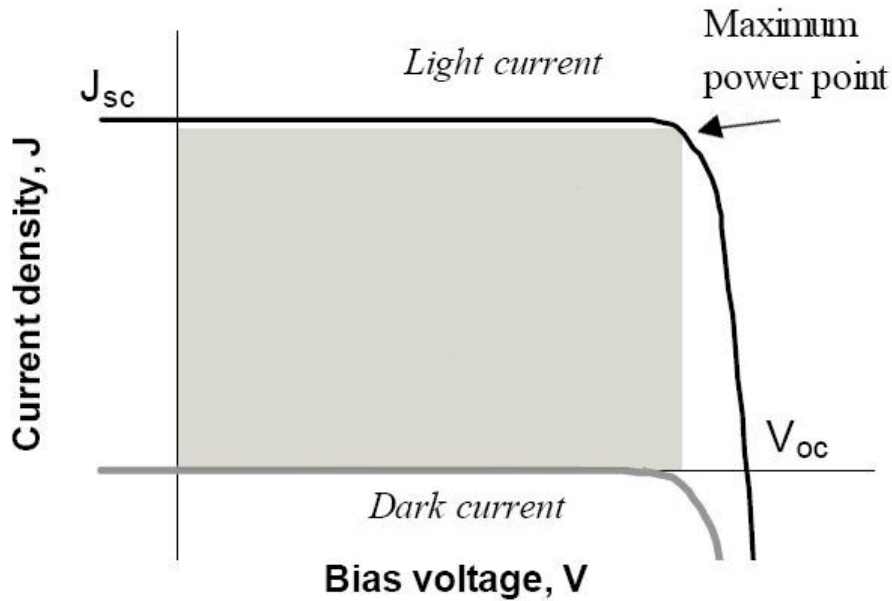


**Figure 1.43:** A comparison of a light current I-V curve and a dark current I-V curve. On the light I-V curve the maximum power point is identified. The power rectangle associated with that point is also illustrated in gray [25].

The points  $I_m$  (current at the maximum power point),  $V_m$  (voltage at the maximum power point),  $I_{sc}$ , and  $V_{oc}$ , along with the incident power on the cell experimentally determined,  $P_{in}$ , are used to define the most commonly used performance rubrics associated with photovoltaics. The first of these, the fill factor, is defined as in Equation 1.38:

$$FF \equiv \frac{I_m V_m}{I_{sc} V_{oc}} \quad 1.38$$

This rubric shows how closely the characteristic I-V curve of the cell matches that of an ideal diode, a rectangle, by comparing the area of the maximum power rectangle of the system to the power rectangle created by the bounds  $I_{sc}$  and  $V_{oc}$  of the system. The closer this value is to unity, the more efficient the cell is. The other, the conversion efficiency, characterizes how much usable energy is delivered to the load of the system in comparison to incident energy, and is defined in Equation 1.39:

$$\eta = \frac{I_m V_m}{P_{in}} = \frac{I_L V_{oc} FF}{P_{in}} \quad 1.39$$

With this rubric, it is a simple matter to then calculate the cost effectiveness of a photovoltaic cell based on this value and the cells production costs [7].

### **1.6 Basic Economics of Solar Cells**

The criterion that may ultimately determine whether photovoltaics are adopted is if cost per unit energy produced by a cell is comparable to that produced by traditional energy sources (e.g. fossil fuels). This statement, however, may seem deceptively simple at first glance, as this cost is dependent on a number of disparate factors. There are a number of ways the cost per unit energy can be improved: including decreasing the cost of manufacturing a cell, lengthening the usable lifetime of the cell, and improving the amount of usable energy a cell produces.

The majority of costs associated with photovoltaic cells currently are associated with the up-front production of the modules (as opposed to maintenance, a direct cost per unit of energy produced, etc.). This cost is differently allocated depending on the type of cell under consideration. For many low- and mid-efficiency cells, like organic, polymer, and silicon cells, rely on low cost materials. Since these cells are necessarily large and needed in significant numbers, costs like module assembly and cell processing become much more significant. For example, a cost analysis of producing a certain type of silicon cell, called *Basepower*, suggested that just under 70% of the cost for this kind of cell comes from module assembly and cell processing [107].

In the case of high-efficiency cells, a different constraint must be additionally considered. Since the materials, such as indium, tellurium, or selenium, used in these cells can be scarcer, to the point where for some materials the entire world's total reserve would be insufficient to produce even a fraction of the amount of devices needed to meet the total energy demand of the planet, the cost of cell manufacturing is generally higher [108]. As such, high-efficiency cells are often made in much smaller sizes, then used in conjunction with concentrating arrays. Even with this, a recent cost breakdown in 2009 for multijunction photovoltaics suggested that the cell cost (not including any module housing) for a typical multijunction photovoltaic cell accounts for approximately one third of the total cost of the device [109]. In order for this type of photovoltaic device to overcome this economic hurdle, the efficiency and lifetime of the device must be significantly higher than its lower efficiency counterparts.

## **1.7 Motivation for Research**

The band gap spacing for triple-junction photovoltaic cells has proven surprising difficult to satisfy in conjunction with other design parameters. Ternary materials based off of GaAs or GaP allow for materials that are very nearly lattice matched while coming close to the ideal band gaps suggested for the two higher energy junctions above in Figure 1.35. A material ideally suited for the third junction in these cells remains unknown to this point, with germanium, with a band gap about 0.25 eV below the ideal value for the lowest junction, often used as the least bad option for the bottom junction (e.g. the record-setting  $\text{Ga}_{0.35}\text{In}_{0.65}\text{P}/\text{Ga}_{0.83}\text{In}_{0.17}\text{As}/\text{Ge}$  cell achieving 41.1% efficiency is evidence of this). This difference from the ideal value represents an opportunity to develop a material that can improve the efficiency of these cells.

It is the purpose of this thesis to verify the optical properties of the ternary material GaTIP and determine if the material would be suitable for use as a bottom junction material with triple-junction solar cells. To this point, a number of groups trying to incorporate thallium into other semiconductor materials have encountered significant difficulty in generating a coherent material [110]. There are a number of challenges incorporating thallium into III-V alloys. One such is the required balance of V-element pressure during growth of the material. In order to prevent the thallium from forming bubbles on the material instead of incorporating into it, growth must be performed under overpressure of the category V element included in the material. V-element overpressure can also lead to an excess of that element in the final material, which means the

overpressure must be as small as possible [111]. Of those that have succeeded of any incorporation at all, most have only succeeded in a thallium content percentage of a few percent [112-114].

## **Chapter 2 Materials and Methods**

The aim of this chapter is twofold. First, as this thesis is heavily based on simulations, an overview of the simulation software will be provided. The methods utilized by the software will be examined. Second, the methods and equipment used to fabricate and test physical samples will be examined. While this thesis does not include testing of samples, it is hoped that the results of this thesis will lead to fabrication and testing of physical samples.

### **2.1 Synopsys Sentaurus TCAD**

The Synopsys software package is utilized to perform simulations and optimize cell designs. This package consists of a number of different modules, each with a unique application. The most significant of these modules are Sentaurus Workbench, Sentaurus Structure Editor, Sentaurus Device, Inspect, and PCM Studio. In order to run a simulation, the first four modules are utilized. To optimize the design, the simulation results are then fed into last module.

#### **2.1.1 Sentaurus Workbench**

Sentaurus Workbench is the graphical user interface of the software package, aiding in organizing a long series of simulations. Workbench allows the other modules to be called sequentially, automatically transferring the output from one module to the input of the next. Variables (e.g. doping concentrations, layer thicknesses, contact widths, etc.) are defined and incorporated into subsequent modules, with each combination of variable values resulting in a new simulation

(e.g. if there are three variables each with three values, there would be twenty-seven total simulations). In the case of a large number of parameters under investigation, this can result in long simulation times. In order to decrease the number of simulations required, an optimization is performed using PCM Studio. Should any output metric be defined and calculated in other modules, such as fill factor or conversion efficiency of a photovoltaic cell, they will be displayed in Workbench as well.

### **2.1.2 Sentaurus Structure Editor**

Sentaurus Structure Editor characterizes the physical structure for a single instance of a device. Structures can be constructed in three dimensions, however, if the device has sufficient symmetry, as in photovoltaic cells, it is sufficient simulate in two dimensions saving system memory. In Structure Editor, each instance of a structure has material layer dimensions (width and height), doping profiles and concentrations, material characteristics (Si, GaAs, etc.), and electrical contacts defined. These properties allow the device to interact with other structures or the environment.

Following design of the device, it must then be meshed. Meshing is where each material layer of a device is divided into a number of smaller regions. The mesh can be defined by the user, allowing for more precise control of ensuing calculation. Large mesh regions allow for faster calculation of simulation results, but small mesh regions allow for more precise results, which is especially important in areas of particular interest (e.g. material interfaces, in the immediate

area of a small structure of interest, etc.). In general, for any uninterrupted area of a single material large mesh regions are sufficient. For thin material thicknesses or small features, a smaller mesh region is required. A sample of a plot generated by the Structure Editor is provided in Figure 2.1.

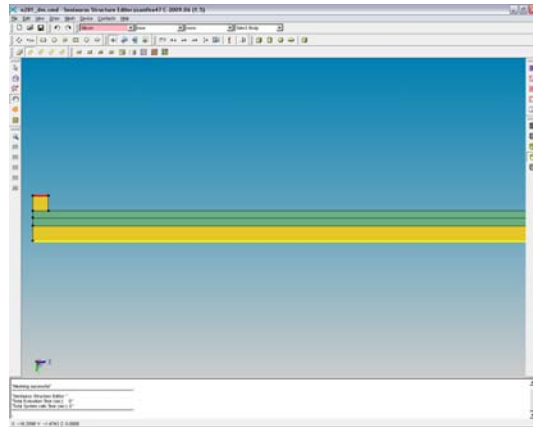


**Figure 2.1:** A sample output from Sentaurus Structure Editor, showing the physical structure of a single junction photovoltaic cell.

### 2.1.3 Sentaurus Device

Whereas in the Structure Editor a device is constructed, in Sentaurus Device the device is simulated. Sentaurus Device imports a mesh, such as the output from the Structure Editor, and runs a simulation which includes external factors (incident spectrum of light, bias voltage, etc.) and internal factors (optical generation of carriers, recombination rates, band bending, etc.). The mesh of the device is simulated in large part using the Transfer Matrix Method (TMM), further explained in section 2.3.1. The simulation results are saved to a number of data files, which can be analyzed using other modules in the software package.

Formatted: Highlight

For all simulations, the incident spectrum was a standardized AM1.5d spectrum. Bias voltage was swept from 0V to a voltage larger than the open

circuit voltage. It should be noted that Sentaurus Device does not calculate device metrics such as fill factor or conversion efficiency. Rather, Sentaurus Device accumulates simulation data which can be used to calculate those metrics.

### 2.1.3.1 Transfer Matrix Method

The most intensive calculations in Sentaurus Device are carried out using the Transfer Matrix Method. The Transfer Matrix Method separates a large, complex structure into smaller, simpler pieces. For most applications, different portions of a photovoltaic cell are characterized by different materials. When determining region divisions, each region must be homogeneous, isotropic and optically linear throughout. An example of allowed and prohibited regions is shown in Figure 2.2.

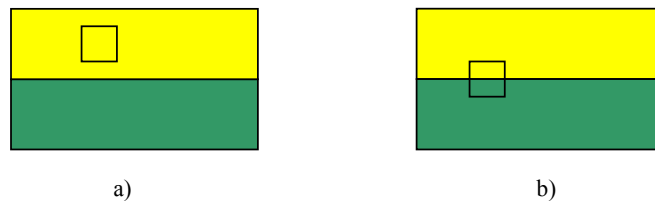


Figure 2.2: In each image, a region (box outline) is defined near the interface of two different homogeneous materials (yellow and green boxes). The region in a) is allowed, as the region is composed of a single, homogeneous material. The region in b) is prohibited, as the region contains the interface of two materials.

Each region has an associated characteristic transfer matrix. Much like transfer functions utilized frequently in circuit design, these matrices can be combined to illustrate features of the cell, such as regions of homogeneity or material interfaces. They can also be adapted to take into account the characteristics of those features (e.g. varying material index of refraction or curvature of interface).

The difference between transfer functions and transfer matrices is that functions only act on a single characteristic, whereas matrices can act on many characteristics at once.

The transfer matrices utilized in Synopsys are remarkably complex and capable of calculations in three dimensions for numerous parameters. As a means of illustration, a simplified calculation will be presented. This calculation is to illustrate the Transfer Matrix Method, and should not be taken as the extent of the calculations performed by the software package.

Consider the case of a monochromatic beam of light incident upon a single layer of a flat, perpendicular photovoltaic cell in one dimension. The beam of light can be represented as a superposition of leftward and rightward travelling waves as in Equation 1.1:

$$E(x) = E_r e^{ikx} + E_l e^{-ikx} \quad 2.1$$

where  $E(x)$  is the magnitude of the electric field at a given point  $x$ ,  $E_r$  and  $E_l$  are respectively the magnitude of the electric field of the rightward and leftward travelling waves,  $i$  is the imaginary unit, and  $k$  the wave number for the beam. Additionally, the spatial derivative of this beam of light is represented as in Equation 2.2:

$$E'(x) = \frac{dE}{dx} = ikE_r e^{ikx} - ikE_l e^{-ikx} \quad 2.2$$

To determine the values for  $E(x+L)$  and  $E'(x+L)$ , the magnitude of these functions a distance  $L$  away from point  $x$ , the following matrix, shown in Equation 2.3, can be used:

$$M = \begin{bmatrix} \cos(kL) & \frac{\sin(kL)}{k} \\ -k \sin(kL) & \cos(kL) \end{bmatrix} \quad 2.3$$

and the calculation to determine  $E(x+L)$  and  $E'(x+L)$  is performed in Equation 2.4:

$$\begin{bmatrix} E(x+L) \\ E'(x+L) \end{bmatrix} = M \begin{bmatrix} E(x) \\ E'(x) \end{bmatrix} \quad 2.4$$

Further, the equation can be generalized by substituting  $M_{total}$  for  $M$ , where  $M_{total}$  is shown in Equation 2.5:

$$M_{total} = M_N \cdot \dots \cdot M_2 \cdot M_1 \quad 2.5$$

Here,  $M_1$  represents the first feature the beam of light strikes and  $M_N$  represents the last [4].

In a TMM program, the input to the combination of transfer matrices is a collection of monochromatic plane waves of varying magnitudes with arbitrary angles of incidence and polarization states. The output from each matrix contains the same elements, varying in magnitude due to the transfer matrix. Each characteristic under investigation (such as incorporating all three dimensions, separating electric field into normal and perpendicular components, including the magnetic field, including angles of incidence in three dimensions, using a spectrum instead of monochromatic light, and many others), quickly increases the size and complexity of each transfer matrix. Computer software is necessary to carry out these calculations especially in the case of large, complex structures and numerous variables.

## 2.1.4 Inspect

Inspect utilizes raw data from the Sentaurus Device module, performs a few simple calculations, and then graphs the results. These plots can be composed of any variables or results specified during the simulation in Device. Additionally, Inspect can perform simple mathematical operations such as multiplying voltage and current to get power. This feature of Inspect is used to produce plots of I-V and P-V curves for various simulated photovoltaic cells. A sample of the plots produced is shown in Figure 2.3.

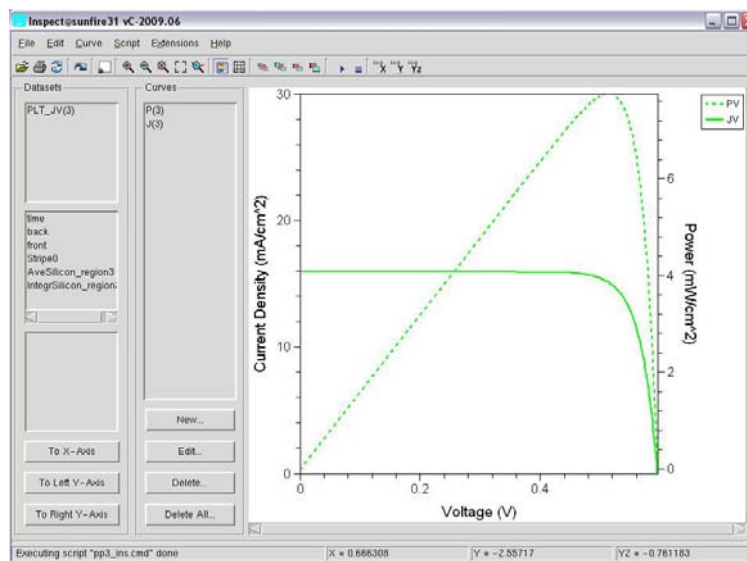


**Figure 2.3:** A sample of the plots produced by Inspect, utilizing data imported from a Sentaurus Device simulation of a solar cell.

Inspect can also be used to extract individual results from simulations performed in Sentaurus device. These results include short circuit current density, open circuit voltage, or the maximum power point (perhaps the most useful in the case of photovoltaics). Once the maximum power point is identified, the fill factor and conversion efficiency can be calculated for any simulated conditions.

## 2.1.4 Tecplot

Tecplot also takes raw data from the Sentaurus device module, but does so in a different fashion than Inspect. Whereas Inspect is used to generate simple plots between a handful of circuit parameters (e.g. contact voltages, current values, etc.), Tecplot is used to generate spatial plots of a structure. These plots can be used to determine current and carrier densities, the rate of optical generation, and various other parameters throughout the entire cell. The program can also be adapted to look at various cell parameters along a 1-D strip of a cell. This feature was used to take a cross-section of cells investigated, from which a band diagram for the cell is produced. A sample of the plots produced is shown in Figure 2.4.

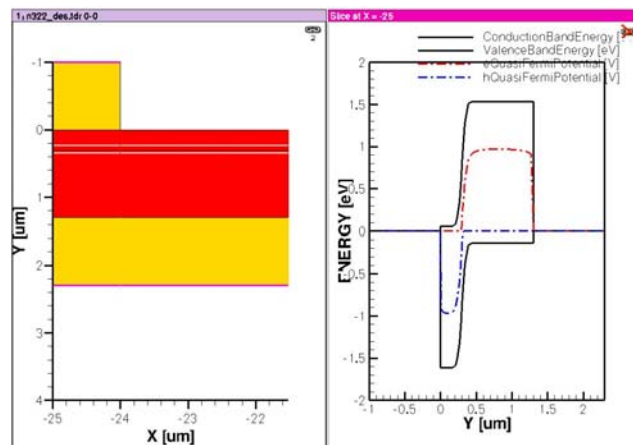


**Figure 2.4:** A sample of plots generated by Tecplot. On the left is a spatial plot of a single junction solar cell. On the right is the band structure of the cell, taken along a 1-D strip on the far left of the cell.

## **2.2 Fabrication Equipment and Deposition Methods**

### **2.2.1 Molecular Beam Epitaxy**

Molecular beam epitaxy (MBE) is a process used to grow highly pure layers of crystalline semiconductor material. The main growth chamber of the MBE system is kept at an ultrahigh vacuum on the order  $10^{-11}$  Torr and is capable of growth temperatures up to 800°C. Vacuum this high must be maintained in order to ensure as few impurities as possible are introduced to a sample during the long growth process. In addition to the main chamber, there are a number of additional source chambers, each containing an elemental material source. These source chambers are also kept under this ultrahigh vacuum and separated from the main growth chamber by a shutter. Growth is accomplished by opening the shutter or shutters between the desired growth material or materials. Should only one source be in use, the growth will naturally be of that material only. Should multiple sources be in use, then the composition of the material will depend greatly on the relative deposition speeds of the materials. These shutters allow for sharply defined material profiles during crystal growth.

Deposition rate in an MBE system is typically slow, on the order of 1  $\mu\text{m/hr}$ , but it does offer some advantages in terms of crystal growth. MBE systems are capable of growth of crystalline layer thickness as thin as an atomic monolayer. Additionally, since the rate of growth is so slow, it allows for careful monitoring of growth conditions *in situ*. Particularly in cases of ternary materials, where relative deposition rates are just as important as absolute deposition rates, this ability is invaluable. The tradeoff in MBE systems is between achieving the

highest quality crystalline films and the slow, complicated, and expensive processing required to accomplishing those films.

### **2.2.2 Photolithography**

Photolithography is used to discriminately deposit layers of material on a sample. A common example in the case of photovoltaics would be deposition of the top contact of a cell. This contact generally includes a region of gold along the perimeter of the cell as well as narrow ‘fingers’ which run along the active face of the cell. Most deposition methods are incapable of depositing layers with any sort of lateral precision, so photolithography is used to deposit a layer of material before a precision deposition which is later removed from sample after deposition is complete. It is the intention for this section to describe a general photolithographic process.

Photolithography in the broadest sense is performed in seven steps. First, the sample is cleaned of any impurities that may have formed on the sample surface. For epi-ready samples with low amounts of surface impurities, the general wafer preparation consists of a series of acetone, isopropanol, and deionized water baths followed by a post-bath bake to remove any remaining moisture. In the case of heavier coverage of surface impurity, additional cleaning methods may be required. HMDS primer spun for 30 sec at 5000 rpm followed by a 30 sec bake at 115°C. Photoresist (e.g. polymethylmethacrylate (PMMA)) and, if required to improve adhesion of the photoresist to the sample surface, primer is deposited on the sample. Both are typically deposited onto the sample

utilizing a spinner; the exact procedure (spin speed, spin duration, ramp up, amount of resist used) depending heavily on the process performed. Third, the sample is placed in a mask aligner (e.g. OAI 204IR Aligner), seen in Figure 2.5, holding the sample in place under an ultraviolet radiation source calibrated to 20 mW/cm<sup>2</sup> at the I-line of a mercury lamp (365.4 nm). A mask is placed on the surface of the sample, which is patterned, to selectively expose regions of the sample to the UV radiation. This mask can be made out of any UV absorbing material, but there a number of materials that have become standards for this use, such as chromium. Fourth, the sample is exposed to UV radiation, the duration of which is determined by the chemistry of the photoresist used. When photoresist is exposed to UV radiation, it undergoes a chemical change, separating the photoresist into regions of exposure and non-exposure. Which region is then removed, the exposed or non-exposed, depends on whether the photoresist used was positive or negative. When a positive resist is used (e.g. Shiply 1813), the exposed resist is rendered soluble to additional chemical processes, which can be utilized to remove the photoresist on the exposed regions of the sample. For negative resists (e.g. SU-8), the opposite is true. Exposure to UV light renders the photoresist insoluble and unexposed regions can be removed with a chemical solvent.



**Figure 2.5:** An image of the OAI 204IR Mask Aligner.

Following UV exposure, the photoresist is developed. During development, part of the photoresist (the exposed portion in with positive photoresists, the unexposed with negative) is removed. In some processes, a short  $O_2$ -RIE (reactive ion etch) may be used to ‘descum’ the sample, removing excess photoresist, but this is not required in all cases. This leaves a selectively deposited layer of photoresist on the sample. The sample can then be used in a number of deposition techniques, such as sputtering or evaporation. Following deposition, the remaining photoresist is removed from the sample in a process called lift off, generally a more vigorous removal process than used during development. In the case of particularly thick layers of the deposited material, sonication may be necessary to assist with lift off. The end result is the selective deposition of a material on the sample [115].

### **2.2.3 Rapid Thermal Annealing**

Rapid Thermal Annealing (RTA) is typically used during the later stages of cell processing when an annealing step is required, for example in the creation of ohmic contacts. RTA systems are typically capable of raising temperature by as much as 30° C/sec up to temperatures reaching as high as 1300° C, with individual anneals lasting two minutes or less at maximum temperature. One of the strengths of RTA is that it can be used even features of the sample may be altered or damaged from prolonged exposure to high temperature (e.g. a doping profile in a region of a sample may diffuse a sufficient amount to alter the performance of a sample under a high enough heat load). In these cases, RTA can perform an anneal to satisfy the fabrication procedure without damaging other structures of the sample.

### **2.2.4 Ion Beam Deposition**

Ion beam deposition, also known as sputtering, is a popular method for depositing high purity films on a sample. The greatest advantage of this system is the wide range of materials that can be deposited. This is due to the fact that the tool is based primarily not on a chemical process, but instead a physical one. The ion beam sputtering system operates by first igniting a DC argon plasma. The argon plasma generates free electrons and positive argon ions, which are essential to the operation of the tool. On the periphery of the plasma is a pair of gratings. The first grating (known as the accelerator) is held at a variable negative potential and acts to accelerate positive argon ions to and then through the grating toward

the neutralizer. The neutralizer generates a cloud of electrons such that the majority of the accelerated positive ions are insulated from the accelerator, maintaining the momentum gained from passing through the negative potential. The possibility remains that neutralizer may not shield all of the accelerated ions from the accelerator, resulting with the occasional high energy ion impacting with the accelerator. To prevent the damage this would cause, a second grating is positioned between the neutralizer and the accelerator and held at a floating potential. Any ions that would impact the accelerator would then instead impact this protecting grating. The ions accelerated by the accelerator and neutralized by the neutralizer strike a target composed of the material to be deposited. The kinetic energy of the argon ions striking the target ejects atoms of the target material. This material then accumulates on any exposed surface in the chamber. This includes both on the sample, forming a thin and highly uniform film, as well as on chamber side walls.

The conditions used for the tool are generally amenable to most materials. The argon gas used to generate the plasma is chemically non-reactive with most materials, so there is little chance of unintended chemical reactions. Since the target material is ejected due to kinetic energy, nearly any material can be used as a target and sputtered, allowing for great versatility. The process also generally runs in a low vacuum. There are some disadvantages to using this type of system, though. Should the argon ions impact the deposited material at too high of an energy, a lower quality film will result.

### **2.3 IV-Station**

The Oriel IV-Station is used in the course of this research to evaluate the performance of individual photovoltaic cells using a variety of metrics, including examples such as fill factor, short circuit current, open circuit voltage, and others described in the introduction. This apparatus offers a variety of advantages as compared to a solar concentrator which utilizes the sun as a radiation source. Ultimately, testing solar cells under actual solar radiation is the most accurate representation of what they would encounter in practical application, however there are a number of issues that make such testing unreliable. Solar radiation intensity on a given day can rely on a number of variables, including location on the globe, time of the year, and weather conditions [116-118]. Weather considerations must be taken into account in regard to the durability of the photovoltaic cells being researched, which often lack weatherproof packaging and can be very delicate. Additionally, it can be very difficult to accurately measure the exact amount of incident sunlight incident on the cell, increasing the error in any performance metric calculated.

The IV-Station provides a method circumventing those concerns while providing an incident spectrum nearly identical to that of the sun. The station is composed of a number of different devices, namely the solar simulator, a holding station, a reference cell, a sourcemeter, a series of ND filters, and the appropriate computer software to accumulate and process data. These devices work in unison to create an accurate incident spectrum. The other components of this station are detailed below.

### 2.3.1 Solar Simulator

The central component of this station is the solar simulator, which generates, collimates, focuses, and orients the light onto the photovoltaic cell. The solar simulator utilizes a 1600 W Xe lamp, powered by a stand-alone power supply, to generate solar energy. The light generated by the lamp is collected by an assortment of optics and reoriented through a filter. This filter is matched to the output spectrum of the Xe lamp such that the resulting spectrum closely resembles the AM1.5 solar spectrum, under concentration. The light is then redirected by another series of optics out of the solar simulator in a 4" x 4" square onto the holding station at an intensity that is typically in the range of 10-12 suns. An image of the solar simulator is shown in Figure 2.6.

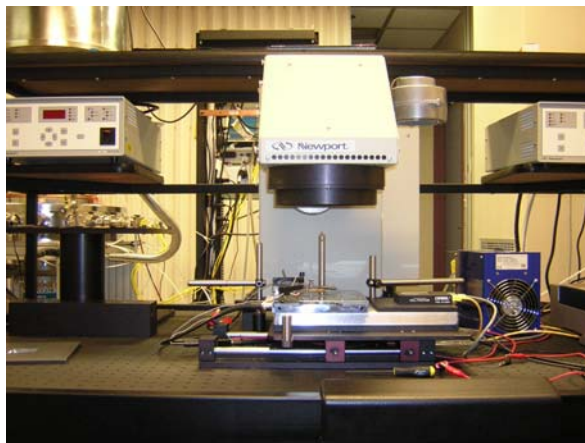


**Figure 2.6:** An image of the solar simulator.

### 2.3.2 Test Area and Probing Stations

The holding station is comprised of two separate portions on a sliding rail system. The first portion consists of an open test area with a temperature diode and a vacuum port in the center. The temperature diode is used in conjunction

with the thermoelectric chiller described in Section 2.1.5 to maintain a stable operating temperature during experimentation. The vacuum port is connected to a vacuum pump, which is used to keep the cell in the same position in the test area. The other portion consists of a reference cell, described in Section 2.1.3. These two portions of the station are located on a single plate which can be slid along a pair of rails and then secured such that only one of the two is under illumination from the solar simulator at any given time.

In order to make electrical contact to a cell, a pair of probing stations is used. Each station is positioned on an attachment to the test area, mounted using magnets to maintain stability. Each probe ends with a narrow-tip needle, which is used to make contact with a sample, which can then transfer information to the source meter. The probe tip is capable of minute adjustments in three dimensions utilizing a pair of joints, one joint for directions parallel to the plane of the sample and one for the direction perpendicular to plane of the sample. Two probe stations are utilized to make electrical contact with both the front and back contacts of the cell. An image of the test area and the probe station is show in Figure 2.7.

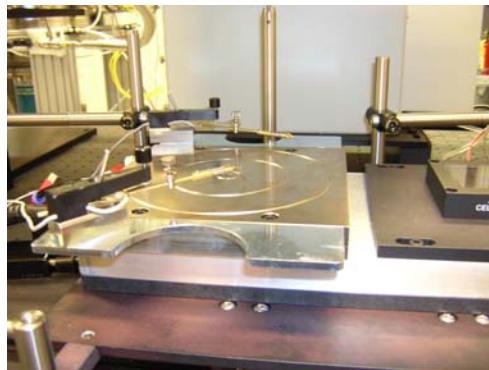


**Figure 2.7:** An image of the test area and probe stations.

### 2.3.3 Reference Cell

Slight variations in environmental conditions will cause the solar simulator to produce marginally different light intensities from experiment to experiment. To account for this, a reference cell is utilized to determine the precise solar intensity at the time of the experiment. The reference cell, composed of a 2 cm x 2 cm silicon monocrystalline silicon photovoltaic cell housed in aluminum housing, is capable of accurately measuring solar intensities in the range of 0.1-3.5 suns with a 0.2% error and a resolution of 0.001 suns. Above 3.5 suns, not only is the reference cell unable to take readings, but prolonged exposure can damage the equipment.

It should be noted that the maximum allowable intensity for the reference cell is approximately 3.5 suns, while the solar simulator produces an intensity upwards of 12 suns. A number of neutral density (ND) filters are used to prevent damage to the reference cell. These filters allow approximately the same percentage of light through at all frequencies, that percentage being determined by their optical density (OD), with individual filters having transmittances ranging from as high as .9+ to as low as .001, reflecting all other incident light. This provides a degree of flexibility in determining the concentration of the solar spectrum incident on a sample. The ND filters are placed in spring-loaded filter holders and held in the path of illumination from the solar simulator over the reference cell, reducing the intensity of light incident on the cell to a level where the reference cell can make an accurate reading. Since the transmittance of each filter can be determined by its optical density, this reading can be used to

determine what the intensity of the solar simulator radiation is precisely. While the primary purpose of these filters is to reduce the intensity of light on the reference cell, they can also be utilized to adjust the intensity of light incident on the photovoltaic cell being examined. Should lower intensity illumination be required, either out of concern of the fragility of the cell or to test under a variety of conditions, a ND filter may be used to reduce the intensity of incident sunlight generated from the solar simulator's standard level to a more satisfactory level. An image of the reference cell is shown in Figure 2.8

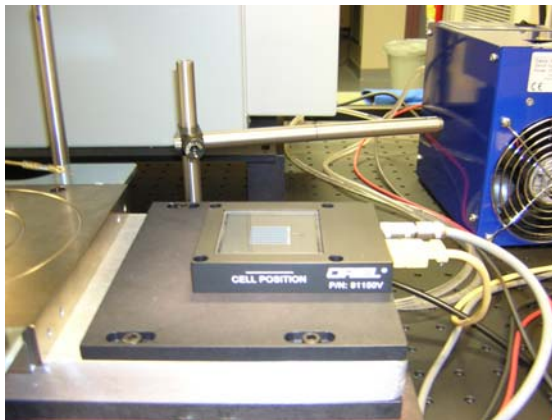


**Figure 2.8:** An image of the reference cell.

### **2.3.4 Thermoelectric Chiller**

Due to the high intensity of light emitted by the solar simulator, the temperature of a PV cell can rapidly climb. To prevent overheating, a thermoelectric chiller is connected to the test area by plastic tubing and is then programmed to maintain a specific temperature. The chiller pumps a mixture of propylene glycol and deionized water into the test area, cooling both the sample and the sample holder. An image of the thermoelectric chiller is shown in Figure 2.9.



**Figure 2.9:** An image of the thermoelectric chiller.

### **2.3.5 Sourcemeater**

The last portion of the test station is the sourcemeater, which is used to take current and voltage readings from the photovoltaic cell under examination. The sourcemeater is connected to the cell either by leads (if wires have attached to the contacts of the cell) or probes (if the cell has bare contacts) and then placed under illuminated area. The duration of illumination is typically limited 15 seconds or less, to limit the amount of heat that accumulates in the cell during testing. Information is then processed by the SolarTest software package, specifically designed for use with the test station. The software then determines many of the important characteristics of a photovoltaic cell. These characteristics include  $V_{oc}$ ,  $I_{sc}$ , maximum power point, fill factor, conversion efficiency, and series and shunt resistance. Under illumination from the solar simulator, the light I-V characteristics are measured. The same readings, taken under ambient laboratory conditions, provide the dark I-V characteristics. An image of the sourcemeater is shown in Figure 2.10.



**Figure 2.10:** An image of the sourcemeter.

## **2.4 Other Testing Apparatus**

### **2.4.1 Spectroscopic Ellipsometer**

Many compounds utilized in layers of photovoltaic cells, such as GaAs, InGaP, and many others, have well characterized optical properties that can be acquired from various databases and research groups. Should an uncharacterized material be under investigation, the ellipsometer provides a method of acquiring this data. The spectroscopic ellipsometer is capable of determining thicknesses of material layers as well as values for the complex index of refraction of a material ( $n + ik$ ) across a range of wavelengths (193-1700 nm) by performing a number of experiments using different input wavelengths of light. The data can be imported to a simulation program or used to determine other characteristics of the material, such as electrical permittivity. The layer under examination need not be the only layer in the sample or even the topmost layer in the sample, but it should be the only layer which is of an uncharacterized material.

An ellipsometer can be considered in four sequential stages: a light source, an input stage, a sample stage, and an output stage. An example of this can be

seen in Figure 2.11. The light source provides a constant intensity of a single wavelength of light to the input stage. This can be accomplished either using a single wavelength laser or spectral source along with a monochromator. The second stage takes the input light, which is composed of all polarizations, and runs through a polarizer such that only one polarization of light is allowed past. The sample stage holds the sample stationary in the ellipsometer. The output stage passes the light through an analyzer before collecting it with a photodetector and analyzing it using computer software. In general, the ellipsometer provides the most accurate results when circularly polarized light is incident on the analyzer. This can be attained utilizing various filters, such as quarter-wave plates, in either the input or output stages to ensure this condition.

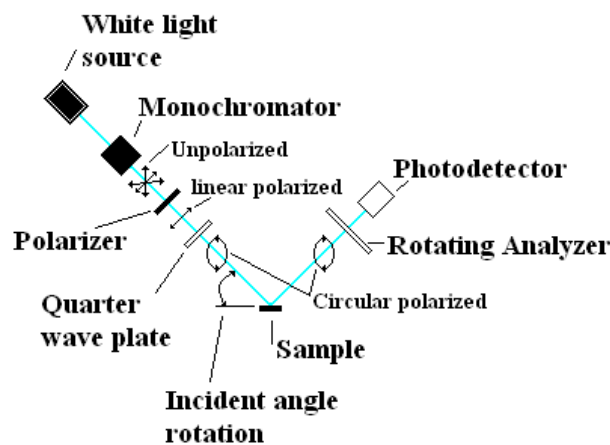


**Figure 2.11:** A diagram of a spectroscopic ellipsometer. In this case, the light source is a white light source and a monochromator, the input stage is a polarizer for producing linearly polarized light and quarter wave plate, the sample stage is just the sample, and the output stage is the analyzer and the photodetector [26].

## **Chapter 3 Band Gap Optimization of Split Junction Solar Cells**

As discussed in Chapter 1, placement of the band gap energies of individual junctions in a cell is a crucial factor in determining overall efficiency. The size of each junction's band gap should be as large as possible to maximize the open circuit voltage ( $V_{oc}$ ) for each junction. Conversely, each junction must also have a band gap energy small enough to absorb a sizable portion of the solar spectrum, generating a large photocurrent. Further, as multijunction cells act akin to voltage sources in series, the currents generated in each junction should be identical, as the series current through the sources will be limited to the lowest current generated by any single junction of a cell. Determining where to place the band gaps of materials can become a complicated engineering problem before physical fabrication of the devices even begins. Split junction cells add another degree of complexity to the design process. Splitting the incident spectrum into multiple components necessitates an optimized cell for each segment of the spectrum.

In this chapter, MATLAB is utilized to optimize band gap placement for both multijunction and split junction photovoltaic cells. In the case of multijunction cells, single, double, and triple junction cells were optimized for output power. The resulting band gap locations were then compared to published data for multijunction cells for verification. The same process was then applied to split junction cells. For the purpose of this thesis, it was assumed that a single dichroic filter would be used in a physical setup, implying that there would be a

single split in the incident solar spectrum and two cells requiring optimization. The incident solar spectrum was split at different wavelengths, simulating different cutoff frequencies for the dichroic filter. These cutoff wavelengths were chosen to correspond to commonly used materials in solar cells. For all optimizations, an initial experiment was performed with material constants (e.g. effective masses of holes and electrons) corresponding to a ‘typical’ III-V semiconductor, working on the assumption that most of the materials of interest would fall in this range. This first experiment would provide approximate band gap energies, allowing for appropriate material choices. The characteristics for these materials were then substituted in for the ‘typical’ values and the experiment was repeated. These results are reported in the subsequent sections.

### **3.1 Full Spectrum Solar Cells**

#### **3.1.1 A Single Junction Full Spectrum Cell**

As a means of illustrating the optimization process, it will first be demonstrated in the context of a single junction, full spectrum solar cell. The maximum possible power generated by a solar cell,  $P_{out}$ , corresponds to an ideal fill factor of 1, and is determined by Equation 3.1 [105]:

$$P_{out} = V_{oc} I_{sc} \quad 3.1$$

where  $V_{oc}$  is the open circuit voltage and  $I_{sc}$  is the short circuit current. Both of these quantities are dependent on the material properties of the junctions in the cell and require further calculation.

For a single junction solar cell,  $V_{oc}$  is defined using Equation 3.2 [105]:

$$V_{oc} = \frac{kT}{q} \ln\left(\frac{N_a N_d}{n_i^2}\right) \quad 3.2$$

Where  $N_a$  and  $N_d$  are the acceptor and donor doping concentrations and  $n_i$  is the intrinsic carrier concentration. The variable  $n_i$  is calculated using Equation 3.3 [7]:

$$n_i = \sqrt{N_C N_V} e^{-E_g/2kT} \quad 3.3$$

Where  $N_C$  and  $N_V$  are the density of states of the material used in the conduction and valence band, respectively, and  $E_g$  is the band gap of the material in eV.  $N_C$  and  $N_V$  are inherent to a given material, whereas  $E_g$  is the variable under investigation.

For a single junction solar cell,  $I_{sc}$  is defined relying heavily on the characteristic equations for a diode using Equation 3.4 [7]:

$$I_{sc} = I_v - I_{dark} \quad 3.4$$

where  $I_v$  is the light-generated current and  $I_{dark}$  is the diode current.  $I_{dark}$  is characterized in Equation 3.5 [7].

$$I_{dark} = qA \left( \frac{D_n n_i^2}{L_n N_a} + \frac{D_p n_i^2}{L_p N_d} \right) e^{\left( \frac{V_{oc} q}{kT} - 1 \right)} \quad 3.5$$

Where  $q$  is the magnitude of electric charge,  $A$  is the cross-sectional area of the cell,  $D_n$  and  $D_p$  are the diffusion constants for the n- and p-doped regions of the p-n junctions,  $L_n$  and  $L_p$  are the diffusion lengths,  $V_{oc}$  is the open circuit voltage calculated above,  $k$  is the Boltzmann constant, and  $T$  is the cell temperature. Most of the parameters are either intrinsic to specific materials or are design choices.

$I_v$ , the photocurrent generated, is generally characterized by Equation 3.6:

$$I_v = \frac{qA}{h} \int_0^{f_g} \frac{1}{f} \frac{dP}{df} df \quad 3.6$$

where P is the incident solar power spectrum. In short, every photon with a frequency shorter than the band gap of the material generates a single carrier pair. For the purposes of this model, recombination losses are ignored (assuming they are reasonably consistent across different materials).

In calculations for this optimization, the integral in Equation 3.6 is approximated. The AM1.5G ASTM G173-03 reference spectrum was used to determine the number of photons at each frequency [2]. The reference spectrum supplies the solar energy density in different frequency ranges, using step sizes of as low as .5 nm at short wavelengths and as high as 5 nm at long wavelengths, from which the number of photons in that range is easily calculated, using the amount of energy present in a single photon at that frequency. As the reference spectrum supplies data by wavelength, as opposed to frequency, the Equation 3.6 was adapted to suit it. The modification follows Equation 3.7:

$$I_v = \frac{A}{h^2} \sum_{\lambda=0}^{\lambda_g} \frac{P_\lambda}{\nu_\lambda} \quad 3.7$$

where  $P_\lambda$  is the amount of power in a given wavelength range,  $\nu_\lambda$  is the frequency corresponding to that wavelength, and  $h$  is Planck's constant.

Once calculated, the ideal band gap placement for a single junction solar cell was compared to results published previously to ensure the program was performing calculations properly. The source used for verification was Zdanowicz et al.[21]. Slight modifications were made to the reference spectrum in this paper, to account for various atmospheric conditions. With these

modifications, a small amount of variation between calculations is to be expected.

The results are displayed in Figure 3.1.

Calculated	Zdanowicz et al.	Difference
897 nm (1.38 eV)	899 nm (1.38 eV)	2 nm (.002 eV)

**Figure 3.1:** Ideal band gap placement for a full spectrum single junction solar cell as calculated by the band gap optimization program (left) and Zdanowicz et al. (center) [21]

### 3.1.2 Multijunction Full Spectrum Solar Cells

Following calculation for a single junction full spectrum cell, the program was adapted to calculate optimum band placement for two and three junction cells. Many of the same equations used in the Section 3.1.1 can be used with little modification to be suited for this application.

In the single junction case,  $V_{oc}$  is dependent only on the lone p-n junction.

In the multijunction case,  $V_{oc}$  is dependent on each p-n junction in the cell

described by Equation 3.8 [105]:

$$V_{oc} = \sum_{i=1}^{i_{max}} V_{oc,i} \quad 3.8$$

where  $V_{oc,i}$  is the open circuit voltage of each individual p-n junction of the cell.

Each  $V_{oc,i}$  may be calculated as in Equation 3.2. In the single junction case,  $I_{sc}$  is

by default the current through the only p-n junction. In the multijunction case, as

the cell acts as multiple voltage sources in series, the current through the sources

is limited to the minimum current through any single junction, as described by

Equation 3.9 [105]:

$$I_{sc} = \text{Min}\{I_1, I_2, \dots\} \quad 3.9$$

where  $I_1$  is the current through the first junction,  $I_2$  is the current through the second cell, etc. The current generated by any single junction can be calculated using equations similar to Equation 3.7. The new equation follows the form of Equation 3.10:

$$I_{v,j} = \frac{A}{h^2} \sum_{\lambda=\lambda_{g,j-1}}^{\lambda_{g,j}} \frac{P_{\lambda}}{v_{\lambda}} \quad 3.10$$

where  $I_{v,j}$  is the photocurrent generated by the  $j^{\text{th}}$  junction,  $j_{\text{max}}$  is the number of junctions in the cell, and  $\lambda_{g,j}$  is the wavelength corresponding the band gap of the  $j^{\text{th}}$  junction. It should be noted that for all cells the value  $\lambda_{g,0}$  (i.e. when  $j$  equals 1 for the topmost junction) is 0 nm. The results for two- and three-junction cells are in Figure 3.2 and Figure 3.3.

Calculated	Zdanowicz et al.	Difference
759 nm (1.63 eV)	674 nm (1.84 eV)	85 nm (.21 eV)
1263 nm (.98 eV)	1107 nm (1.12 eV)	156 nm (.14 eV)

**Figure 3.2:** Ideal band gap placement for a full spectrum dual junction solar cell as calculated by the band gap optimization program (left) and Zdanowicz et al.(right) [21]

Calculated	Zdanowicz et al.	Difference
655 nm (1.90 eV)	590 nm (2.10 eV)	65 nm (0.20 eV)
910 nm (1.36 eV)	873 nm (1.42 eV)	37 nm (0.06 eV)
1320 nm (0.94 eV)	1305 nm (0.95 eV)	15 nm (0.01 eV)

**Figure 3.3:** Ideal band gap placement for a full spectrum triple junction solar cell as calculated by the band gap optimization program (left) and Zdanowicz et al.(right)[21]

### **3.2 Multijunction Split Junction Solar Cells**

Adapting the optimizer for use with split junction cells required an additional consideration. In split junction cells, the incident spectrum is split into multiple segments. For the purpose of this thesis, only splitting the spectrum into two segments was considered. Solar cells can absorb energies from both portions of the spectrum, with photovoltaic materials generally used in the shorter wavelength portion of the spectrum and thermophotovoltaic materials in the longer wavelength portion. The changes in the input spectrum cause very slight changes in terms of the equations for generating photocurrent. In fact, for both cells Equation 3.10 can be adapted with the redefinition of some constants. For the PV cell,  $\lambda_{g,j}$  can never exceed the cutoff wavelength of the device used to split the spectrum (as there is no light at wavelengths longer than this in the incident spectrum). For the TPV cell,  $\lambda_{g,0}$  instead equals that same cutoff wavelength (as there is no light at wavelengths shorter than this in the incident spectrum). Otherwise, all the equations described in this chapter still hold for these cells.

A number of different cutoff wavelengths were optimized. The location of these cutoffs were chosen for a variety of reasons, e.g. they correspond to common material substrates or materials commonly used in photovoltaics. In the following sections, the cutoff wavelength will be provided, followed by the motivation for selecting this wavelength. The optimum band placement for both a PV and TPV cell will be provided (single, dual, and triple junctions for a PV cell, single and dual junctions for a TPV cell). Finally, a selection of material suggestions which are nearly lattice-matched will be provided where possible.

This is not possible for junctions of some cells, sometimes due to a lack of well defined materials in the proper energy range or a lack of materials lattice-matched to other junctions in the cell.

### 3.2.1 867 nm Cutoff Split Junction Cell

The first cutoff point investigated is for  $\lambda_{\text{cutoff}}$  equals 867 nm, or 1.43 eV. The cutoff frequency corresponds to the band gap for GaAs, a common substrate material for semiconductor fabrication as well as a material commonly used in photovoltaic cells. Results for single, dual, and triple junction PV and single and dual junction TPV cells are provided in Figure 3.4 and Figure 3.5.

Single Junction	Material Suggestion	Lattice Constant (Angstroms)	Band Gap (eV)
867 nm (1.43 eV)	GaAs	5.653	1.43
<b>Dual Junction</b>			
637 nm (1.95 eV)	$\text{Al}_4\text{Ga}_6\text{As}$	5.656	1.92
867 nm (1.43 eV)	GaAs	5.653	1.43
<b>Triple Junction</b>			
561 nm (2.21 eV)	$\text{Al}_4\text{In}_6\text{P}$	5.6	2.2
708 nm (1.75 eV)	$\text{Ga}_5\text{In}_5\text{P}$	5.66	1.75
867 nm (1.43 eV)	GaAs	5.653	1.43

**Figure 3.4:** Ideal band gap placement for single, dual, and triple junction PV cells in a split junction system. Material suggestions for each junction are provided if applicable.

Single Junction	Material Suggestion	Lattice Constant (Angstroms)	Band Gap (eV)
1329 nm (0.93 eV)	$\text{Ga}_6\text{In}_4\text{As}$	5.815	0.92
<b>Dual Junction</b>			
1195 nm (1.04 eV)	$\text{GaAs}_8\text{Sb}_2$	6.0	1.1
1775 nm (0.70 eV)	GaSb	6.096	0.726

**Figure 3.5:** Ideal band gap placement for single and dual junction TPV cells in a split junction system. Material suggestions for each junction are provided if applicable.

Note that for each of the PV cells, the bottom junction is placed at the cutoff frequency, as the bottom junction for each of the full spectrum cells is at a longer wavelength than the cutoff frequency. This in turn increases the band gap energy of each of the above junctions in the cell. For the PV cells there are well established materials that correspond to the appropriate band gaps and lattice matched to each other at this cutoff.

For the longer wavelength portion of the spectrum, a single junction cell is optimized at a band gap that allows for use of well-characterized materials that are not traditionally considered TPV materials. This results from having a short cutoff wavelength, leaving a large section of the solar spectrum associated with PV materials incident on the TPV cell. For the dual junction cell, the bottom junction band gap is located near the band gap of GaSb, a commonly used TPV material. It may be possible to utilize GaAsSb in the top junction, but this material is not well characterized, so precise properties for specific mole fractions may vary. Should GaAsSb prove well-suited, a two junction TPV cell for this system could be feasible.

### **3.2.2 925 nm Cutoff Split Junction Cell**

The next cutoff point investigated is for  $\lambda_{\text{cutoff}}$  equals 925 nm, or 1.34 eV. The cutoff frequency corresponds to the band gap for InP, a material commonly used in photovoltaic cells. Results for single, dual, and triple junction PV and single and dual junction TPV cells are provided in Figure 3.6 and Figure 3.7.

Single Junction	Material Suggestion	Lattice Constant (Angstroms)	Band Gap (eV)
897 nm (1.38 eV)	InP	5.8687	1.34
<b>Dual Junction</b>			
660 nm (1.88 eV)	Gap 1	NA	NA
925 nm (1.34 eV)	InP	5.8687	1.34
<b>Triple Junction</b>			
579 nm (2.14 eV)	Gap 1	NA	NA
741 nm (1.67 eV)	Gap 1	NA	NA
924 nm (1.34 eV)	InP	5.8687	1.34

**Figure 3.6:** Ideal band gap placement for single, dual, and triple junction PV cells in a split junction system. Material suggestions for each junction are provided if applicable.

Single Junction	Material Suggestion	Lattice Constant (Angstroms)	Band Gap (eV)
1329 nm (0.93 eV)	Ga <sub>6</sub> In <sub>4</sub> As	5.815	0.92
<b>Dual Junction</b>			
1235 nm (1.00 eV)	GaAs <sub>8</sub> Sb <sub>2</sub>	6.0 (approx.)	1.1 (approx.)
1785 nm (0.69 eV)	GaSb	6.096	0.726

**Figure 3.7:** Ideal band gap placement for single and dual junction TPV cells in a split junction system. Material suggestions for each junction are provided if applicable.

Comparing the results of the PV stages of this section and Section 3.2.1, a number of interesting trends emerge. For the single junction case, the cutoff is at a longer wavelength than the ideal band gap placement for a full spectrum cell. The band placement of single junction cell for the PV stage then converges to the full spectrum placement. For the purposes of this cutoff wavelength (and all subsequent cutoff wavelengths investigated) it is assumed that an InP substrate would be used. This consideration was taken into account for lattice-matching purposes in the other junctions of the cell. For dual and triple junctions, the bottom junction remains at the cutoff wavelength as in the GaAs-cutoff cell in Section 3.2.1. In the triple junction case for the PV stage, there is no well-defined

material at an appropriate lattice constant for the top junction of the cell, as can be seen in Figure 3.8.

The results for the TPV cell are nearly identical to that for the TPV cell in the 867 nm cutoff system. This is not surprising, considering how similar the incident spectrum on this stage is to that of the previous example. As with the 867 nm cutoff system, both single and dual junction TPV cells seem like realistic options.

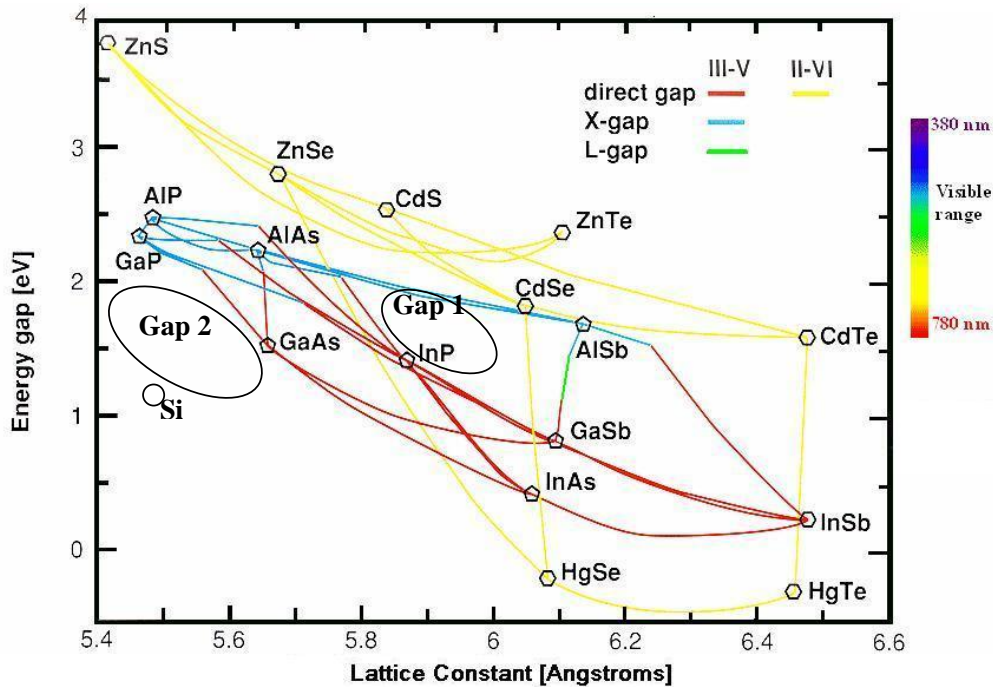


**Figure 3.8:** Lattice constant vs. band gap plot for common group IV, III-V, and II-VI semiconductors. Certain regions of this plot have very few well characterized materials and are denoted as gaps. Gap 1 is germane to the 925 nm cutoff system, while Gap 2 is relevant to the 1100 nm cutoff system. Adapted from [27].

### 3.2.3 1100 nm Cutoff Split Junction Cell

#### 3.2.3.1 1100 nm Cutoff Split Junction Cell – Silicon Based

The next cutoff point investigated is for  $\lambda_{\text{cutoff}}$  equals 1100 nm, or 1.13 eV. The cutoff frequency corresponds to the band gap for silicon. Results for single, dual, and triple junction PV and single and dual junction TPV cells are provided in Figure 3.9 and Figure 3.10.

Single Junction	Material Suggestion	Lattice Constant (Angstroms)	Band Gap (eV)
897 nm (1.38 eV)	Si	5.4310	1.12
<b>Dual Junction</b>			
718 nm (1.72 eV)	Gap 2	NA	NA
1100 nm (1.13 eV)	Si	5.4310	1.12
<b>Triple Junction</b>			
620 nm (2.00 eV)	Gap 2	NA	NA
828 nm (1.50 eV)	Gap 2	NA	NA
1100 nm (1.13 eV)	Si	5.4310	1.12

**Figure 3.9:** Ideal band gap placement for single, dual, and triple junction PV cells in a split junction system. Material suggestions for each junction are provided if applicable.

Single Junction	Material Suggestion	Lattice Constant (Angstroms)	Band Gap (eV)
1761 nm (0.70 eV)	GaSb	6.096	0.726
<b>Dual Junction</b>			
1347 nm (0.92 eV)	$\text{Al}_8\text{Ga}_2\text{Sb}$	6.13	0.9
1761 nm (0.70 eV)	GaSb	6.096	0.726

**Figure 3.10:** Ideal band gap placement for single and dual junction TPV cells in a split junction system. Material suggestions for each junction are provided if applicable.

The PV simulation illustrates the issues with using silicon in multijunction photovoltaics. Silicon has an unusually small lattice constant, as can be seen in Figure 3.8, meaning that there are very few materials that could be deposited on it without strain issues. Those that are lattice matched (e.g. GaP, AlP, etc.) have

band gaps of significantly higher energy than even the highest junction in the ideal band placement. Though silicon has many advantages for use in PV systems, it is not a useful material for this application.

Again, for the single junction TPV cell, GaSb is a convenient material, both in terms of band gap and simple material composition. For the dual junction TPV cell, the top junction is best fit by AlGaSb, however this material has not been well characterized to this point, with most of the data coming from a handful of experimental samples [119].

### **3.2.3.2 1100 nm Cutoff Split Junction Cell – GaAs Based**

Due to issues finding materials at the proper band placement while maintaining the lattice-matched condition with silicon, another examination was performed utilizing GaAs. While GaAs would not be a proper material for the bottom junction of this cell, the intention is that this substrate would allow for use of more combinations of materials in the InGaAs and InGaP families. This would allow for more options in determining possible cells for use in this system. For this case, the TPV cell composition could remain the same as in Section 3.2.3.1, requiring only a change in the PV stage. Results for single, dual, and triple junction PV cells are provided in Figure 3.11.

Single Junction	Material Suggestion	Lattice Constant (Angstroms)	Band Gap (eV)
897 nm (1.38 eV)	GaAs	5.653	1.42
<b>Dual Junction</b>			
718 nm (1.72 eV)	Al <sub>0.25</sub> Ga <sub>0.75</sub> As	5.655	1.74
1100 nm (1.13 eV)	GaTlP	5.6	1.1
<b>Triple Junction</b>			
620 nm (2.00 eV)	Ga <sub>0.7</sub> In <sub>0.3</sub> P	5.57	1.99
828 nm (1.50 eV)	Al <sub>0.06</sub> Ga <sub>0.94</sub> As	5.65	1.50
1100 nm (1.13 eV)	GaTlP	5.6	1.1

**Figure 3.11:** Ideal band gap placement for single, dual, and triple junction PV cells in a split junction system. Material suggestions for each junction are provided if applicable.

While many of the junctions for the single, dual, and triple junction cells have well-characterized materials available that are lattice-matched to a GaAs substrate, the bottommost junction for dual and triple junction cells becomes problematic. Unfortunately, there is no well-characterized material that is lattice-matched to GaAs. The best option is Ga<sub>1-x</sub>Tl<sub>x</sub>P, but this is a material that has exhibited great growth difficulty, particularly in cases with high thallium mole fractions. There have been few cases of mole fractions of thallium exceeding  $x = .1$ , leading to a poorly characterized material in the mole fraction range that would be required for this application [111, 120].

### 3.2.4 1698 nm Cutoff Split Junction Cell

The final cutoff point investigated is for  $\lambda_{\text{cutoff}}$  equals 1698 nm, or 0.73 eV. The cutoff wavelength corresponds to the band gap for GaSb. Results for single, dual, and triple junction PV and single and dual junction TPV cells are provided in Figure 3.12 and Figure 3.13.

Single Junction	Material Suggestion	Lattice Constant (Angstroms)	Band Gap (eV)
897 nm (1.38 eV)	In <sub>0.05</sub> Ga <sub>0.95</sub> As	5.67	1.38
<b>Dual Junction</b>			
760 nm (1.63 eV)	In <sub>0.47</sub> Al <sub>0.53</sub> As	5.83	1.65
1265 nm (0.98 eV)	In <sub>0.35</sub> Ga <sub>0.65</sub> As	5.80	0.98
<b>Triple Junction</b>			
655 nm (1.89 eV)	Ga <sub>0.58</sub> In <sub>0.42</sub> P	5.63	1.84
910 nm (1.36 eV)	Ga <sub>0.95</sub> In <sub>0.05</sub> As	5.67	1.38
1320 nm (0.94 eV)	Ge/GaTIP	5.65/5.6	0.67/0.9

**Figure 3.12:** Ideal band gap placement for single, dual, and triple junction PV cells in a split junction system.

<b>Single Junction</b>
2346 nm (0.53 eV)
<b>Dual Junction</b>
2106 nm (0.59 eV)
2457 nm (0.50 eV)

**Figure 3.13:** Ideal band gap placement for single and dual junction TPV cells in a split junction system.

For the PV stage, the cutoff wavelength is so long that the ideal bandgap placements are identical to that for a full spectrum cell. As such, it makes little sense to generate material combinations matched to GaSb when the combinations available for full spectrum cells would be more efficient. For the triple junction cell, there is a lack of well-characterized material for the bottom junction that is well matched to the top and middle. Germanium is generally utilized for the bottom junction of these cells, sometimes necessitating tailoring of the other junctions in the cell [121], as it has the closest band gap match for the bottom junction while maintaining a near lattice-matched condition to the materials used

in the top and middle of the cell. GaTIP has the potential for use in the bottom junction of the cell, which will be examined further in Chapter 4.

For TPV cells, there are very few materials which are capable of generating band gaps in the ranges necessary. There are no binary materials in the range desired, meaning that there are no convenient materials that could double as both a bottom junction and substrate. Most of the materials that might suit the junctions, such as GaInSb, AlInSb, InPAs, and AlInAs, have not been extensively characterized. Creating a TPV cell for this system may well be possible, but further research into these materials, particularly their lattice constants, is required.

### **3.3 Conclusions**

The optimum band gaps for PV and TPV cells in a split junction photovoltaic system were determined for systems employing various cutoff wavelengths tuned to practical and commonly used semiconductor materials. The ultimate aim was not only to determine the optimum band gaps for these cells, but also to determine which, if any, cutoff wavelengths had optimum band gaps that corresponded to lattice-matched materials.

As evidenced by the results above, employing a dichroic filter at a wavelength of 1698 nm (i.e. GaSb) does not meet these criteria. As the band gaps for the PV cell match those for the full spectrum cell, with the lowest junction significantly above the band gap suggested by GaSb, leaving a portion of the solar spectrum unutilized. A better result could be obtained by utilizing a full spectrum

cell and designing a dichroic filter to match the band gap of the bottom junction, avoiding this waste. Furthermore, GaSb would not be utilized as the bottom junction of the device as its band gap (0.7 eV) is significantly far away from the optimum placement for the cell (0.53 eV).

The 925 nm (InP) cutoff system exhibited material characterization issues. For the dual and triple junction cells, there is a junction which does not have a well defined material lattice-matched to the other suggested layers. It may be possible to generate such a layer with a novel material, which may be a subject of investigation at a later date. For the time being, these designed possibilities can be dismissed before even looking at the TPV portion of the results.

The 867 nm (GaAs) cutoff system shows promising combinations of materials for both the PV and TPV portions of the system. Were a complete system to be constructed, this system would likely be the easiest to design while still maintaining a high efficiency.

The last remaining possibility, the 1100 nm (Si) cutoff exhibited different issues. Since silicon has such a small lattice constant, there are very few materials latticed matched to it. Those that are do have band gaps that are far from the ideal placement for use in the PV stage of the system. When this system was reexamined utilizing a GaAs substrate in place of silicon, the use of GaTIP was necessitated. The use of this material will be discussed in detail in the Chapter 4.

## **Chapter 4 Simulation of Thallium-Based Multijunction Photovoltaic Cells**

In the previous chapter, band gap placement in solar cells for various applications was examined. In this chapter, individual cells are simulated using the Sentaurus TCAD software package. In particular, cells utilizing thallium-containing junctions, which may be more ideally suited for use in some of the dichroic systems as suggested in the previous chapter, are investigated. As suggested in the previous chapter, there are very few materials that are lattice matched to GaAs, and the slew of ternary materials lattice-matched to it, that also have band gaps in the 1.2 eV and lower range. One such material is GaTlP, but growth of this material is taxing, with mole fractions of thallium over 10% rarely performed. As such, it is important to perform preliminary calculations before growth of a sample to ensure optimum results. Additionally, simulations allow for fine tuning of structure layouts, from specific mole fraction composition to tunnel diode characteristics to contact geometry.

First, individual semiconductor p-n junction solar cells were simulated. Materials were chosen for use in later, more elaborate structures rather than optimization of a single junction system. Proper layer thickness and doping concentrations were optimized for each junction. Next, the properties of the tunnel diodes to be used in the system were investigated. For tunnel diodes, an initial test was performed on a single highly-doped p-n junction. This was followed by simulations of dual junction solar cells, utilizing some of the previous

single junction simulations and requiring use of a tunnel diode between the layers. Use of different materials necessitated different tunnel diode materials, with some of the narrow band gap materials commonly used for bottom junctions in solar cells needing use of quaternary materials. A number of triple junction solar cells were then simulated, with each layer separated by a different tunnel junction. First, cells with well-established efficiencies were simulated, to determine a baseline for further simulations. Then, cells including thallium-incorporating bottom junctions were simulated, aiming to improve total conversion efficiency possible out of the cells. Finally, simulations were performed on cells utilizing a truncated incident solar spectrum, approximating use in the dichoric system outlined in the previous chapter. The cells used in this simulation will be those suggested by the previous chapter. Front and back contacts made of gold were placed on each cell, with the front contact shadowing only a small fraction of the cell.

#### **4.1 Simulation of Single Junction Photovoltaic Cells**

The simplest case for a solar cell involves a single p-n junction. For this section, a number of different materials are simulated. The materials chosen are not intended to be optimum choices for a single junction full spectrum cell, instead corresponding to material choices for triple cells. As such, for materials which are not intended to be the topmost junction in cell, two sets of results are provided. The first shows when the full solar spectrum is incident upon it, the

second when a truncated solar spectrum, resulting from high frequency light being absorbed by wider band gap materials above it in the cell, is.

#### 4.1.1 Simulation of a Single Junction GaInP Cell

For this simulation Ga<sub>0.37</sub>In<sub>0.63</sub>P was utilized. This material has a band gap of 1.61 eV and a lattice constant of 5.714 angstroms. Material thicknesses and doping levels were varied to achieve the highest efficiency for the junction. A physical diagram and equilibrium band diagram for the device is provided in Figure 4.1. Specific dimensions and doping concentrations of the highest performing junction are provided in Figure 4.2. J-V and P-V curves are provided in Figure 4.3. Cell performance metrics are provided in Figure 4.4.

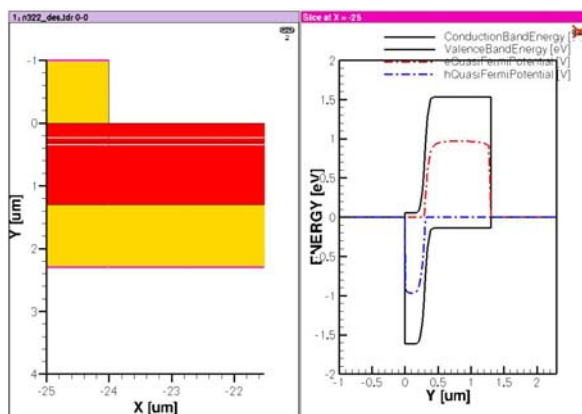


**Figure 4.1:** Physical structure and equilibrium band diagram of a GaInP (red) single junction cell.

Parameter	Value
n-Thickness	0.3 $\mu\text{m}$
p-Thickness	1.0 $\mu\text{m}$
n-Concentration	$1\text{e}17 \text{ cm}^{-3}$
p-Concentration	$1\text{e}17 \text{ cm}^{-3}$

**Figure 4.2:** Structural parameters of GaInP cell.

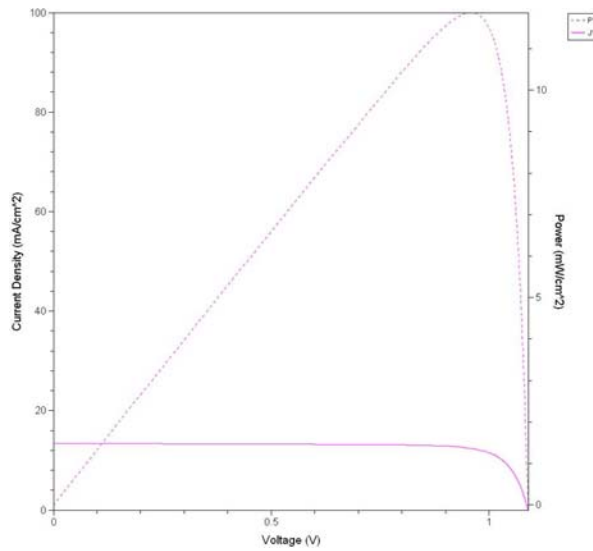


**Figure 4.3:** J-V and P-V curves for the GaInP cell.

Parameter	Value
$J_{SC}$	12.89 mA/cm <sup>2</sup>
$V_{OC}$	1.0778 V
$P_m$	11.35 mW/cm <sup>2</sup>
FF	81.72%
Efficiency	11.35%

**Figure 4.4:** Performance metrics for GaInP cell. Short circuit current density ( $J_{SC}$ ), open circuit voltage ( $V_{OC}$ ), maximum power ( $P_m$ ), fill factor (FF), and conversion efficiency (Efficiency) are listed.

#### 4.1.2 Simulation of a Single Junction InGaAs Cell

For this simulation  $In_{.17}Ga_{.83}As$  was utilized. This material has a band gap of 1.21 eV and a lattice constant of 5.722 angstroms. Material thicknesses and doping levels were varied to achieve the highest efficiency for the junction. A physical diagram and equilibrium band diagram for the device is provided in Figure 4.5. Specific dimensions and doping concentrations of the highest performing junction are provided in

Parameter	Value
n-Thickness	0.5 $\mu m$

p-Thickness	1.0 $\mu\text{m}$
n-Concentration	$1\text{e}17 \text{ cm}^{-3}$
p-Concentration	$1\text{e}17 \text{ cm}^{-3}$

Figure 4.6. J-V and P-V curves are provided in Figure 4.7. Cell performance metrics are provided in

Parameter	Value (truncated spectrum)	Value (full spectrum)
$J_{\text{SC}}$	11.81 $\text{mA}/\text{cm}^2$	22.73 $\text{mA}/\text{cm}^2$
$V_{\text{OC}}$	0.6028 V	0.626 V
$P_{\text{m}}$	5.32 $\text{mW}/\text{cm}^2$	10.84 $\text{mW}/\text{cm}^2$
FF	74.69%	76.19%
Efficiency	5.32%	10.84%

Figure 4.8. In order to get an appropriate response for how this cell would perform as part of a triple junction cell, where part of the incident spectrum would be absorbed by junctions with higher band gaps, simulations were performed with both a full solar spectrum and a truncated spectrum, cutoff at where above cells would stop absorbing light.

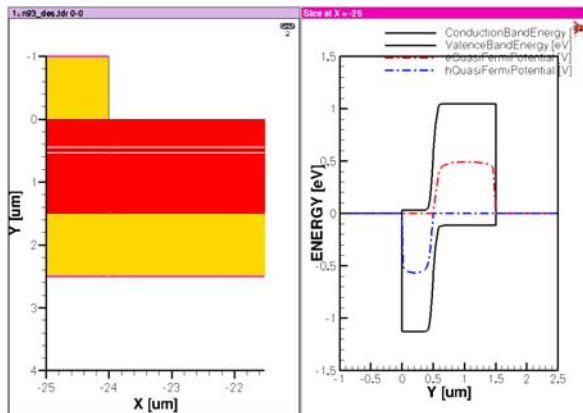


**Figure 4.5:** Physical structure and equilibrium band diagram of an InGaAs (red) single junction cell.

Parameter	Value
n-Thickness	0.5 $\mu\text{m}$
p-Thickness	1.0 $\mu\text{m}$
n-Concentration	$1\text{e}17 \text{ cm}^{-3}$
p-Concentration	$1\text{e}17 \text{ cm}^{-3}$

**Figure 4.6:** Structural parameters of InGaAs cell.

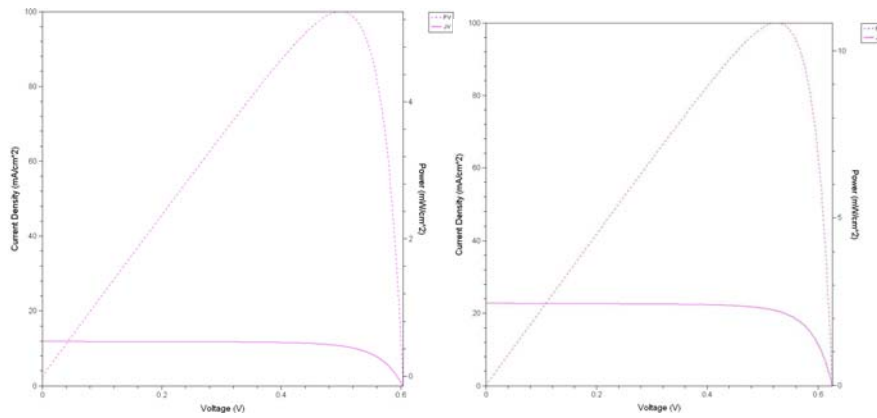


**Figure 4.7:** J-V and P-V curves for the InGaAs cell with truncated (left) and full (right) incident spectrum.

Parameter	Value (truncated spectrum)	Value (full spectrum)
$J_{SC}$	11.81 mA/cm <sup>2</sup>	22.73 mA/cm <sup>2</sup>
$V_{OC}$	0.6028 V	0.626 V
$P_m$	5.32 mW/cm <sup>2</sup>	10.84 mW/cm <sup>2</sup>
FF	74.69%	76.19%
Efficiency	5.32%	10.84%

**Figure 4.8:** Performance metrics for the InGaAs cell. Short circuit current density ( $J_{SC}$ ), open circuit voltage ( $V_{OC}$ ), maximum power ( $P_m$ ), fill factor (FF), and conversion efficiency (Efficiency) are listed. Conversion efficiency values for both the full and truncated spectrum refer to total power converted from the full solar spectrum.

#### 4.1.3 Simulation of a Single Junction Ge Cell

For this simulation Ge was utilized. This material has a band gap of 0.66 eV and a lattice constant of 5.646 angstroms. Material thicknesses and doping levels were varied to achieve the highest efficiency for the junction. A physical diagram and equilibrium band diagram for the device is provided in Figure 4.9. Specific

dimensions and doping concentrations of the highest performing junction are provided in

Parameter	Value
n-Thickness	0.3 $\mu\text{m}$
p-Thickness	1.0 $\mu\text{m}$
n-Concentration	$1\text{e}17 \text{ cm}^{-3}$
p-Concentration	$1\text{e}17 \text{ cm}^{-3}$

**Figure 4.10.** J-V and P-V curves are provided in **Figure 4.11**. Cell performance metrics are provided in

Parameter	Value (truncated spectrum)	Value (full spectrum)
$J_{\text{sc}}$	13.58 $\text{mA}/\text{cm}^2$	22.73 $\text{mA}/\text{cm}^2$
$V_{\text{oc}}$	0.0755 V	0.626 V
$P_{\text{m}}$	0.45 $\text{mW}/\text{cm}^2$	10.84 $\text{mW}/\text{cm}^2$
FF	43.8%	76.19%
Efficiency	0.45%	10.84%

Figure 4.12. In order to get an appropriate response for how this cell would perform as part of a triple junction cell, where part of the incident spectrum would be absorbed by junctions with higher band gaps, simulations were performed with both a full solar spectrum and a truncated spectrum, cutoff at where above cells would stop absorbing light.

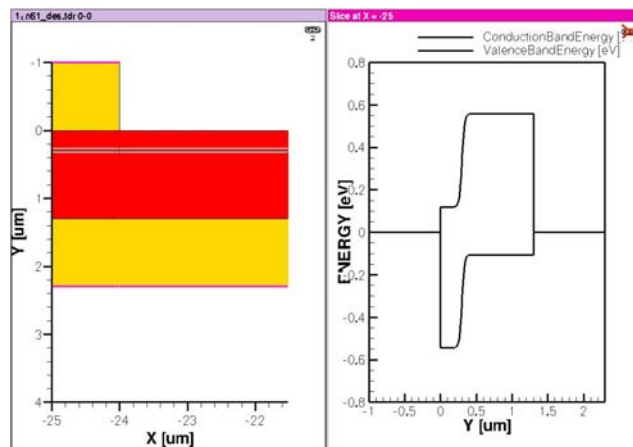


**Figure 4.9:** Physical structure and equilibrium band diagram of a Ge (red) single junction cell.

Parameter	Value
n-Thickness	0.3 $\mu\text{m}$
p-Thickness	1.0 $\mu\text{m}$
n-Concentration	$1\text{e}17 \text{ cm}^{-3}$
p-Concentration	$1\text{e}17 \text{ cm}^{-3}$

**Figure 4.10:** Structural parameters of Ge cell.

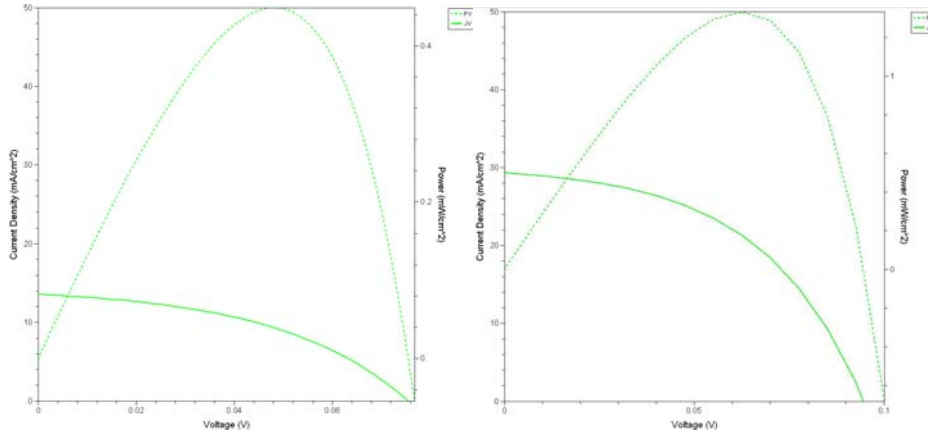


**Figure 4.11:** J-V and P-V curves for the Ge cell with a truncated (left) and full (right) incident spectrum.

Parameter	Value (truncated spectrum)	Value (full spectrum)
$J_{\text{SC}}$	13.58 $\text{mA}/\text{cm}^2$	22.73 $\text{mA}/\text{cm}^2$
$V_{\text{OC}}$	0.0755 V	0.626 V
$P_{\text{m}}$	0.45 $\text{mW}/\text{cm}^2$	10.84 $\text{mW}/\text{cm}^2$
FF	43.8%	76.19%
Efficiency	0.45%	10.84%

**Figure 4.12:** Performance metrics for the Ge cell. Short circuit current density ( $J_{\text{SC}}$ ), open circuit voltage ( $V_{\text{OC}}$ ), maximum power ( $P_{\text{m}}$ ), fill factor (FF), and conversion efficiency (Efficiency) are listed. Conversion efficiency values for both the full and truncated spectrum refer to total power converted from the full solar spectrum.

## 4.2 Simulation of a Tunnel Diode

In this section, a sample tunnel diode is simulated. The diode consists of  $\text{Al}_{0.7}\text{Ga}_{0.3}\text{As}$  and GaAs material layers. A small voltage sweep is performed to

determine when (the?) (each?) diode best conducts. A J-V curve is provided in Figure 4.13.

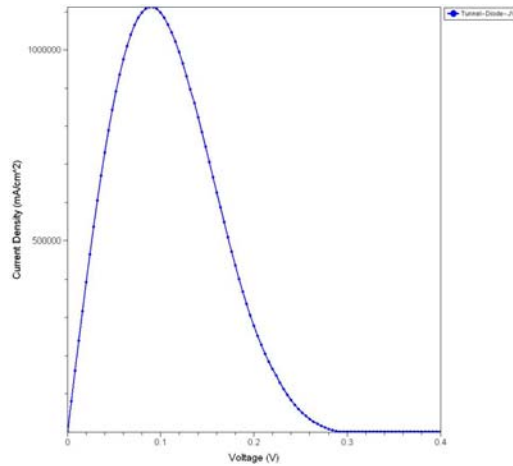


**Figure 4.13:** J-V curve for an Al<sub>0.7</sub>Ga<sub>0.3</sub>As/GaAs tunnel diode.

This simulation of a tunnel diode is not the only composition of tunnel diode used in following simulation. Each combination of adjacent junctions necessitates a tunnel diode with different material compositions, due to band gap and electron affinity considerations. Each tunnel diode operates in a similar manner; the variation of material composition is intended to avoid band edge discontinuity between the tunnel diode and the junction layers and minimize solar absorption by the tunnel diode layers. This section is intended to illustrate the general performance of the tunnel diodes as opposed to listing the performance of all the diodes used for multijunction cells.

#### **4.3 Simulation of Dual Junction Cells**

Simulations of the dual junction cells entail generally the same process as for single junction cells. The main difference lies in the structure tested. Each

structure consists of two p-n junctions in electrical series on either side of a tunnel diode. The tunnel diode is tailored to the materials used in the cell to ensure band edge continuity on both sides of the junction. Gold contacts are then attached on the front and back of the cell.

The goal simulating the dual junction cells is to simulate consecutive junctions of possible triple junction structures. Doing this eases the computational complexity of the structures while still allowing for current matching between consecutive junctions and finding suitable tunnel diode materials. The dual junction structures are then combined into triple junction cells.

#### **4.3.1 Simulation of a GaInP/InGaAs Cell**

In this simulation, the  $\text{Ga}_{0.37}\text{In}_{0.63}\text{P}$  and  $\text{In}_{0.17}\text{Ga}_{0.83}\text{As}$  junctions from Sections 4.1.1 and 4.1.2, respectively, and combined into a single cell. The two cells are connected by an  $\text{In}_{0.7}\text{Al}_{0.3}\text{As}/\text{In}_{0.7}\text{Al}_{0.3}\text{As}$  tunnel diode. A physical diagram and band structure for the device is provided in Figure 4.14. Specific dimensions and doping concentrations for the highest performing cell are provided in Figure 4.15. J-V and P-V curves are provided in Figure 4.16. Cell performance metrics are provided in Figure 4.17.

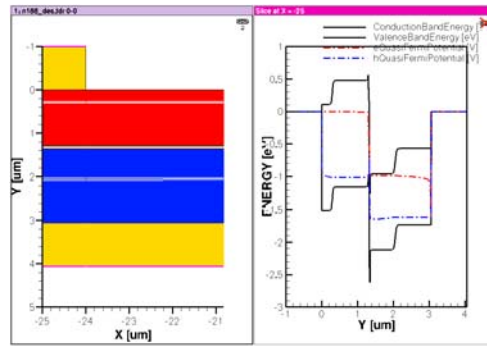


**Figure 4.14:** Physical structure and band diagram of a GaInP(red)/InGaAs(blue) dual junction cell.

Parameter	Value
GaInP n-Thickness	0.3 $\mu\text{m}$
GaInP p-Thickness	1.0 $\mu\text{m}$
GaInP n-Concentration	$1\text{e}17 \text{ cm}^{-3}$
GaInP p-Concentration	$1\text{e}17 \text{ cm}^{-3}$
Tunnel Diode p-Thickness	0.03 $\mu\text{m}$
Tunnel Diode n-Thickness	0.03 $\mu\text{m}$
Tunnel Diode p-Concentration	$1\text{e}19 \text{ cm}^{-3}$
Tunnel Diode n-Concentration	$1\text{e}19 \text{ cm}^{-3}$
InGaAs n-Thickness	0.7 $\mu\text{m}$
InGaAs p-Thickness	1.0 $\mu\text{m}$
InGaAs n-Concentration	$1\text{e}17 \text{ cm}^{-3}$
InGaAs p-Concentration	$1\text{e}17 \text{ cm}^{-3}$

**Figure 4.15:** Structural parameters of GaInP/InGaAs cell.

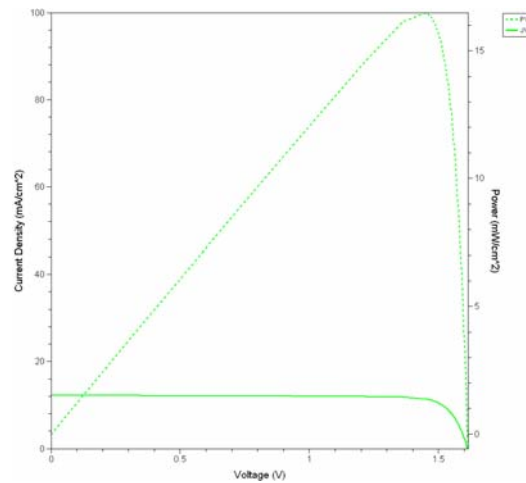


**Figure 4.16:** J-V and P-V curves for the GaInP/InGaAs cell.

Parameter	Value
$J_{SC}$	12.23 mA/cm <sup>2</sup>
$V_{OC}$	1.6041 V
$P_m$	15.14 mW/cm <sup>2</sup>
FF	84.26%
Efficiency	15.14%

**Figure 4.17:** Performance metrics for the GaInP/InGaAs cell. Short circuit current density ( $J_{SC}$ ), open circuit voltage ( $V_{OC}$ ), maximum power ( $P_m$ ), fill factor (FF), and conversion efficiency (Efficiency) are listed.

### 4.3.2 Simulation of an InGaAs/Ge Cell

In this simulation, the  $In_{1.7}Ga_{0.83}As$  and Ge junctions from Sections 4.1.2 and 4.1.3, respectively, and combined into a single cell. The two cells are connected by an  $In_{2.0}Ga_{0.8}As/In_{0.625}Al_{0.325}As$  tunnel diode, with the Gallium bearing side in contact with the InGaAs junction. A physical diagram and band structure for the device is provided in Figure 4.18. Specific dimensions and doping concentrations for the highest performing cell are provided in Figure 4.19. J-V and P-V curves are provided in Figure 4.20. Cell performance metrics are provided in Figure 4.21. Similarly to the single junction cells that are not intended to be the topmost junctions of a multijunction cell, metrics for both full spectrum illumination and a truncated spectrum, truncated where above junctions would absorb incident light, are provided. In order to get an appropriate response for how this cell would perform as part of a triple junction cell, where part of the incident spectrum would be absorbed by junctions with higher band gaps, simulations were performed with both a full solar spectrum and a truncated spectrum, cutoff at where above cells would stop absorbing light.

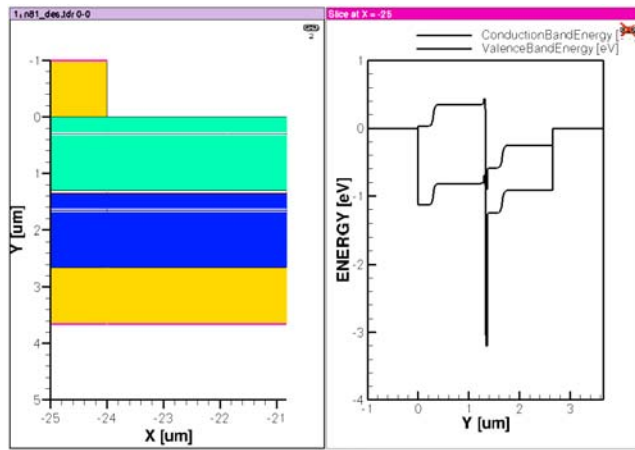


**Figure 4.18:** Physical structure and band diagram of an InGaAs(cyan)/Ge(blue) dual junction cell.

Parameter	Value
InGaAs n-Thickness	0.3 $\mu\text{m}$
InGaAs p-Thickness	1.0 $\mu\text{m}$
InGaAs n-Concentration	$1\text{e}17 \text{ cm}^{-3}$
InGaAs p-Concentration	$1\text{e}17 \text{ cm}^{-3}$
Tunnel Diode p-Thickness	0.03 $\mu\text{m}$
Tunnel Diode n-Thickness	0.03 $\mu\text{m}$
Tunnel Diode p-Concentration	$1\text{e}19 \text{ cm}^{-3}$
Tunnel Diode n-Concentration	$1\text{e}19 \text{ cm}^{-3}$
Ge n-Thickness	0.3 $\mu\text{m}$
Ge p-Thickness	1.0 $\mu\text{m}$
Ge n-Concentration	$1\text{e}17 \text{ cm}^{-3}$
Ge p-Concentration	$1\text{e}17 \text{ cm}^{-3}$

**Figure 4.19:** Structural parameters of InGaAs/Ge cell.

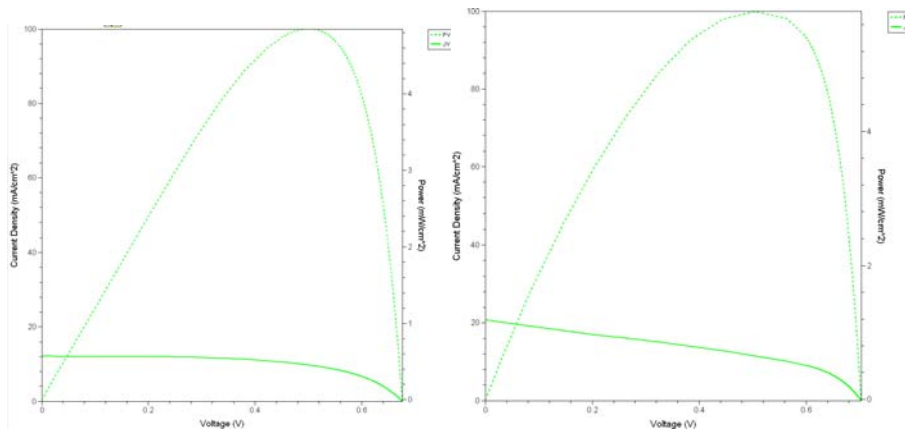


**Figure 4.20:** J-V and P-V curves for the InGaAs/Ge cell with a truncated (left) and full (right) incident spectrum.

Parameter	Value (truncated spectrum)	Value (full spectrum)
$J_{SC}$	12.04 mA/cm <sup>2</sup>	22.73 mA/cm <sup>2</sup>
$V_{OC}$	0.676 V	0.626 V
$P_m$	4.85 mW/cm <sup>2</sup>	10.84 mW/cm <sup>2</sup>
FF	59.60%	76.19%
Efficiency	4.85%	10.84%

**Figure 4.21:** Performance metrics for the InGaAs/Ge cell. Short circuit current density ( $J_{SC}$ ), open circuit voltage ( $V_{OC}$ ), maximum power ( $P_m$ ), fill factor (FF), and conversion efficiency (Efficiency) are listed. Conversion efficiency values for both the full and truncated spectrum refer to total power converted from the full solar spectrum.

It should be noted that this cell has a lower efficiency than the single junction InGaAs cell. However, the performance of this cell is more realistic, as the single junction simulations utilized the full solar spectrum. As the dual junction

#### **4.4 Simulation of Triple Junction Cells**

Simulations of triple junction cells are an extension of the dual junction cell simulations performed previously. In these cells, three p-n junctions are connected in electrical series with a tunnel diode between each pair of p-n junctions. The first of the triple junction cells simulated utilizes information gleaned from the previously described simulations.

Following simulation of this cell, triple junction cells utilizing TI-bearing junctions were simulated. For these cells, a similar simulation procedure was followed. For the sake of brevity, results of single and dual junction cells related to these cells will be omitted. Instead, the results of the final triple junction cell structures will be reported.

#### 4.4.1 Simulation of a GaInP/InGaAs/Ge Cell

For this simulation, a  $\text{Ga}_{0.37}\text{In}_{0.63}\text{P}/\text{In}_{0.17}\text{Ga}_{0.83}\text{As}/\text{Ge}$  cell was tested. This cell is based heavily on the cell described in [121], which has a recorded efficiency of 41.1% under high concentration and of 31.6% efficiency under single sun illumination. This cell is intended to be a baseline against which novel designs incorporating TI-bearing junctions can be compared to. A physical diagram and band structure for the device is provided in Figure 4.22. Specific dimensions and doping concentrations for the highest performing cell are provided in Figure 4.23. J-V and P-V curves are provided in Figure 4.24. Cell performance metrics are provided in

Parameter	Value
$J_{\text{SC}}$	12.25 $\text{mA}/\text{cm}^2$
$V_{\text{OC}}$	1.7081 V
$P_{\text{m}}$	15.53 $\text{mW}/\text{cm}^2$
FF	76.88%
Efficiency	15.53%

Figure 4.25.

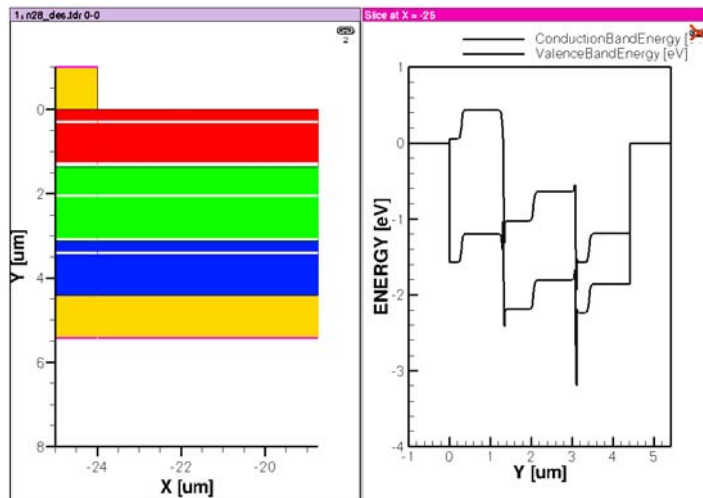


**Figure 4.22:** Physical structure and equilibrium band diagram of a GaInP(red)/InGaAs(green)/Ge(blue) triple junction cell.

Parameter	Value
GaInP n-Thickness	0.3 $\mu\text{m}$
GaInP p-Thickness	1.0 $\mu\text{m}$
GaInP n-Concentration	$1\text{e}17 \text{ cm}^{-3}$
GaInP p-Concentration	$1\text{e}17 \text{ cm}^{-3}$
Tunnel Diode 1 p-Thickness	0.03 $\mu\text{m}$
Tunnel Diode 1 n-Thickness	0.03 $\mu\text{m}$
Tunnel Diode 1 p-Concentration	$1\text{e}19 \text{ cm}^{-3}$
Tunnel Diode 1 n-Concentration	$1\text{e}19 \text{ cm}^{-3}$
InGaAs n-Thickness	0.3 $\mu\text{m}$
InGaAs p-Thickness	1.0 $\mu\text{m}$
InGaAs n-Concentration	$1\text{e}17 \text{ cm}^{-3}$
InGaAs p-Concentration	$1\text{e}17 \text{ cm}^{-3}$
Tunnel Diode 2 p-Thickness	0.03 $\mu\text{m}$
Tunnel Diode 2 n-Thickness	0.03 $\mu\text{m}$
Tunnel Diode 2 p-Concentration	$1\text{e}19 \text{ cm}^{-3}$
Tunnel Diode 2 n-Concentration	$1\text{e}19 \text{ cm}^{-3}$
Ge n-Thickness	0.3 $\mu\text{m}$
Ge p-Thickness	1.0 $\mu\text{m}$
Ge n-Concentration	$1\text{e}17 \text{ cm}^{-3}$
Ge p-Concentration	$1\text{e}17 \text{ cm}^{-3}$

**Figure 4.23:** Structural parameters of GaInP/InGaAs/Ge cell.

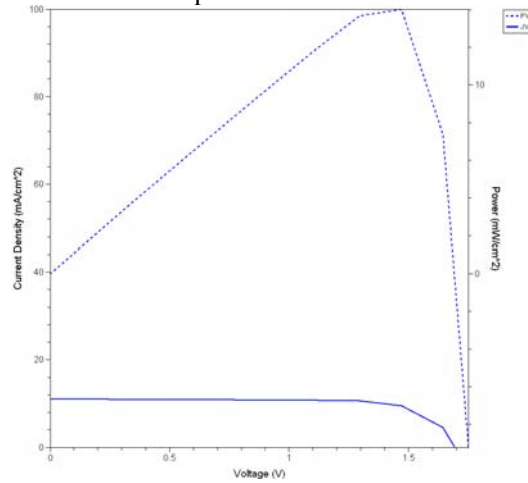


**Figure 4.24:** J-V and P-V curves for the GaInP/InGaAs/Ge cell.

Parameter	Value
$J_{\text{SC}}$	$12.25 \text{ mA/cm}^2$
$V_{\text{OC}}$	1.7081 V
$P_{\text{m}}$	$15.53 \text{ mW/cm}^2$

FF	76.88%
Efficiency	15.53%

**Figure 4.25:** Performance metrics for the GaInP/InGaAs/Ge cell. Short circuit current density ( $J_{SC}$ ), open circuit voltage ( $V_{OC}$ ), maximum power ( $P_m$ ), fill factor (FF), and conversion efficiency (Efficiency) are listed.

#### 4.4.2 Simulation of a GaInP/InGaAs/GaTlP Cell

This cell was designed to directly improve upon the structure from Section 4.4.1. In that cell, the bottom germanium junction has a non-ideal bandgap for use with the top two junctions in the cell. In this case, germanium has a lower than ideal band gap, which implies that the junction will produce sufficient current to match that generated by the above cells, but at the cost of a lower open circuit voltage generated by the junction. This in turn leads to a lower open circuit voltage generated by the cell for the same generated current, leading to reduced power generation and reduced overall efficiency. Germanium was used as the bottom junction material for this cell due to the lack of well defined materials that have band gaps in the ideal range while being lattice-matched to in the 5.6-5.7 angstrom range. Utilizing GaTlP, which has a wider band gap for these lattice constants than germanium, should increase the open circuit voltage of the cell without diminishing the current generated.

For this simulation, a  $Ga_{.37}In_{.63}P/In_{.17}Ga_{.83}As/Ga_{.42}Tl_{.58}P$  cell was tested. This mole fraction of GaTlP has a band gap of 0.9 eV. A physical diagram and band structure for the device is provided in Figure 4.26. Specific dimensions and doping concentrations for the highest performing cell are provided in Figure 4.27. J-V and P-V curves are provided in Figure 4.28. Cell performance metrics are provided in

Parameter	Value
$J_{SC}$	12.36 mA/cm <sup>2</sup>
$V_{OC}$	1.8337 V
$P_m$	17.36 mW/cm <sup>2</sup>
FF	76.61%
Efficiency	17.36%

Figure 4.29.

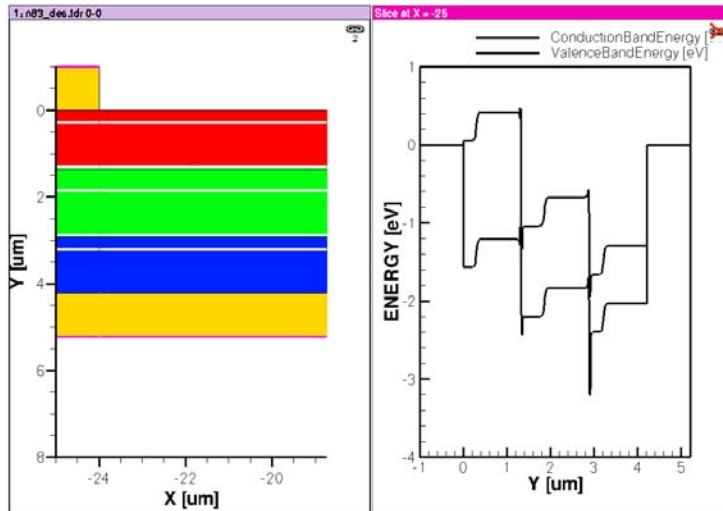


**Figure 4.26:** Physical structure and equilibrium band diagram of a GaInP(red)/InGaAs(green)/GaTIP(blue) triple junction cell.

Parameter	Value
GaInP n-Thickness	0.3 $\mu\text{m}$
GaInP p-Thickness	1.0 $\mu\text{m}$
GaInP n-Concentration	$1\text{e}17 \text{ cm}^{-3}$
GaInP p-Concentration	$1\text{e}17 \text{ cm}^{-3}$
Tunnel Diode 1 p-Thickness	0.03 $\mu\text{m}$
Tunnel Diode 1 n-Thickness	0.03 $\mu\text{m}$
Tunnel Diode 1 p-Concentration	$1\text{e}19 \text{ cm}^{-3}$
Tunnel Diode 1 n-Concentration	$1\text{e}19 \text{ cm}^{-3}$
InGaAs n-Thickness	0.5 $\mu\text{m}$
InGaAs p-Thickness	1.0 $\mu\text{m}$
InGaAs n-Concentration	$1\text{e}17 \text{ cm}^{-3}$
InGaAs p-Concentration	$1\text{e}17 \text{ cm}^{-3}$
Tunnel Diode 2 p-Thickness	0.03 $\mu\text{m}$

Tunnel Diode 2 n-Thickness	0.03 $\mu\text{m}$
Tunnel Diode 2 p-Concentration	$1\text{e}19 \text{ cm}^{-3}$
Tunnel Diode 2 n-Concentration	$1\text{e}19 \text{ cm}^{-3}$
GaTIP n-Thickness	0.3 $\mu\text{m}$
GaTIP p-Thickness	1.0 $\mu\text{m}$
GaTIP n-Concentration	$1\text{e}17 \text{ cm}^{-3}$
GaTIP p-Concentration	$1\text{e}17 \text{ cm}^{-3}$

**Figure 4.27:** Structural parameters of GaInP/InGaAs/GaTIP cell.

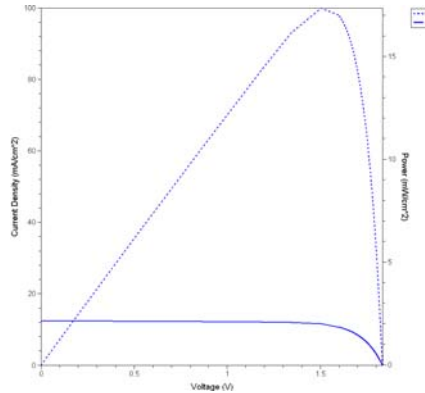


**Figure 4.28:** J-V and P-V curves for the GaInP/InGaAs/GaTIP cell.

Parameter	Value
$J_{SC}$	12.36 $\text{mA}/\text{cm}^2$
$V_{OC}$	1.8337 V
$P_m$	17.36 $\text{mW}/\text{cm}^2$
FF	76.61%
Efficiency	17.36%

**Figure 4.29:** Performance metrics for the GaInP/InGaAs/GaTIP cell. Short circuit current density ( $J_{SC}$ ), open circuit voltage ( $V_{OC}$ ), maximum power ( $P_m$ ), fill factor (FF), and conversion efficiency (Efficiency) are listed.

#### 4.4.3 Simulation of a GaInP/AlGaAs/GaTIP Top Cell

Whereas the previous simulation dealt with improving an existing cell design for a three junction full spectrum cell, this section implemented the band placement suggested in Section 3.2.3.2 for a split junction system. Due to the long-wavelength portion of the solar spectrum redirected to the TPV cell, the amount

of the solar spectrum incident on the PV cell is truncated, leading to higher (in energy) band gap levels for the junctions of the cell.

In this cell, a  $\text{Ga}_{0.76}\text{In}_{0.24}\text{P}/\text{Al}_{0.04}\text{Ga}_{0.96}\text{As}/\text{Ga}_{0.5}\text{Tl}_{0.5}\text{P}$  structure was utilized. These materials have band gaps of 2.00 eV, 1.45 eV, and 0.95 eV, respectively. A physical diagram and band structure for the device is provided in Figure 4.30. Specific dimensions and doping concentrations for the highest performing cell are provided in Figure 4.31. J-V and P-V curves are provided in Figure 4.32. Cell performance metrics are provided in Figure 4.32.

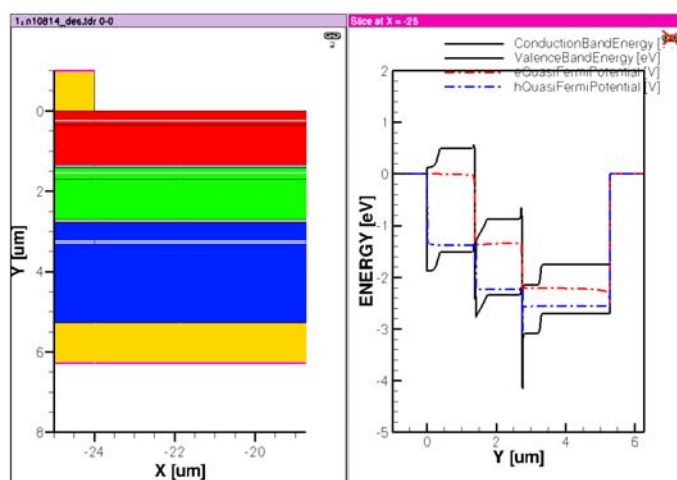


**Figure 4.30:** Physical structure and band diagram of a GaInP(red)/AlGaAs(green)/GaTlP(blue) triple junction cell.

Parameter	Value
GaInP n-Thickness	0.3 $\mu\text{m}$
GaInP p-Thickness	1.0 $\mu\text{m}$
GaInP n-Concentration	$1\text{e}17 \text{ cm}^{-3}$
GaInP p-Concentration	$1\text{e}17 \text{ cm}^{-3}$
Tunnel Diode 1 p-Thickness	0.03 $\mu\text{m}$
Tunnel Diode 1 n-Thickness	0.03 $\mu\text{m}$
Tunnel Diode 1 p-Concentration	$1\text{e}19 \text{ cm}^{-3}$
Tunnel Diode 1 n-Concentration	$1\text{e}19 \text{ cm}^{-3}$
AlGaAs n-Thickness	0.3 $\mu\text{m}$

AlGaAs p-Thickness	1.0 $\mu\text{m}$
AlGaAs n-Concentration	$1\text{e}17 \text{ cm}^{-3}$
AlGaAs p-Concentration	$1\text{e}17 \text{ cm}^{-3}$
Tunnel Diode 2 p-Thickness	0.03 $\mu\text{m}$
Tunnel Diode 2 n-Thickness	0.03 $\mu\text{m}$
Tunnel Diode 2 p-Concentration	$1\text{e}19 \text{ cm}^{-3}$
Tunnel Diode 2 n-Concentration	$1\text{e}19 \text{ cm}^{-3}$
GaTIP n-Thickness	0.3 $\mu\text{m}$
GaTIP p-Thickness	1.0 $\mu\text{m}$
GaTIP n-Concentration	$1\text{e}17 \text{ cm}^{-3}$
GaTIP p-Concentration	$1\text{e}17 \text{ cm}^{-3}$

**Figure 4.31:** Structural parameters of GaInP/AlGaAs/GaTIP cell.

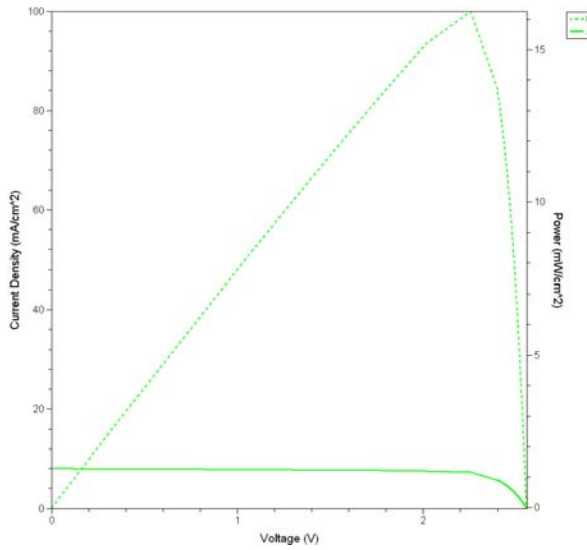


**Figure 4.32:** J-V and P-V curves for the GaInP/AlGaAs/GaTIP cell.

Parameter	Value
$J_{SC}$	7.96 $\text{mA}/\text{cm}^2$
$V_{OC}$	2.556 V
$P_m$	16.26 $\text{mW}/\text{cm}^2$
FF	79.92%
Efficiency	16.26%

**Figure 4.33:** Performance metrics for the GaInP/AlGaAs/GaTIP cell. Short circuit current density ( $J_{SC}$ ), open circuit voltage ( $V_{OC}$ ), maximum power ( $P_m$ ), fill factor (FF), and conversion efficiency (Efficiency) are listed.

#### 4.4.4 Simulation of GaSb TPV Cell

For the purposes of calculating the system efficiency for a SJ system, a simple TPV cell was simulated. Simulated was a single junction GaSb cell, with a 0.726 eV. As this cell is intended for use in a split junction system, simulations are provided for both full spectrum and for an incident spectrum corresponding to where a dichroic mirror would split the solar spectrum, in this case at 0.95 eV. A physical diagram and band structure for the device is provided in Figure 4.34. Specific dimensions and doping concentrations for the highest performing cell are provided in Figure 4.35. J-V and P-V curves are provided in Figure 4.36. Cell performance metrics are provided in

Parameter	Value (truncated spectrum)	Value (full spectrum)
$J_{SC}$	9.80 mA/cm <sup>2</sup>	35.99 mA/cm <sup>2</sup>
$V_{OC}$	0.1485 V	0.1951 V
$P_m$	0.71 mW/cm <sup>2</sup>	3.89 mW/cm <sup>2</sup>
FF	48.66%	55.43%
Efficiency	0.71%	3.89%

Figure 4.37.

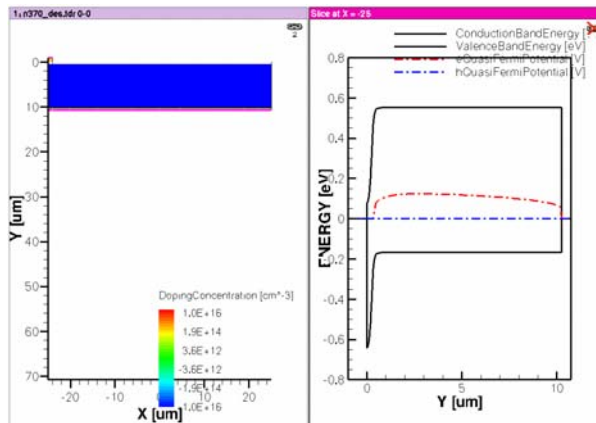
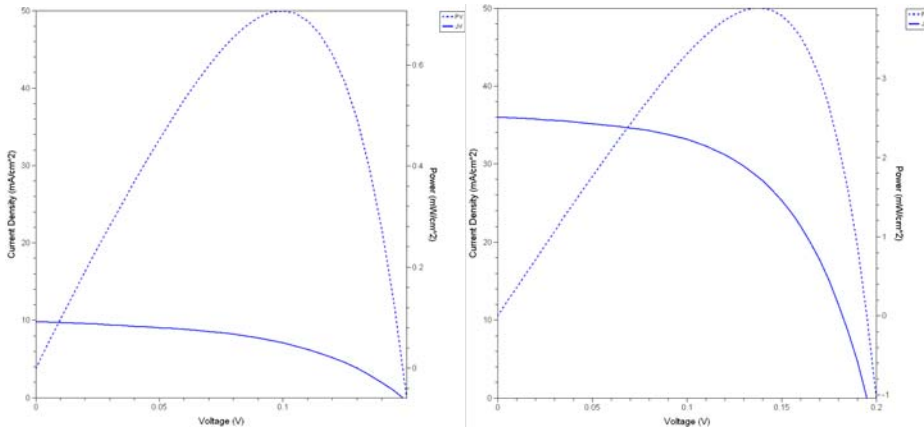


Figure 4.34: Physical structure and equilibrium band diagram of a GaSb single junction cell.

Parameter	Value
n-Thickness	0.25 $\mu\text{m}$
p-Thickness	10 $\mu\text{m}$
n-Concentration	$1\text{e}16 \text{ cm}^{-3}$
p-Concentration	$1\text{e}16 \text{ cm}^{-3}$

**Figure 4.35:** Structural parameters of GaSb cell.



**Figure 4.36:** J-V and P-V curves for the GaSb cell with truncated (left) and full (right) spectrum illumination.

Parameter	Value (truncated spectrum)	Value (full spectrum)
$J_{SC}$	9.80 $\text{mA}/\text{cm}^2$	35.99 $\text{mA}/\text{cm}^2$
$V_{OC}$	0.1485 V	0.1951 V
$P_m$	0.71 $\text{mW}/\text{cm}^2$	3.89 $\text{mW}/\text{cm}^2$
FF	48.66%	55.43%
Efficiency	0.71%	3.89%

**Figure 4.37:** Performance metrics for the GaSb cell. Short circuit current density ( $J_{SC}$ ), open circuit voltage ( $V_{OC}$ ), maximum power ( $P_m$ ), current at maximum power ( $I_m$ ), voltage at maximum power ( $V_m$ ), fill factor (FF), and conversion efficiency (Efficiency) are listed.

To determine the total system efficiency of the SJ system, the conversion efficiency of this TPV cell is added to the PV cell from Section 4.4.3, resulting in a total system efficiency of 16.97%.

#### 4.4.5 Simulations of Triple Junction Cells Utilizing Antireflective Coatings

Both the PV and TPV cells under discussion to this point would be best described as stripped down versions of solar cells. Fabricated solar cells include a number of other features to ensure higher conversion efficiencies. Some of those features, like use of ohmic contacts, can be omitted due to the idealized nature of simulation work. Other features, like antireflective coatings (ARCs), can be included to improve simulation efficiencies.

Most of the semiconductor materials used in solar cells have indices of refraction in range of 3-4.5, depending on both material and specific wavelength of light. This differs greatly from index of refraction of air,  $\sim 1$ . Using Equation 1.1 :

$$R = \left( \frac{n_1 - n_2}{n_1 + n_2} \right)^2 \quad 4.1$$

it is calculated that at the interface between air and the semiconductor materials as much as 40.5% of incident light is reflected from cell, indicating a massive loss in efficiency. If a material, or materials with a wider band gap than any junction in the cell (to minimize absorption of light by this layer that could be absorbed by the active regions of the cell) but an intermediate index of refraction, the amount of reflected light can be reduced.

In this section a  $\text{Si}_3\text{N}_4$  layer, with an average index of refraction of around 2.74, is added on top of each of the triple junction cells previously simulated. Using the equation above, it is calculated that using this intermediate layer can reduce reflection from the range of 22.0-26.6%. Efficiency metrics for the new cells are then calculated. Additionally, the external quantum efficiency of each

cell across a range of wavelengths is calculated before and after adding the antireflective coating to show that the layer aids in light absorption across all wavelengths of light. The results of these simulations can be seen in Figures 4.38-42.

Parameter	Value
$J_{SC}$	13.91 mA/cm <sup>2</sup>
$V_{OC}$	1.7286 V
$P_m$	17.90 mW/cm <sup>2</sup>
FF	74.43%
Efficiency	17.9%

**Figure 4.38:** Performance metrics for the GaInP/InGaAs/Ge cell with a Si<sub>3</sub>N<sub>4</sub> ARC. Short circuit current density ( $J_{SC}$ ), open circuit voltage ( $V_{OC}$ ), maximum power ( $P_m$ ), fill factor (FF), and conversion efficiency (Efficiency) are listed.

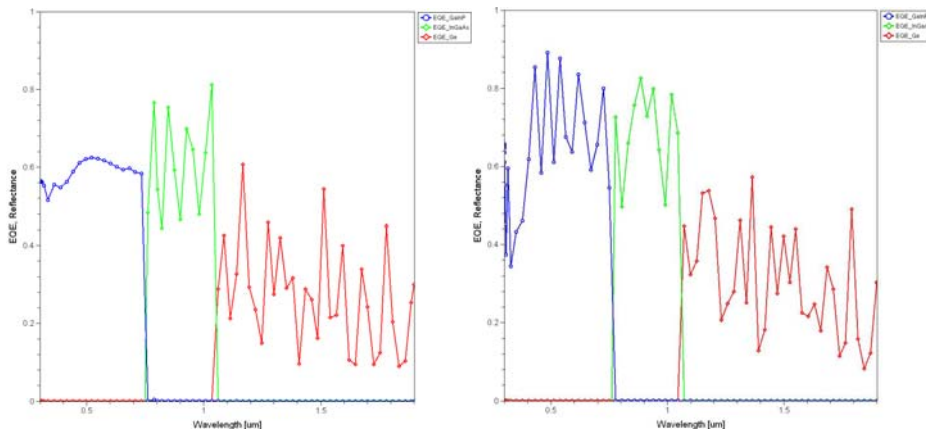


**Figure 4.39:** EQE of GaInP/InGaAs/Ge cell without (left) and with (right) a Si<sub>3</sub>N<sub>4</sub> ARC.

Parameter	Value
$J_{SC}$	13.95 mA/cm <sup>2</sup>
$V_{OC}$	1.8507 V
$P_m$	19.74 mW/cm <sup>2</sup>
FF	76.43%
Efficiency	19.74%

**Figure 4.40:** Performance metrics for the GaInP/InGaAs/GaTIP cell with a Si<sub>3</sub>N<sub>4</sub> ARC. Short circuit current density ( $J_{SC}$ ), open circuit voltage ( $V_{OC}$ ), maximum power ( $P_m$ ), fill factor (FF), and conversion efficiency (Efficiency) are listed.

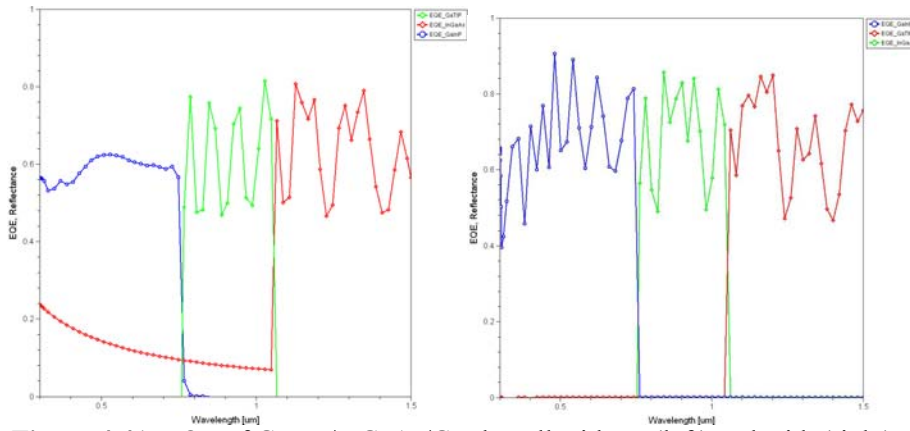


**Figure 4.41:** EQE of GaInP/InGaAs/GaTIP cell without (left) and with (right) a Si<sub>3</sub>N<sub>4</sub> ARC.

Parameter	Value
J <sub>SC</sub>	9.95 mA/cm <sup>2</sup>
V <sub>OC</sub>	2.5787 V
P <sub>m</sub>	20.32 mW/cm <sup>2</sup>
FF	79.21%
Efficiency	20.32%

**Figure 4.42:** Performance metrics for the GaInP/AlGaAs/GaTIP cell with a Si<sub>3</sub>N<sub>4</sub> ARC. Short circuit current density (J<sub>SC</sub>), open circuit voltage (V<sub>OC</sub>), maximum power (P<sub>m</sub>), fill factor (FF), and conversion efficiency (Efficiency) are listed.

#### **4.5 Conclusions and Future Work**

Use of the GaTIP in resulted in higher simulated conversion efficiencies when under the same conditions than some of the most efficient cells produced to date, resulting in an improvement over that cell of 2.42% for a 3-junction full spectrum cell and 3.13% for a split junction system. Utilization of a simple 1-layer ARC dramatically improved the current density generated by the cells 12.9% for the full spectrum cell and 25.0% for split junction cell, but external quantum efficiency simulations show that there is still a significant portion of incident light lost to reflection. In order to get to the current densities expected from these cells,

$\sim 16 \text{ mA/cm}^2$ , more extensive ARCs must be used, utilizing 2 or more layers with intermediate indices of refraction, which will be a focus of future simulations.

Perhaps the largest deviation from the results expected from literature is in open circuit voltage of these cells. For example, the GaInP/InGaAs/Ge cell taken from literature has an experimental  $V_{oc}$  of 2.282 V, whereas the simulated structure only resulted in a  $V_{oc}$  of 1.7286 V [121]. Further investigation into this issue revealed that the simulation software consistently underestimates the open circuit voltages of individual solar cell junctions, usually on the order of 0.2 V. This effect was evidenced by comparing single junction cells from published works and simulating the exact same structures, from layer thicknesses to doping levels. Investigating a germanium subcell, specified in [122], the expected  $V_{oc}$  for a cell should be in the range of 0.25-0.32 V, depending on doping levels and layer thicknesses. However, the highest  $V_{oc}$  achieved in simulation was 0.08 V. For a GaAs subcell, specified in [123] the open circuit voltage should reach somewhere in the range of 1.00-1.05 V, but the highest ever achieved in simulation utilizing this structure was 0.85 V. This shows a systematic error in simulations across all materials. This effect is cumulative when numerous junctions are utilized in a single cell. In the case of a triple junction cell, this can result in a discrepancy of up to 0.6 V, equal to that between experimental and simulated results. The cause of this discrepancy will be the focus of future inquiry, but as this irregularity is consistent across all of the cells simulated, it is believed that the main result from the simulation is still valid, that use of GaTIP in multijunction and split junction systems can result in higher conversion efficiencies. Future work will include

fabrication of cells including (Ti)-bearing materials, attempting to generate higher conversion efficiencies than currently demonstrated.

## Chapter 5 Conclusion and Future Work

In Chapter 3, the ideal band placements for both full spectrum and split junction systems were examined. For the full spectrum case, the ideal band placement was compared to that of structures that have been designed previously. The most relevant result from this section was in regard to previously used triple junction cells. Due to the common usage of germanium bottom junctions, there is significant excess current generated by this junction, current which is wasted due to the current generation limitations by the other junctions. This implies that the band gap for this junction was too low, which in turn resulted in a lower open circuit voltage for the cell as a whole. There were (are?) no well-characterized materials that had both the required band gap and lattice constant, but it was determined that a novel material of interest, GaTIP, could fill this need. Triple junction full spectrum cells utilizing this material were further examined in Chapter 4.

For split junction systems, the cutoff wavelength between the two stages was varied and then the ideal band placements for both stages were determined. Once these were found, it was determined if there was any combination of materials that satisfied both the band placements desired while maintaining lattice-matching throughout the cells of each stage existed. Such combinations exist for two of the examined cutoff wavelengths: 867 nm and 1100 nm.

For the 867 nm cutoff system, there existed combinations of materials that were well-characterized for both the PV and TPV stage. Since these stages did not necessitate use of the novel materials under investigation for this thesis,

further analysis of these cells was deferred to a later date. Specifically, due to the relatively short cutoff wavelength of the filter for this system, further analysis of the TPV stage, dividing that portion of the spectrum across more than the two junction upper limit assumed for this thesis and possibly even multiple stages, should be investigated. Fabrication of these cells may also warrant investigation.

For the 1100 nm cutoff system, a viable material combination was present. This combination required the use of GaTIP, a material mentioned previously for the triple junction full spectrum cell, for the PV stage. Further examination of this system was performed in Chapter 4.

In Chapter 4, simulations were performed on full spectrum cells and split junction systems which utilize GaTIP junctions to determine if use of this material could improve overall conversion efficiency. These simulations can be divided into two general cases: a comparison of full spectrum triple junction cells, one with a germanium bottom junction and the other a GaTIP bottom junction, and examination of a split junction system whose PV stage utilizes a GaTIP bottom junction. In the former example, it was determined that incorporation of GaTIP in the cell can improve the open circuit and operating voltages of the cell with negatively influencing the current generated, resulting in a net improvement in conversion efficiency. In the latter, it was determined that the system conversion efficiency could exceed that. Both of these designs now require fabrication and testing. This will require a great amount of effort, as compositions of GaTIP with the required thallium content required for this application have not been grown to date, much less incorporated into complicated structures. In fact, compositions

with even a fraction of the required thallium have resulted in unusable film quality.

## Appendix – Figure Credits

### Chapter 1

**Figure 1.1:** Reference [1]  
**Figure 1.2:** Reference [2]  
**Figure 1.3:** Reference [3]  
**Figure 1.4:** Reference [4]  
**Figure 1.5:** Reference [3]  
**Figure 1.6:** Reference [4]  
**Figure 1.7:** Reference [5]  
**Figure 1.8:** Created by Chandler Downs  
**Figure 1.9:** Reference [4]  
**Figure 1.10:** Reference [5]  
**Figure 1.11:** Created by Chandler Downs  
**Figure 1.12:** Reference [6]  
**Figure 1.13:** Reference [7]  
**Figure 1.14:** Reference [7]  
**Figure 1.15:** Created by Chandler Downs  
**Figure 1.16:** Reference [8]  
**Figure 1.17:** Created by Chandler Downs  
**Figure 1.18:** Created by Chandler Downs  
**Figure 1.19:** Created by Chandler Downs  
**Figure 1.20:** Reference [9]  
**Figure 1.21:** Reference [10]  
**Figure 1.22:** Reference [11]  
**Figure 1.23:** Reference [12]  
**Figure 1.24:** Reference [13]  
**Figure 1.25:** Reference [14]  
**Figure 1.26:** Reference [14]  
**Figure 1.27:** Reference [15]  
**Figure 1.28:** Reference [16]  
**Figure 1.29:** Reference [17]  
**Figure 1.30:** Reference [4]  
**Figure 1.31:** Reference [15]  
**Figure 1.32:** Reference [18]  
**Figure 1.33:** Reference [19]  
**Figure 1.34:** Reference [20]  
**Figure 1.35:** Reference [21]  
**Figure 1.36:** Reference [22]  
**Figure 1.37:** Reference [23]  
**Figure 1.38:** Created by Chandler Downs  
**Figure 1.39:** Created by Chandler Downs  
**Figure 1.40:** Reference [24]  
**Figure 1.41:** Created by Chandler Downs  
**Figure 1.42:** Created by Chandler Downs  
**Figure 1.43:** Reference [25]

## **Chapter 2**

**Figure 2.1:** Created by Chandler Downs  
**Figure 2.2:** Created by Chandler Downs  
**Figure 2.3:** Created by Chandler Downs  
**Figure 2.4:** Created by Chandler Downs  
**Figure 2.5:** Created by Chandler Downs  
**Figure 2.6:** Created by Chandler Downs  
**Figure 2.7:** Created by Chandler Downs  
**Figure 2.8:** Created by Chandler Downs  
**Figure 2.9:** Created by Chandler Downs  
**Figure 2.10:** Created by Chandler Downs  
**Figure 2.11:** Reference [26]

## **Chapter 3**

**Figure 3.1:** Created by Chandler Downs using reference [21]  
**Figure 3.2:** Created by Chandler Downs using reference [21]  
**Figure 3.3:** Created by Chandler Downs using reference [21]  
**Figure 3.4:** Created by Chandler Downs  
**Figure 3.5:** Created by Chandler Downs  
**Figure 3.6:** Created by Chandler Downs  
**Figure 3.7:** Created by Chandler Downs  
**Figure 3.8:** Created by Chandler Downs adapted from [27]  
**Figure 3.9:** Created by Chandler Downs  
**Figure 3.10:** Created by Chandler Downs  
**Figure 3.11:** Created by Chandler Downs  
**Figure 3.12:** Created by Chandler Downs  
**Figure 3.13:** Created by Chandler Downs

## **Chapter 4**

**Figure 4.1:** Created by Chandler Downs  
**Figure 4.2:** Created by Chandler Downs  
**Figure 4.3:** Created by Chandler Downs  
**Figure 4.4:** Created by Chandler Downs  
**Figure 4.5:** Created by Chandler Downs  
**Figure 4.6:** Created by Chandler Downs  
**Figure 4.7:** Created by Chandler Downs  
**Figure 4.8:** Created by Chandler Downs  
**Figure 4.9:** Created by Chandler Downs  
**Figure 4.10:** Created by Chandler Downs  
**Figure 4.11:** Created by Chandler Downs  
**Figure 4.12:** Created by Chandler Downs  
**Figure 4.13:** Created by Chandler Downs  
**Figure 4.14:** Created by Chandler Downs  
**Figure 4.15:** Created by Chandler Downs  
**Figure 4.16:** Created by Chandler Downs  
**Figure 4.17:** Created by Chandler Downs

**Figure 4.18:** Created by Chandler Downs  
**Figure 4.19:** Created by Chandler Downs  
**Figure 4.20:** Created by Chandler Downs  
**Figure 4.21:** Created by Chandler Downs  
**Figure 4.22:** Created by Chandler Downs  
**Figure 4.23:** Created by Chandler Downs  
**Figure 4.24:** Created by Chandler Downs  
**Figure 4.25:** Created by Chandler Downs  
**Figure 4.26:** Created by Chandler Downs  
**Figure 4.27:** Created by Chandler Downs  
**Figure 4.28:** Created by Chandler Downs  
**Figure 4.29:** Created by Chandler Downs  
**Figure 4.30:** Created by Chandler Downs  
**Figure 4.31:** Created by Chandler Downs  
**Figure 4.32:** Created by Chandler Downs  
**Figure 4.33:** Created by Chandler Downs  
**Figure 4.34:** Created by Chandler Downs  
**Figure 4.35:** Created by Chandler Downs  
**Figure 4.36:** Created by Chandler Downs  
**Figure 4.37:** Created by Chandler Downs  
**Figure 4.38:** Created by Chandler Downs  
**Figure 4.39:** Created by Chandler Downs  
**Figure 4.40:** Created by Chandler Downs  
**Figure 4.41:** Created by Chandler Downs  
**Figure 4.42:** Created by Chandler Downs

## Bibliography

1. Lawrence Kazmerski, D.G., Al Kicks, *Best Research-Cell Efficiencies*. 2007.
2. *ASTM G173-03 Reference Spectra*.
3. Kasap, S.O., *Optoelectronics and Photonics: Principles and Practices*. 2001, Upper Saddle River: Prentice Hall.
4. Saleh, B.E., *Fundamentals of Photonics*. 2007: Wiley-Interscience.
5. Manasreh, O., *Semiconductor Heterojunctions and Nanostructures*. 2005, New York: McGraw-Hill.
6. Neamen, D.A., *Semiconductor Physics and Devices*. 2003, Boston: McGraw-Hill.
7. Anderson, B.L., et al., *Fundamentals of Semiconductor Devices*. 2005, Boston: McGraw Hill.
8. Nahory, R.E., et al., *Band gap versus composition and demonstration of Vegard's Law for  $In_{1-x}Ga_xAs_yP_{1-y}$  lattice matched to InP*. Applied Physics Letters, 1978. **33**(7): p. 659-61.
9. Goetzberger, A., et al., *Photovoltaic materials, history, status and outlook*. Materials Science & Engineering R: Reports, 2003. **40**(1): p. 1-46.
10. Staebler, D.L., et al., *Reversible conductivity change in discharge-produced amorphous Si*. Applied Physics Letters, 1977. **31**(4): p. 292-4.
11. Gratzel, M., *Dye-sensitized solar cells*. Journal of Photochemistry and Photobiology C: Photochemistry Reviews, 2003. **4**(2): p. 145-53.
12. Hoppe, H., et al., *Organic solar cells: An overview*. Journal of Materials Research, 2004. **19**(7): p. 1924-45.
13. Strumpel, C.e.a., *Modifying the solar spectrum to enhance silicon solar cell efficiency - An overview of available materials*. Solar Energy Materials and Solar Cells, 2007. **91**(4): p. 238-49.
14. Trupke, T., et al., *Improving solar cell efficiencies by down-conversion of high-energy photons*. Journal of Applied Physics, 2002. **92**(3): p. 1668-74.
15. Sun, B., et al., *Photovoltaic Devices Using Blends of Branched Cdse Nanoparticles and Conjugated Polymers*. Nano Letters, 2003. **3**(7): p. 961-63.
16. Pan, J.L. and C.G. Fonstad, *Theory, fabrication and characterization of quantum well infrared photodetectors*. Materials Science and Engineering: R: Reports, 2000. **28**(3-4): p. 65-147.
17. Barnham, K.W.J., et al., *Quantum well solar cells*. Physica E: Low-dimensional Systems and Nanostructures, 2002. **14**(1-2): p. 27-36.
18. Bhattacharya, P., S. Ghosh, and A.D. Stiff-Roberts, *QUANTUM DOT OPTO-ELECTRONIC DEVICES*. Annual Review of Materials Research, 2004. **34**(1): p. 1-40.
19. Nishi, K., et al., *A narrow photoluminescence linewidth of 21 meV at 1.35  $\mu$  m from strain-reduced InAs quantum dots covered by  $In_{0.2}Ga_{0.8}As$  grown on GaAs substrates*. Applied Physics Letters, 1999. **74**(8): p. 1111-1113.

20. Algora, C., *Key aspects in the modeling of concentrator III-V solar cells and III-V thermophotovoltaic converters*. Semiconductors, 2004. **38**(8): p. 918-922.
21. Zdanowicz, T., T. Rodziewicz, and M. Zabkowska-Waclawek, *Theoretical analysis of the optimum energy band gap of semiconductors for fabrication of solar cells for applications in higher latitudes locations*. Solar Energy Materials and Solar Cells, 2005. **87**(1-4): p. 757-769.
22. King, R.R., *High-efficiency multijunction photovoltaics for low-cost solar electricity*. LEOS 2008 - 21st Annual Meeting of the IEEE Lasers and Electro-Optics Society 2008: p. 2-3.
23. IMPhotonix, I., *Dichroic Filter Specifications*. 2010: Tewksbury.
24. Jonscher, A.K., et al., *The Physics of the Tunnel Diode*. British Journal of Applied Physics, 1961. **12**: p. 654.
25. Nelson, L., *The Physics of Solar Cells*. 2003, London: Imperial College Press.
26. Shemelya, C., *A Thermophotovoltaic Enhancement: 2D Photonic Crystals to Increase Thermophotovoltaic Efficiencies*, in *Electrical and Computer Engineering*. 2010, Tufts University: Medford.
27. [http://www.tf.uni-kiel.de/matwis/amat/semi\\_en/kap\\_5/backbone/r5\\_1\\_4.html](http://www.tf.uni-kiel.de/matwis/amat/semi_en/kap_5/backbone/r5_1_4.html), *Lattice Constant vs. Band Gap plot*, bandgap\_misfit.gif, Editor.
28. *Renewable Energy Consumption and Electricity Preliminary Statistics 2008*. 2009, Energy Information Administration: Washington, DC.
29. *Total Primary energy Consumption (Quadrillion Btu), All Countries*. 2006, US Energy Information Administration: Washington, DC.
30. Da Rosa, A.V., *Fundamentals of Renewable Energy*. 2005: Elsevier Academic Press.
31. Lorenz, P., et al., *The economics of solar power*, in *The McKinsey Quarterly*. 2008, McKinsey & Company.
32. *Solar Cell*, in *Encyclopaedia Britannica*. 2010, Encyclopaedia Britannica Online.
33. Chapin, D.M., et. al, *A new silicon p-n junction photocell for converting solar radiation into electrical power*. Journal of Applied Physics, 1954. **25**: p. 676-7.
34. Zahl, H.A. and H.K. Ziegler, *Power sources for satellites and space vehicles*. Solar Energy, 1960. **4**(1): p. 32-38.
35. Green, M.A., et al., *Solar Cell Efficiency Tables (Version 32)*. Progress in Photovoltaics: Research and Applications, 2008. **16**: p. 435-40.
36. *Photovoltaic Effect*, in *Encyclopaedia Britannica*. 2010, Encyclopaedia Britannica Online.
37. Kasap, S.O., *Electronic Materials and Devices*. 2006: McGraw-Hill.
38. Stern, F. and J.M. Woodall, *Photon recycling in semiconductor lasers*. Journal of Applied Physics, 1974. **45**(9): p. 3904-3906.
39. Kazmerski, L.I., *Photovoltaics: a review of cell and module technologies*. Renewable & Sustainable Energy Reviews, 1997. **1**(1-2): p. 71-170.

40. Afzaal, M., et al., *Recent developments in II-VI and III-V semiconductors and their applications in solar cells*. Journal of Materials Chemistry, 2005. **16**: p. 1597-602.
41. Chu, T.L. and S.S. Chu, *Thin film II-VI photovoltaics*. Solid-State Electronics, 1995. **38**(3): p. 533-549.
42. Bachmann, K.J., et al., *II-VI and I-III-VI<sub>2</sub> alloy crystals for photovoltaic applications*. Solar Cells. **21**(1-4): p. 99-108.
43. Vurgaftman, I., et al., *Band Parameters for III-V compound semiconductors and their alloys*. Journal of Applied Physics, 2001. **89**(11).
44. Onda, T. and R. Ito, *Behavior of miscibility gaps in the phase diagrams of III-V semiconductor : I. Ternary systems solid solutions*. Journal of Crystal Growth, 1986. **78**(3): p. 479-492.
45. Bhattacharya, P., *Semiconductor Optoelectronic Devices*. 1997: Prentice Hall.
46. Zolper, J.C., *The effect of dislocations on the performance of gallium arsenide solar cells*. Conference Record of the Twentieth IEEE Photovoltaic Specialists Conference, 1988. **1**: p. 678-83.
47. Kieliba, T., S. Riepe, and W. Warta, *Effect of dislocations on minority carrier diffusion length in practical silicon solar cells*. Journal of Applied Physics, 2006. **100**(6): p. 063706-12.
48. Jain, R.K., et al., *Influence of the dislocation density on the performance of heteroepitaxial indium phosphide solar cells*. IEEE Transactions on Electron Devices, 1993. **40**(11): p. 1928-34.
49. Vernon, S.M., et al., *Experimental study of solar cell performance versus dislocation density*. Conference Record of the Twenty First IEEE Photovoltaic Specialists Conference, 1990. **1**: p. 211-6.
50. Shockley, W., et al., *Statistics of recombinations of holes and electrons*. Physical Review, 1952. **87**(5): p. 823-42.
51. Wenham, S.R. and M.A. Green, *Silicon solar cells*. Progress in Photovoltaics: Research and Applications, 1996. **4**(1): p. 3-33.
52. Rothwarf, A. and K.W. Böer, *Direct conversion of solar energy through photovoltaic cells*. Progress in Solid State Chemistry, 1975. **10**(Part 2): p. 71-102.
53. Goetzberger, A. and C. Hebling, *Photovoltaic materials, past, present, future*. Solar Energy Materials and Solar Cells, 2000. **62**(1-2): p. 1-19.
54. Rech, B. and H. Wagner, *Potential of amorphous silicon for solar cells*. Applied Physics A: Materials Science & Processing, 1999. **69**(2): p. 155-167.
55. Hamakawa, Y., *Recent advances in amorphous silicon technologies and its application to solar cells*. Renewable Energy. **8**(1-4): p. 10-16.
56. Bolton, J.R., *Solar Cells - A Technology Assessment*. Solar Energy Materials and Solar Cells, 1983. **31**(5): p. 483-502.
57. Meier, J., et al., *Potential of amorphous and microcrystalline silicon solar cells*. Thin Solid Films, 2004. **451-452**: p. 518-524.

58. O'Regan, B., Gratzel, M., *A low-cost, high-efficiency solar cell based on dye-sensitized colloidal TiO<sub>2</sub> films*. Nature, 1991. **353**(6346): p. 737-40.
59. Chiba, Y., et al., *Conversion efficiency of 10.8% by a dye-sensitized solar cell using a TiO<sub>2</sub> electrode with high haze*. Applied Physics Letters, 2006. **88**(22).
60. Goncalves, L.M., et al., *Dye-sensitized solar cells: A safe bet for the future*. Energy & Environmental Science, 2008. **1**: p. 655-67.
61. Patrocinio, A.O.T., et al., *Efficient and low cost devices for solar energy conversion: Efficiency and stability of some natural-dye-sensitized solar cells*. Synthetic Metals, 2009. **159**(21-22): p. 2342-2344.
62. McConnell, R.D., *Assessment of the dye-sensitized solar cell*. Renewable and Sustainable Energy Reviews, 2002. **6**(3): p. 271-293.
63. Green, M.A., et al., *Solar cell efficiency tables (Version 34)*. Progress in Photovoltaics: Research and Applications, 2009. **17**(5): p. 320-326.
64. Usami, A., et al., *Temperature dependence of open-circuit voltage in dye-sensitized solar cells*. Solar Energy Materials and Solar Cells, 2009. **93**(6-7): p. 840-842.
65. Ghosh, A.K., et al., *Photovoltaic and rectification properties of Al/Mg phthalocyanine/Al Schottky-barrier cells*. Journal of Applied Physics, 1974. **45**(1): p. 230-6.
66. Tang, C.W., *Two-layer organic photovoltaic cell*. Applied Physics Letters, 1986. **48**(2): p. 183-185.
67. Benanti, T. and D. Venkataraman, *Organic Solar Cells: An Overview Focusing on Active Layer Morphology*. Photosynthesis Research, 2006. **87**(1): p. 73-81.
68. Stubinger, T. and W. Brutting, *Exciton diffusion and optical interference in organic donor--acceptor photovoltaic cells*. Journal of Applied Physics, 2001. **90**(7): p. 3632-3641.
69. Hauch, J.A., et al., *Flexible organic P3HT:PCBM bulk-heterojunction modules with more than 1 year outdoor lifetime*. Solar Energy Materials and Solar Cells, 2008. **92**(7): p. 727-31.
70. Auzel, F., *Upconversion and Anti-Stokes Processes with f and d Ions in Solids*. Chemical Reviews, 2004. **104**(1): p. 139-73.
71. Ahrens, B., et al., *Neodymium-doped fluorochlorozirconate glasses as an upconversion model system for high efficiency solar cells*. physica status solidi (a), 2008. **205**(12): p. 2822-2830.
72. Goldschmidt, J.C., et al., *Advanced upconverter systems with spectral and geometric concentration for high upconversion efficiencies*. Proceedings of the 2008 Conference on Optoelectronic and Microelectronic Materials and Devices, COMMAD '08, 2008: p. 307-11.
73. Shalav, A., B.S. Richards, and M.A. Green, *Luminescent layers for enhanced silicon solar cell performance: Up-conversion*. Solar Energy Materials and Solar Cells, 2007. **91**(9): p. 829-842.
74. Luque, A., et al., *Multiple Levels in Intermediate Band Solar Cells*. Applied Physics Letters, 2010. **96**(1).

75. Shpaisman, H., et al., *Can up- and down-conversion and multi-exciton generation improve photovoltaics?* Solar Energy Materials and Solar Cells, 2008. **92**(12): p. 1541-1546.
76. Conibeer, G. *Third generation photovoltaics*. in *Nanoscale Photonic and Cell Technologies for Photovoltaics II*. 2009. San Diego, CA, USA: SPIE.
77. Lakshminarayana, G., et al., *Co-operative downconversion luminescence in  $Tm^{3+}/Yb^{3+} : SiO_2-Al_2O_3-LiF-GdF_3$  glasses*. Journal of Physics D: Applied Physics, 2008(17): p. 175111.
78. Ekins-Daukes, N.J., et al. *Physics of quantum well solar cells*. in *Physics and Simulation of Optoelectronic Devices XVII*. 2009. San Jose, CA, USA: SPIE.
79. Nozik, A.J., *Multiple exciton generation in semiconductor quantum dots*. Chemical Physics Letters, 2008. **457**(1-3): p. 3-11.
80. Anderson, N.G., *Ideal theory of quantum well solar cells*. Journal of Applied Physics, 1995. **78**(3): p. 1850-1861.
81. Ghosh, K., *Material Selection for Three Level Transition Using Quantum Well Structure*, in *Electrical and Computer Engineering*, University of Delaware.
82. Mazzer, M., et al., *Progress in quantum well solar cells*. Thin Solid Films, 2006. **511-512**: p. 76-83.
83. Ekins-Daukes, N.J., et al., *Strained and strain-balanced quantum well devices for high-efficiency tandem solar cells*. Solar Energy Materials and Solar Cells, 2001. **68**(1): p. 71-87.
84. Gonzalez-Valls, I., et al., *Vertically-aligned nanostructures of ZnO for excitonic solar cells: a review*. Energy and Environmental Science, 2009. **2**: p. 19-34.
85. Fan, H.J., P. Werner, and M. Zacharias, *Semiconductor Nanowires: From Self-Organization to Patterned Growth*. Small, 2006. **2**(6): p. 700-717.
86. Lee, J.-C., et al., *Synthesis of hybrid solar cells using CdS nanowire array grown on conductive glass substrates*. Electrochemistry Communications, 2009. **11**(1): p. 231-234.
87. Kempa, T.J., et al., *Single and Tandem Axial p-i-n Nanowire Photovoltaic Devices*. Nano Letters, 2008. **8**(10): p. 3456-3460.
88. Nozik, A.J., *Exciton multiplication and relaxation dynamics in quantum dots: Applications to ultra-high efficiency solar photon conversion*. Conference Record of the 2006 IEEE 4th World Conference on Photovoltaic Energy Conversion, WCPEC-4, 2007. **1**: p. 40-4.
89. Raffaele, R.P., *Multi-junction solar cell spectral tuning with quantum dots*. Conference Record of the 2006 IEEE 4th World Conference on Photovoltaic Energy Conversion, WCPEC-4, 2007. **1**: p. 162-6.
90. Kuo, D.M.T. and Y.-C. Chang, *Electron tunneling rate in quantum dots under a uniform electric field*. Physical Review B, 2000. **61**(16): p. 11051.
91. Grundmann, M., O. Stier, and D. Bimberg, *InAs/GaAs pyramidal quantum dots: Strain distribution, optical phonons, and electronic structure*. Physical Review B, 1995. **52**(16): p. 11969.

92. Rahilly, W.P., *Vertical multijunction solar cells*. Record of the Ninth IEEE Photovoltaic Specialists Conference, 1972: p. 44-52.
93. Sater, B.L., *The multiple junction edge illuminated solar cell*. Record of the 10th IEEE Photovoltaic Specialists Conference, 1974: p. 188-93.
94. King, R.R., *40% efficient metamorphic GaInP/GaInAs/Ge multijunction solar cells*. Applied Physics Letters, 2007. **90**(18).
95. Zhangbo, Y., et al., *The cooling technology of solar cells under concentrated system*. 2009 IEEE 6th International Power Electronics and Motion Control Conference, 2009: p. 2193-7.
96. Yoshida, A., et al., *Characteristics of concentrator triple junction cell optimized for current matching*. record of the 2006 IEEE 4th World Conference on Photovoltaic Energy Conversion, 2007. **1**: p. 757-9.
97. Mayberry, C.S., K.C. Reinhardt, and T.L. Kreifels, *Monolithic crystalline multijunction solar cell development and analysis at the US Air Force research laboratory*. Renewable Energy, 2003. **28**(11): p. 1729-1740.
98. Bielawny, A., et al. *Dispersive elements for spectrum splitting in solar cell applications*. in *Photonics for Solar Energy Systems*. 2006. Strasbourg, France: SPIE.
99. Green, M.A. and A. Ho-Baillie, *Forty three per cent composite split-spectrum concentrator solar cell efficiency*. Progress in Photovoltaics: Research and Applications, 2010. **18**(1): p. 42-47.
100. Vincenzi, D., et al., *Concentrating PV system based on spectral separation of solar radiation*. physica status solidi (a), 2009. **206**(2): p. 375-378.
101. Barnett, A., et al., *Very high efficiency solar cell modules*. Progress in Photovoltaics: Research and Applications, 2009. **17**(1): p. 75-83.
102. Wilcox, J.R., et al. *Combining solar cell and optical modeling in multijunction systems*. in *Photovoltaic Specialists Conference (PVSC), 2009 34th IEEE*. 2009.
103. Karp, J.H. and J.E. Ford. *Multiband solar concentrator using transmissive dichroic beamsplitting*. in *High and Low Concentration for Solar Electric Applications III*. 2008. San Diego, CA, USA: SPIE.
104. Esaki, L., *New Phenomenon in Narrow Germanium p-n Junctions*. Physical Review, 1958. **109**(2): p. 603.
105. Würfel, P., *Physics of Solar Cells: From Basic Principles to Advanced Concepts*. 2nd ed. 2009, Weinheim: Wiley-VCH.
106. Sze, S.M., *Physics of Semiconductor Devices*. 1981, New York: John Wiley & Sons.
107. Cañizo, C.d., G.d. Coso, and W.C. Sinke, *Crystalline silicon solar module technology: Towards the 1 euro per watt-peak goal*. Progress in Photovoltaics: Research and Applications, 2009. **17**(3): p. 199-209.
108. Andersson, B.A., et al., *Material constraints for thin-film solar cells*. Energy, 1998. **23**(5): p. 407-411.
109. Cotal, H., et al., *III-V multijunction solar cells for concentrating photovoltaics*. Energy and Environmental Science, 2009. **2**(2): p. 174-92.

110. Friedman, D.J., et al., *Exploration of GaInTlP and related Tl-containing III-V alloys for photovoltaics*. AIP Conference Proceedings, 1999(462): p. 401-5.
111. Beneyton, R., et al., *Experimental and theoretical investigation into the difficulties of thallium incorporation into III-V semiconductors*. Physical Review B, 2005. **72**(12): p. 125209.
112. Kajikawa, Y., et al., *Effect of Tl content on the growth of TlGaAs films by low-temperature molecular-beam epitaxy*. Journal of Applied Physics, 2003. **93**(3): p. 1409-1416.
113. Ohnishi, K., et al., *Effects of annealing on TlGaAs/GaAs single hetero structures and TlGaAs/GaAs multiple quantum well structures grown by low-temperature MBE*. Journal of Crystal Growth, 2007. **301-302**: p. 113-116.
114. Takushima, M., et al., *Thallium incorporation during TlInAs growth by low-temperature MBE*. Journal of Crystal Growth, 2007. **301-302**: p. 117-120.
115. Madou, M.J., *Fundamentals of Microfabrication: The Science of Miniaturization*. 2 ed. 2002, New York: CRC Press.
116. Böer, K.W., *The solar spectrum at typical clear weather days*. Solar Energy, 1977. **19**(5): p. 525-538.
117. Petrie, W.R. and M. McClintock, *Determining typical weather for use in solar energy simulations*. Solar Energy, 1978. **21**(1): p. 55-59.
118. Siefer, G., et al. *Influence of the simulator spectrum on the calibration of multi-junction solar cells under concentration*. in *Photovoltaic Specialists Conference, 2002. Conference Record of the Twenty-Ninth IEEE*. 2002.
119. Bocchi, C., et al., *Measurement of Aluminum Concentration in the Ga(1-x)Al(x)Sb/GaSb Epitaxial System*. Journal of Applied Physics, 1999. **86**(3).
120. Hubener, A., et al. *1.3  $\mu\text{m}$  emission of TlGaP-LEDs grown on GaAs*. in *Indium Phosphide and Related Materials, 1999. IPRM. 1999 Eleventh International Conference on*. 1999.
121. Guter, W., *Current-matched triple-junction solar cell reaching 41.1% conversion efficiency under concentrated sunlight*. Applied Physics Letters, 2009. **94**(22): p. 223504.
122. Kalyuzhnyy, N., et al., *Germanium subcells for multijunction GaInP/GaInAs/Ge solar cells*. Semiconductors. **44**(11): p. 1520-1528.
123. Yamada, T., et al., *5 x 5 cm<sup>2</sup> GaAs and GaInAs Solar Cells with High Conversion Efficiency*. Japanese Journal of Applied Physics, 2005. **44**(31).